UNIONE EUROPEA
Fondo Sociale Europeo
Fondo Europeo di Sviluppo Regionale

Ministero dell'Istruzione, dell'Università e della Ricerca

PON RICERCA E INNOVAZIONE 2014 - 2020

UNIVERSITÀ DEGLI STUDI DI PALERMO

Dottorato di ricerca in Scienze Fisiche
Dipartimento di Fisica e Chimica "E. Segre"
Settore Scientifico Disciplinare FIS/07

Development of 2D & 3D cadmium–zinc–telluride spectroscopic imagers for X-ray and gamma ray applications

THE CANDIDATE
ANTONINO BUTTACAVOLI

THE TUTOR
PROF. LEONARDO ABBENE

THE COORDINATOR
PROF. GIOACCHINO MASSIMO PALMA

XXXIII CYCLE
2021

ACKNOWLEDGEMENTS

First to all, I would like to express my deepest thanks to my supervisor Leonardo Abbene for all his support during my PhD not only for his scientific knowledges (that are very big), but also for establishing a true friendship with me.

My thanks also go to Dr. Fabio Principato for his electronic support and to Prof. Gaetano Gerardi who guided me in the understanding of his softwares.

Special thanks to IMEM-DUE2Lab teams: Silvia Zanettini, Nicola Sarzi Amadè, Nicola Zambelli, Manuele Bettelli and Giacomo Benassi for their support on my PhD work, and their friendship (with Bronz, Dedè and Filo) which shown to me during my stay in Emilia (and that still lasts).

Thanks to Dr Mattew C. Veale for his willingness to let me carry out part of the thesis work at R.A.L., also in smart working (due to the COVID pandemic).

Lastly, a thank you to my family, my girlfriend Susanna and my friends, I hope you may be proud of this achievement.

INTRODUCTION

Recently, great efforts have been made by several research groups and industries in the development of imaging arrays, with single-photon counting and energy resolving capabilities, for colour/spectroscopic X-ray imaging, opening new perspectives for applications within the fields of diagnostic medicine, synchrotron applications, non-destructive testing (NDT) and security screening. Spectroscopic X-ray imagers are typically based on high-Z and wide-band-gap direct-conversion compound semiconductors with the goal to ensure room temperature operation and higher detection efficiency than the traditional semiconductor detectors (silicon, germanium). Silicon drift detectors, invented in 1984 by Gatti and Rehak, were also proposed for room temperature spectroscopic X-ray imaging, representing the best solution up to 20 keV. At high energies, despite their excellent energy resolution and high detection efficiency, few imager prototypes based on high-purity germanium (HPGe) detectors have been developed, mainly due to their cumbersome cryogenic cooling (liquid and mechanical coolers) and the difficulties in fabricating small pixel devices.

Among the compound semiconductors, cadmium zinc telluride (CdZnTe or CZT) represents now a key material for radiation detection because of its appealing physical properties (high atomic number, wide band gap, high density) and the continuing advancement of the crystal growth and device-fabrication technologies. Several companies and researchers are involved in the development of spectroscopic-grade CZT crystals and devices, aiming to obtain improvements in charge-carrier-transport properties, electrical contacts, charge collection, electronic noise, charge sharing and high-flux radiation-induced polarization phenomena.

The activities of my PhD's research were carried out within this framework and its main focus was the development and characterization of new CZT detectors with pixel and drift electrodes, covering X-ray and gamma ray energies up to 1 MeV. One of the goals was to develop pulse processing techniques, trough a digital approach, for performance improvements in the detectors. New 2D and 3D CZT detectors were developed, within two leading research projects (*Avatar X* and *3-CaTS*), as prototypes of advanced spectroscopic imagers for food inspections and medical applications.

My PhD's research was funded by the Italian Ministry for University and Research (MUR) under the national research and innovation plan (PON 2014-2020), which foresaw a collaboration among the Department of Physics and Chemistry (DiFC) Emilo Segrè of University of Palermo (Italy), an Italian company (due2lab, Parma, Italy) and the Rutherford Appleton Laboratory (RAL, UK).

More in detail, the presentation of all the research activities and results are organized as follows.

After a brief introduction on compound semiconductor radiation detectors, in the *first Chapter*, is reported an overview on the physical properties of the CZT material and the main critical issues for radiation detection.

In the *second Chapter*, the spectroscopic performances of different CZT pixel detectors are presented, with particular attention to the mitigation and correction of the charge sharing distortions.

The results of the spectroscopic characterization of new 3D CZT drift strip detectors and new correction techniques constitute the *third Chapter*.

A review of the main results obtained during this work is presented in the conclusions, where future perspectives are also pointed out.

CONTENTS

1. CADMIUM-ZINC-TELLURIDE RADIATION DETECTORS

1.1. Compound Semiconductor Radiation Detectors

The success of semiconductor detectors is due to several properties that are not available with other types of detectors: the excellent energy resolution, the high detection efficiency and the possibility of developing compact detection systems.
The principle of operation of semiconductor detectors is represented by the direct conversion of the energy released by a photon during the interaction process into an electrical signal. Generally, the choice of the proper semiconductor detector is related to key physical features:

The main physical characteristics to point out are:

- atomic number (Z)
- bandgap (Eg)
- resistivity (ρ)
- mobility-lifetime products ($\mu\tau$) for charge carriers (electrons and holes)

- ✓ Since the photoelectric effect cross section is proportional to Z^n (where n = 4~5), materials with high atomic number are required for high detection efficiency;
- ✓ The width of the bandgap affects different aspects of a detector. A wide bandgap (more than 1.4 eV) decreases the number of charges thermally generated, ensuring good room temperature performances when detectors work at room temperatures. Nevertheless, a bandgap too large affects the increase on the energy pair production (w), with larger statistic fluctuations

in energy resolution Semiconductors with bandgap values between 1.5 - 2.2 eV, can represent a good compromise;

- ✓ high resistivity values (more than 10^8 Ω·cm) decrease leakage currents and allow us to use high electric fields;
- ✓ to optimize charge collection, good transport properties of the charge carriers are required. In particular, the drift lenght of carriers $\lambda=\mu\tau E$ (where E is electric field generated by bias voltage V), must be greater than the thickness L of the detector.

$$\mu\tau E \gg L \quad \rightarrow \quad \mu\tau \gg \frac{L}{E} = \frac{L^2}{V} \qquad (1.1)$$

Moreover, difference between transport properties for holes and electron leads to distortion in the spectra. In particular, since there is often a $\mu\tau$ of the holes smaller than that of the electrons, spectra are affected by hole tailing.

Furthermore, other very important aspects are the ability to create crystals with a high degree of homogeneity to minimize recombination and trapping of carriers and to guarantee good transport properties for the charge carriers.

Silicon (Si) and germanium (Ge) represent the main semiconductors for radiation detectors (*Knoll, 2000*). Advances in crystal growth processes, high crystal purity and good transport properties of the charge carriers, ensured excellent energy resolution of the detectors. In particular, due to the low atomic number Z_{Si} =14 and the limited thickness (1 mm), Si detectors are very appealing up to 20 keV. While, Ge detectors represent the best choice for gamma ray measurements, even if obtained at criogenic temperatures.

The desire to have detectors with higher detection efficiency than silicon and the performance of germanium even at room temperature has stimulated intense research activities on the development of new semiconductor materials (compound semiconductors).

Compound semiconductors as radiation detectors were first studied in 1945 by Van Heerden who used AgCl crystals for the detection of alpha particles and gamma rays.

Typically, compound semiconductors are obtaineded from elements of groups III and V (e.g. GaAs) and groups II and VI (e.g. CdTe) of the periodic table. In addition to binary compounds, ternary materials have also been produced, e.g. CdZnTe and CdMnTe.

Table 1.1 shows the physical properties of common compound semiconductors typically used for radiation detectors compared with silicon and germanium, while the table 1.2 compares the resolution at different energies reported in literature.

Table 1.1 *Physical properties at room temperature of semiconductor materials for X-ray and gamma ray radiation detectors (M. R. Squillante et al 2016; E. Belas et al 2014).*

Material	**Si**	**Ge**	**GaAs**	**TlBr**	**HgI_2**	**CdTe**	**$Cd_{0.9}Zn_{0.1}Te$**
Crystal Structure	Cubic	Cubic	Cubic (ZB)	Cubic (CsCl)	Tetragonal	Cubic (ZB)	Cubic (ZB)
Average Z	14	32	32	58	62	50	49
Density (g/cm^3)	2.33	5.33	5.32	7.56	6.4	6.2	5.78
Band-gap (eV)	1.12	0.67	1.43	2.68	2.13	1.518	1.57
Pair Creat. Energy (eV)	3.62	2.96	4.2	6.5	4.2	4.43	4.6
Resistivity (Ωcm)	$2.3 \cdot 10^5$	47	10^8	10^{12}	10^{13}	10^9	10^{10}
$\mu\tau_e$ (cm^2/V)	>1	>1	$8 \cdot 10^{-5}$	$1.6 \cdot 10^{-5}$	10^{-4}	$3 \cdot 10^{-3}$	10^{-3}-10^{-2}
$\mu\tau_h$ (cm^2/V)	≈1	>1	$4 \cdot 10^{-6}$	10^{-6}	$4 \cdot 10^{-5}$	$5 \cdot 10^{-4}$	10^{-5}-10^{-4}

Table 1.2 *Energy resolution of typical semiconductor radiation detectors (Owens 2019).*

Material		**Si**	**GaAs**	**TlBr**	**HgI_2**	**CdTe**	**$Cd_{0.9}Zn_{0.1}Te$**
T (°C)		**-15**	**R. T.**	**R. T.**	**0**	**-60**	**R. T.**
Dim	**Area (mm^2)**	**0.8**	**0.8**	**3**	**5**	**16**	**14**
	Thick. (mm)	**0.5**	**0.04**	**0.8**	**0.2**	**12**	**2**
Energy Res. (keV)	**@5.9 keV**	**0.245**	**0.572**	**1.8**	**0.198**	**0.31**	**-**
	@59.6 keV	**0.524**	**0.780**	**3.3**	**0.650**	**0.6**	**1.3**
Ref		***Owens 2003***	***Owens 2003***	***Owens 2003***	***Iwanczyk 1989***	***Loupilov 2001***	***Abbene 2018***

1.2. Cadmium-Zinc-Telluride (CdZnTe or CZT): State of Art

Among compound semiconductors, cadmium-zinc-telluride (CdZnTe or CZT) is a very promising material for room temperature detection of X-ray and gamma ray radiation (*Schlesinger, James et al T.E,1995, 2001*). The first CZT detector was developed in 1992 (*Butler el al, 1992*), since then many advances have been made in crystal growth, contact deposition and signal analysis techniques.

CZT is a ternary compound obtained from CdTe where a little amount of cadmium is substituted by zinc in the crystal growth process.

In $Cd_{1-x}Zn_xTe$ the Zinc amount is in range x=0.1-0.2, with this condition the band gap is larger than 1.5 eV (if zinc amount, x, is 10% the exact value of band gap is 1.572eV) that allows a very low leakage current at room temperature. (*Williams, 1994*).

A point of strength of CZT is that Zn addition increases resistivity of one magnitude order, allowing the reduction of leakage current (electronic noise) and the application of high bias voltages. Moreover, this leads to develop CZT detectors with quasi-ohmic contacts, which are less affected by temporal instabilities (bias-induced polarization effects).

CZT detectors with quasi-ohmic contacts (Au/CZT/Au, Pt/CZT/ Pt) compete with CdTe detectors with rectifying contacts (In/CdTe/Pt, Al/CdTe/Pt), taking into account bias induced polarization and high flux radiation induced polarization.

Bias induced polarization is a phenomenon related to carrier trapping by trapping centers (impurities and defects): trapped carriers distort electric field in the device resulting in a bad carrier collection that changes during the time (*Farella et al., 2009; Grill et al., 2011; Cola and Farella, 2009; Abbene at al., 2013; Principato et al., 2013*). This is a very critical issue when the detector undergoes long working times.

The effects of polarization phenomena are highlighted by variation of the peak counts, by the displacement of the energy peaks and by the variation of the energy resolution.

The high average atomic number of the CZT elements (Z_{Cd}=48, Z_{Zn}=30, Z_{Te}=52) and density allow the prevalence of photoelectric absorption against of Compton

scattering and an efficient stopping power in the region of interest for X-ray and Gamma-ray.

Typical value of CZT resistivity is about $10^{10}\Omega\cdot cm$.

With these values the leakage current is very low also with typical electric field values of thousands $V\cdot cm^{-1}$, that increase the collection of charge carriers and reduce the collection times.

CZT has the same crystalline structure of CdTe; these crystals have a building block composed by two interpenetrating face center cubic (FCC) sub-lattices shifted on the cell diagonal by one-quarter. In CZT Cd and Zn occupy vertexes of one of these sub-lattices and Te occupy the vertexes of the other one. The resulting structures is zinc-blende (Figure 1.1).

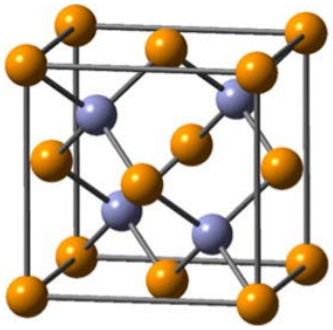

Figure 1.1 *Crystalline structure of CdTe and CZT.*

Very important characteristics are the carriers transport properties mobility $\boldsymbol{\mu}$ and life time $\boldsymbol{\tau}$ values and their contribution in the drift length (Eq. 1.1). The drift length represents the distance that the carriers can cross through the semiconductor before they are trapped, also indirectly suggests the amount of charge loss inside the semiconductor during the carrier's flight. Higher $\boldsymbol{\mu\tau}$ values allow thicker detectors and good charge collection at the electrodes.

$\boldsymbol{\mu}$ and $\boldsymbol{\tau}$ are influenced by the band diagram, the crystalline lattice, defects, and trapping centers. The product of these transport parameters ($\mu\tau$) for CZT is generally better than the parameters of others semiconductor with high Z used in X-ray detector field. However, in CZT, the $\mu\tau$ product for holes is 2 orders of magnitude lower than the one of electrons; the respective value at 300K are: $\mu\tau_h \sim 10^{-(4\div5)}$ $cm^2\cdot V^{-1}$ and $\mu\tau_e \sim 10^{-(2\div3)}$ $cm^2\cdot V^{-1}$. This large difference between

electrons and holes restricts detector performance in particular decreasing energy resolution (this aspect will be explained in paragraph 1.4).

Charge transport properties depend also on impurities and defects of the semiconductor. They operate like scattering centers by changing mobility and by reducing lifetime. Defects are also the cause of the carriers recombination and electric field distortions.

An important aspect to take into consideration is that of obtaining large volumes of monolithic material in order to have detectors with large surface and thickness for imaging at high energy. Monolithic crystals ensure better transport properties than polycrystalline that cause recombination of charge carriers at the grain boundaries. Over the years, different manufacturing techniques for CZT crystals have been developed. The most used growth methods are the traveling heater method (THM) and Bridgman (high and low pressure and boron-encapsulated vertical Bridgman). The main properties are compared in table 1.3.

Table 1.3 *State of art of CZT crystals in detector development.*

Growth Method	**Volume (cm^3)**	**$\mu\tau_e$ (cm^2V^{-1})**	**Ref.**
THM	>20	10^{-2}	*He Z, et al, 2019*
VB	>4	10^{-3}	*McCoy et al, 2019*

The presence of defects and impurities, for a given material, depends on several factors and mainly on the particular manufacturing process.

In a crystal, defects can be point-type, like interstitial defects, vacancies, Frenkel-defects (Figure 1.2), or extended (dislocations, disclinations, grain boundaries, microcracks, inclusions).

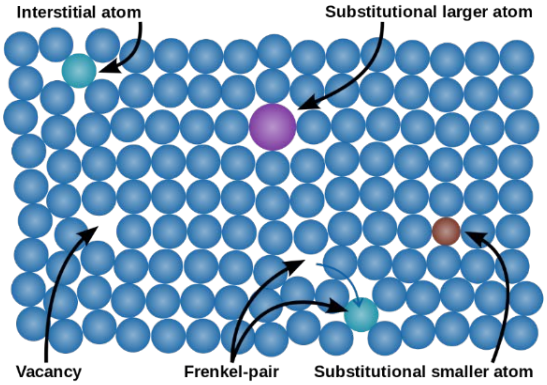

Figure 1.2 *Point-like defects and impurities in a semiconductor crystal*

The impurities, inside the semiconductors, are caused by the presence of doping elements that are introduced during the growth processes to increase their resistivity, CZT is usually doped with group III elements like Indium (*Zappettini et al, 2009*). In the band structure of a perfect crystal, electrons and holes can only occupy the energy levels in the conduction and valence bands, however the presence of doping impurities generates a series of levels.The study of the energy levels associated with defects and impurities can be carried out through different techniques, the figure 1.3 shows the deep levels characteristic of a CZT, founded on the analysis of internal electric field based on Pockels effect performed with optical (*Franc et al, 2015*) and temperatures methods (*Rejhon et al, 2016*).

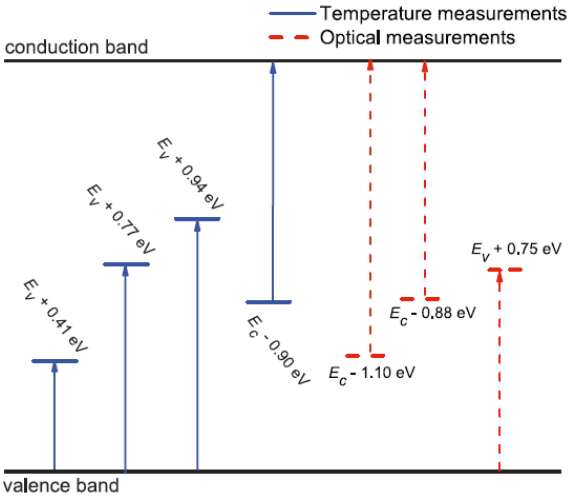

Figure 1.3 *Scheme of the observed energy levels Full lines represent energy levels found bytemperature measurements and dashed lines represent energies which were found by infrared spectral scanning method (Rejhon et al, 2016).*

Grain boundaries (Figure 1.4) can be formed during the growth when local temperature gradients or high growth speeds occurs. Close to the grain boundaries interface many other defects are forming such as impurities, dislocations and disclinations. Mechanical weakening and charge transport limitations are typical of these defects, trapping and recombination effects are also expected in these regions.

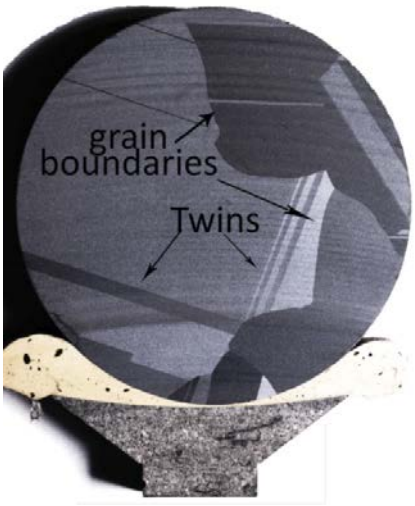

Figure 1.4 *CZT slice wafer cut perpendicular to the growth direction in which grain boundaires and twins are marked.*

Thermal and mechanical stresses due to the cooling down after crystal growth are perpetrators of cracks. Cracks can also be created in the subsequent stages of device preparation such as cutting and lapping processes. Therefore, cracks can be avoided thanks to appropriate choices of: thermal profile, crucible material and cooling down process.

Another category of problems in CZT is the presence of Te inclusions.

Typical diameters of these inclusions are between 1 and 3 microns but larger ones were observed, up to 30 microns, especially close to twin planes or to grain boundary interfaces.

Tellurium electrical resistivity is several orders of magnitude lower than surrounding semiconductor, so that higher leakage current (and then field distortion) is found in the volumes with large number of inclusions. For this reasons Te inclusions strongly limit CZT devices performances, in particular imaging devices.

Figure 1.5 and 1.6 respectively show a 3D distribution of Te inclusion in a CZT block and their concentration as function of diameter observed and reconstruct at IMEM-CNR (Parma).

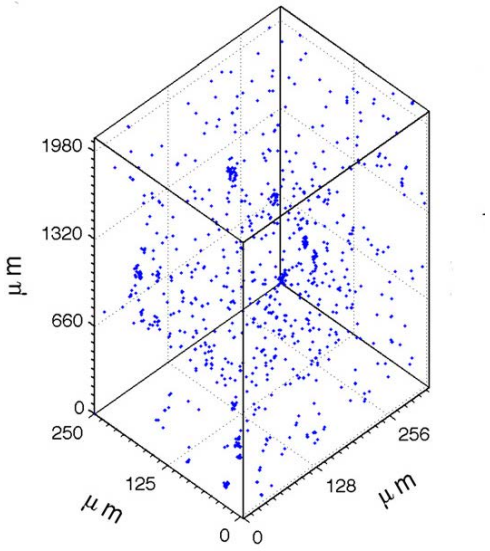

Figure 1.5 *3D-representation of Tellurium inclusions in a CZT block measured at IMEM-CNR (Parma).*

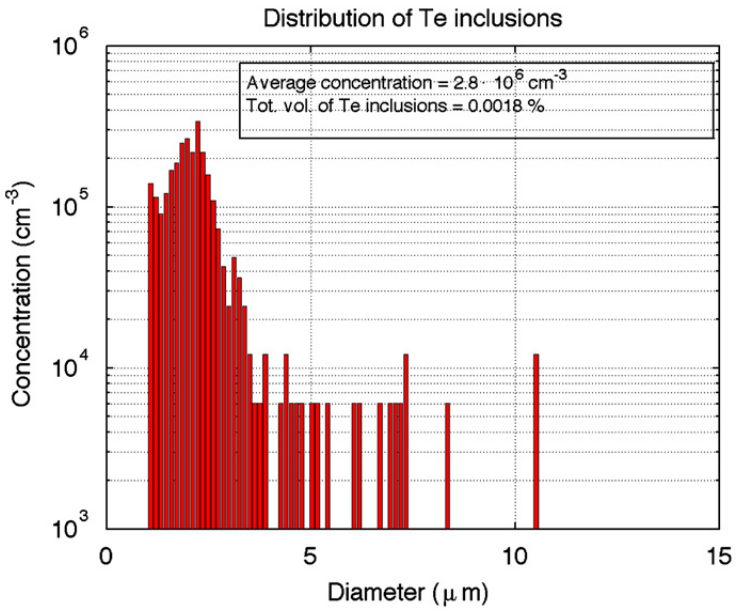

Figure 1.6 *Concentration of Tellurium inclusions as a function of diameter measured at IMEM-CNR (Parma).*

.

1.3. Detection of X Rays and Gamma Rays with CZT Detectors

1.3.1 Interaction mechanisms

Semiconductor detectors are able to detect different type of radiation, electromagnetic waves or sub-atomic particles both uncharged or charged.

Charged particles (α and β) have a strong interaction with matter and typically are stopped and detected in the first lawyers of material.

Neutrons have low interaction with semiconductors used for detectors, therefore it is first necessary to convert neutrons into γ rays or alpha particles, through the use of converting materials.

X and gamma rays are highly penetrating, mainly interact with matter through three different processes such as, photoelectric effect, Compton scattering and pair production.

These three mechanisms lead to the direct conversion of the interacting radiation into an electrical signal.

In particular, in photoelectric effect (Figure 1.7) the entire photon energy is deposited in the detector and, to obtain its energy, it is enough to measure the whole photo-generated charge. For this reason, photoelectric absorption is the ideal process for X and γ spectroscopy.

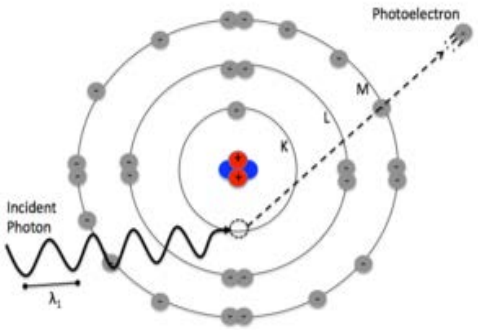

Figure 1.7 *Schematic representation of the photoelectric process. The incident photon is completely absorbed and a photoelectron is ejected.*

When an incident photon is absorbed, an excited electron (photoelectron) is emitted with energy E_k:

$$E_k = h\nu - E_b \qquad (1.2)$$

where $h\nu$ is the energy of incident photon and E_b is the binding energy of emitted electron. The process occurs mainly with the electrons of the innermost shell for which $h\nu > E_b$.

The emitted photoelectron interacts mainly in an inelastic way with the crystalline lattice of the semiconductor, it loses its kinetic energy creating electrons-holes pairs, the number of these pairs is proportional to the energy of the incident photon (Figure 1.8). An electron of external shell, jumping into the shell left empty by the emitted electron, can generate the emission of fluorescence photons.

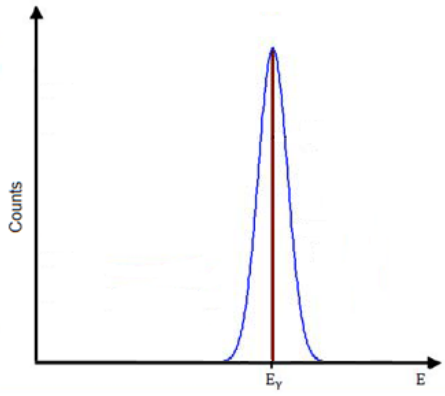

Figure 1.8 *Spectrum of monoenergetic photons interacting through photoelectric process.*

Fluorescence photons are significant in high-Z materials; the most relevant fluorescence energies of CZT are shown in table 1.4.

Table 1.4 *The attenuation length λ_{CdZnTe} of K-shell fluorescent X-rays in CdZnTe materials (Abbene 2018a).*

Element	K-shell absorption energy (keV)	Fluorescence lines	Energy of fluorescent lines (keV)	λ_{CdZnTe} (μm)
Cd	26.7	$K\alpha_1$	23.17	116
		$K\beta_1$	26.10	161
Zn	9.7	$K\alpha_1$	8.54	8.4
		$K\beta_1$	9.57	11.4
Te	31.8	$K\alpha_1$	27.47	69
		$K\beta_1$	31.00	95

Unlike the photoelectric effect, Compton scattering is the interaction between a photon and an electron weakly bound ($E_b << h\nu$), so ones can consider the electron a free electron and initially at rest.

When interaction occurs a fraction of photon energy is transferred to the electron, a photon, with less energy than the incident photon, is emitted deflected to an angle θ respect to incident photon direction (Figure 1.9).

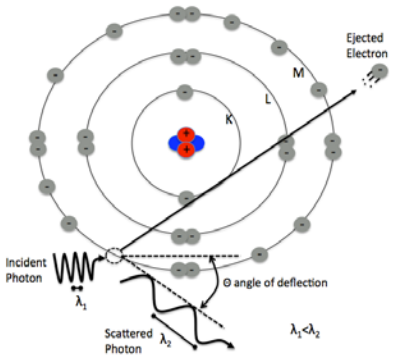

Figure 1.9 *Schematic representation of Compton effect in the scattering plane.*

According to the conservation of energy and momentum it is obtained:

$$E_k = h\nu_1 - h\nu_2 = h\nu_1 \left[\frac{(h\nu_1/m_e c^2)(1 - cos\theta)}{1 + (h\nu_1/m_e c^2)(1 - cos\theta)} \right] \qquad (1.3)$$

The energy transferred to the electron ($\boldsymbol{E_k}$) depends on the scattering angle that can change from 0 (with θ=0) to a maximum value when θ=π; therefore, the energy of monoenergetic incident beam there is a continuum shape as shown in figure 1.10.

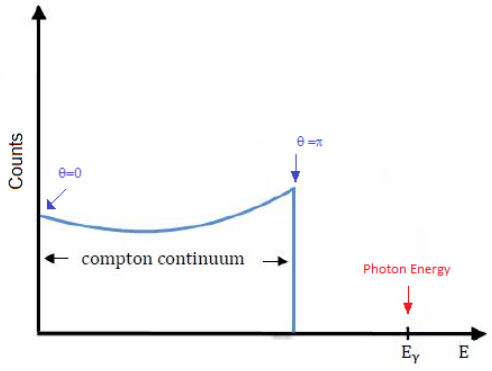

Figure 1.10 *Compton spectrum of monoenergetic photons.*

At last, pair production is a process that occurs when a photon interacting with atomic nucleus generates a pair electron-positron (Figure 1.11).

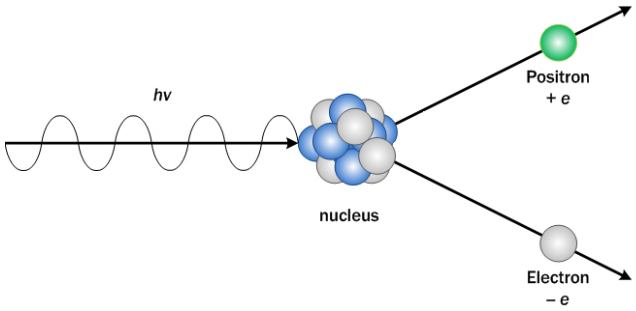

Figure 1.11 *Schematic representation of the pair production process.*

In order that pair production will happen, the energy of incident photon must be greater than 1.02 MeV, that is the twice the rest-mass energy of an electron, in fact:

$$h\nu = E_{-e} + E_{-e} + 2m_e c^2 \qquad \textbf{(1.4)}$$

Summarizing, to develop a detector with good performance, the photoelectric effect must be predominant, as all the energy of the incident radiation is released into the active material of the detector and therefore the charge generated is proportional to the energy of the incident radiation.

The cross sections (**σ**) of the three mechanisms have a strong dependence on the atomic number (*K. Debertin and R.T. Helmer, 1988*):

$$\sigma_{photo} \propto Z^{4\div5} \qquad \sigma_{Compton} \propto Z \qquad \sigma_{pair} \propto Z^2 \qquad \textbf{(1.5)}$$

Focusing the attention on these three interactions, is interesting to analyze the relative importance of the three processes as function of the atomic number and photon energy.

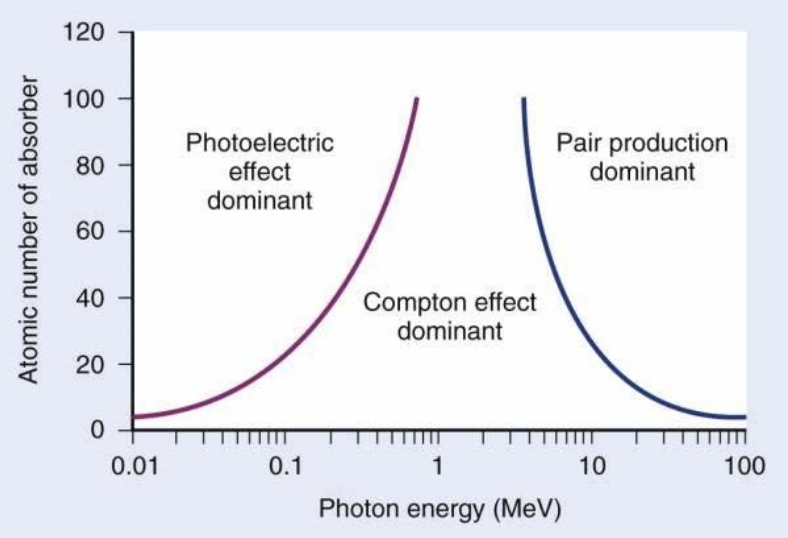

Figure 1.12 *The relative importance of the photoelectric effect, Compton scattering and pair production with different Z numbers and photon energies. Violet and blue curves are respectively Photoelectric-Compton and Pair-Compton equiprobable curve (Knoll, 2000).*

Observing the figure 1.12 it is clear that by choosing a material with a high atomic number, the photoelectric effect will be dominant.

Figure 1.13 (a) shows the overall trend of attenuation coefficient and its relative contributions of Compton, photoelectric effect and pair production for CZT (XCOM: Photon Cross Section Database). At last, the detection efficiency vs. the CZT thickness is also reported (Fig 1.13 (b)).

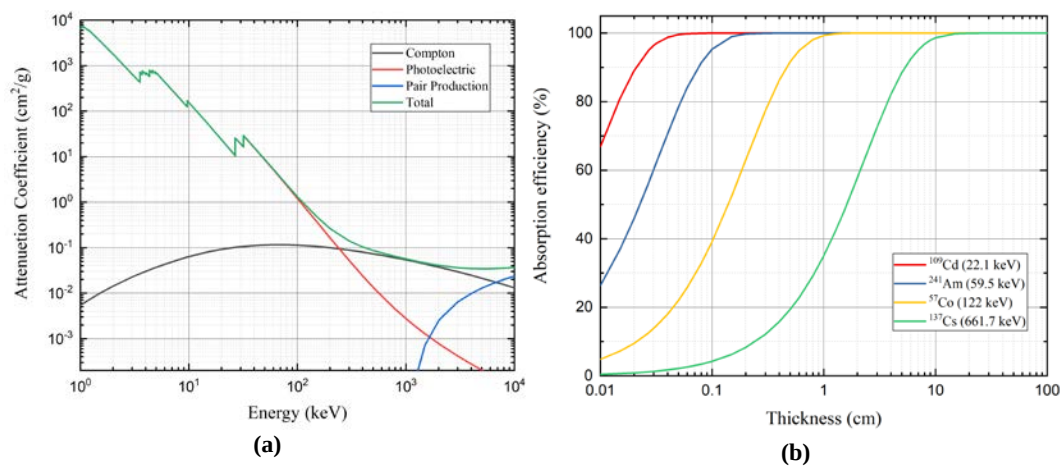

Figure 1.13 a) *Photon absorption cross sections for CZT for Compton, Photoelectric and Pair Productionmechanisms in the 10-104 keV energy range.* ***b)*** *Absorption efficiency of CZT as a function of crystal thickness at various photon energies (corresponding to the most commonly used radionuclides).*

1.3.2 Signal formation and energy resolution

The operating principle of all semiconductor radiation detectors is based on the conversion of the energy released by the radiation during the interaction process into an electrical signal. Figure 1.14 schematically illustrates how a semiconductor detector, based on a planar electrode geometry, directly converts photon energy into electric signal.

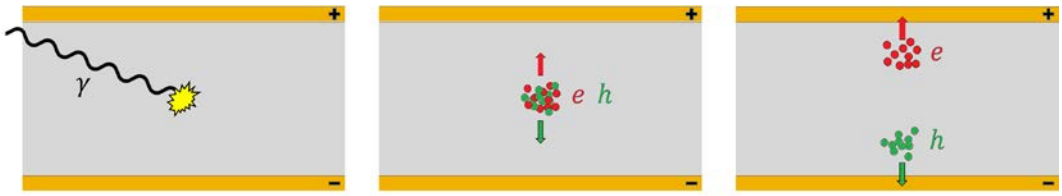

Figure 1.14 *Schematic representation of the signal generation in a semiconductor-based radiation detector: interaction of the γ-ray with the crystal, electron-hole pairs production, drifting and collection.*

The main effect of the interaction of the energy radiation ***E*** with a semiconductor is the production of a certain number ***N*** of electron-hole pairs: ***N=E/w*** (where ***w*** is average electron-hole pair creation energy).

The size of the generated charge clouds is generally related to the photoelectron ejected by the photoelectric interaction of X-rays (*Bolotnikov, 2007; Kalemci & Matteson, 2002*), and its calculation is challenge due to the numerous processes involved in the absorption of primary radiation. However, ones can achieve this by using Monte Carlo simulations in which it is possible to trace all the secondary particles and the energy released at each point of the crystal (*M. Bettelli, et al, 2020*) (Fig. 1.15).

Nevertheless, for low energies (less than 100 keV), the initial size of the electron cloud can be neglected, since it is generally lower than 3 μm (*Bolotnikov et al., 2007*).

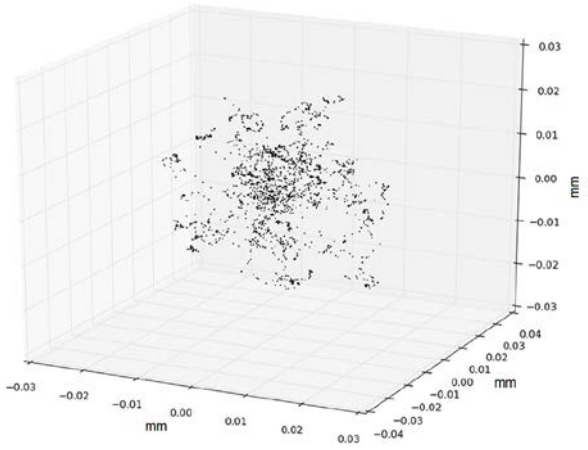

Figure 1.15 *Example of interaction positions of a photoelectron and its secondary particles (). (M. Bettelli, et al, 2020).*

The electric field, attracts the electrons towards the anode and the holes towards the cathode with drift velocity $\boldsymbol{v_e}$ and $\boldsymbol{v_h}$ respectively for electrons and holes according to the equation:

$$\vec{v} = \mu\vec{E} \qquad \textbf{(1.6)}$$

where $\boldsymbol{\mu}$ is the carrier mobility.

This linear relationship, between velocity and electric field, maintains its validity below a saturation value that is much higher than the typical ones used in real devices ($\sim$ 15000 $V \cdot cm^{-1}$ at room temperature for CdTe) (*G. Ottaviani, 1977*); hence, the mobility is assumed to be constant. The electric field within the crystal volume depends from several factors such as applied bias voltage, geometrical configuration of the electrodes, crystal dimensions, presence of spatial charge and defects and the metal contacts.

Due to this large number of factors, calculating the field profile in each point of the crystal is very difficult, for this reason experimental techniques are employed (Pockel effect, Laser Induced Transient Current Technique) (*Uxa et al, 2012*).

The Shockley - Ramo theorem describes the process of charge induction on each of the detector electrodes due to the motion of charge carriers using the concept of a weighting potential (*Shockley W., J. 1938, Ramo S. 1939*).

According to the Shockley-Ramo theorem, the magnitude of induced charge by the movement of a charge $\boldsymbol{q}$ (from initial position x_i to final x_f) on a generic electrode, and the current ($\boldsymbol{i}$) are given by the following expressions:

$$\Delta Q_{ind} = \int_{x_i}^{x_f} qE_0(x)dx = -q\left[\varphi_0(x_f) - \varphi_0(x_i)\right] \qquad (1.7)$$

$$i = \frac{dQ}{dt} = qvE_0$$

with $\varphi_0(x)$ weighting potential, $\mathbf{E}_0$ is the weighting electric field and $\boldsymbol{v}$ is drift speed of charge q and $\boldsymbol{x}$ is the distance from the cathode.

The weighting potential is not a physical field, but is a dimensionless quantity between 0 and 1, it representing the electric potential present in the volume of the detector, applying a unitary potential to the collection electrode and zero for other electrodes.

Figure 1.16 shows the weighting potential as a function of the depth of interaction for 3 different detectors: red for a planar detector in brown and blue two pixels detectors with different geometry; the w/L parameter is the ratio between the pixel size (*w*) and the detector thickness (*L*) (*Del Sordo, 2009*).

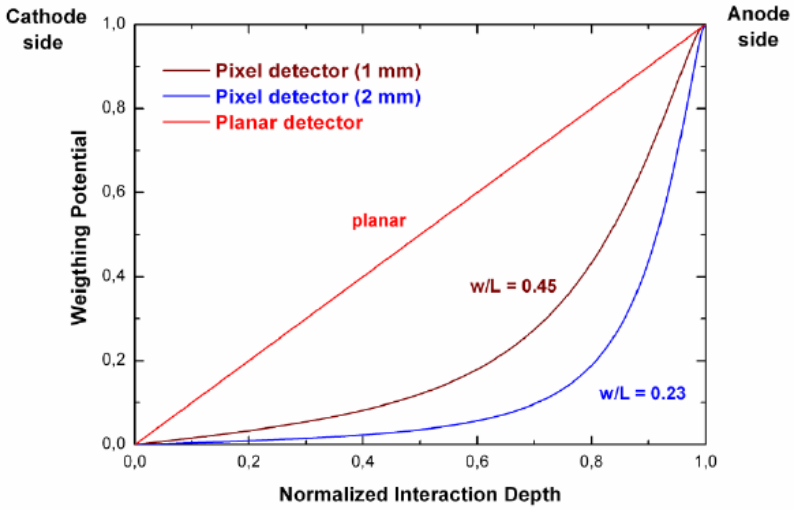

Figure 1.16 *The weighting potential for pixel detectors and a planar detector as a function of the normalized interaction depth (interaction depth/detector thickness).*

For a planar detector (red line of as shown in figure 1.16), the weighting potential assumes a linear trend with the normalized distance from the cathode z = w/L, where L is the thickness of the detector.

Neglecting any losses of the charge carriers (charge trapping) during the path, the induced charge by the drift of N electron-hole pairs, after they have passed through the whole detector, can be written as follows:

$$\Delta Q_{ind} = -(N \cdot e)(0 - z) + (N \cdot e)(1 - z) = N \cdot e \qquad (1.8)$$

with *N·e* initial charge created, that is proportional to deposited energy by photon.
with N·e initial charge created, that is proportional to deposited energy by photon.
Critical issues due to incomplete charge collection will be explained in the next paragraph.

In a typical detection system, shown in the figure 1.17, the detector is connected to a charge sensitive preamplifier (CSP) which integrates and amplifys the signal generated by the incident radiation into detector, then further amplified and formed by a linear amplifier (Shaping Amplifier) and finally sampled from a multi-channel analyzer (MCA).

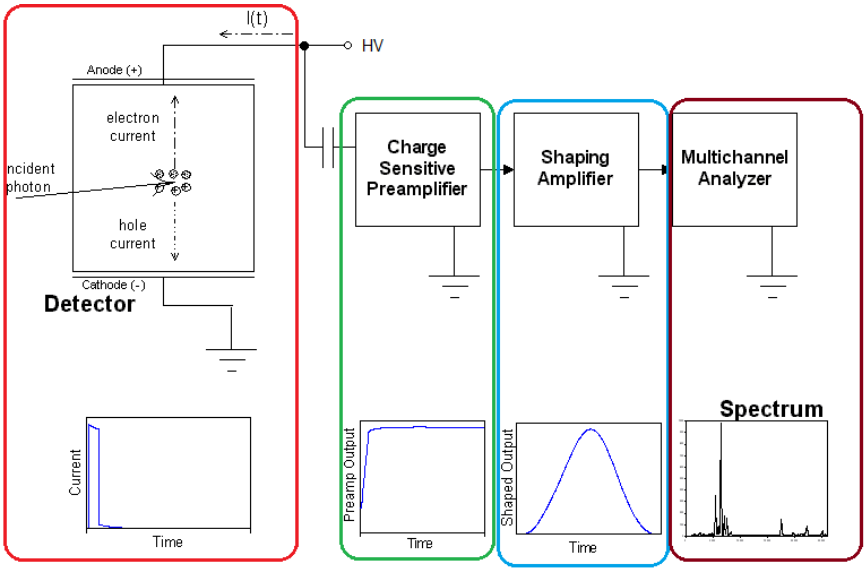

Figure 1.17 *Typical detection system in which the different phases are highlighted, from the detection of the signal (in red) to the formation of the spectrum, the lower part of figure shows the different outputs of every step.*

The energy spectrum in output from the detection system shows a widening, this determines the energy resolution of the detector and is usually expressed in terms of full width at half maximum (FWHM) *(Knoll, 2000)*.

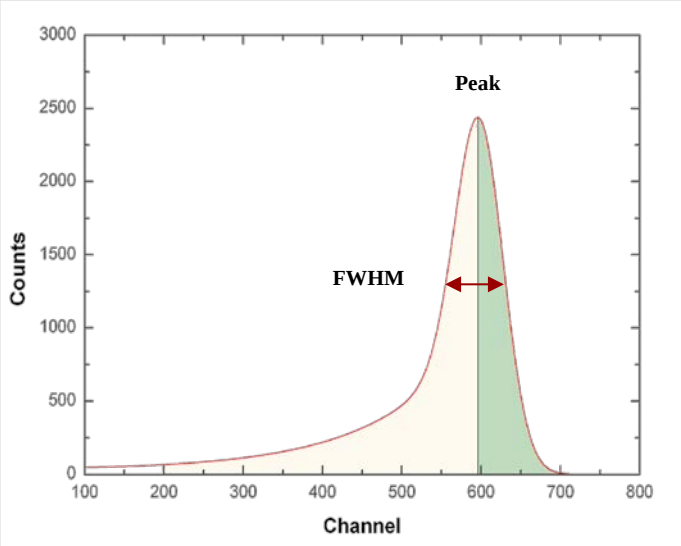

Figure 1.18 *Definition of detector resolution.*

Widening is due to several noise sources that contribute to broadening the photopeak, these contributions are generally considered independent, so we can consider the total FWHM as:

$$FWHM_{tot}^2 = FWHM_{stat}^2 + FWHM_{det}^2 + FWHM_{elettr}^2 \qquad \textbf{(1.9)}$$

- ***FWHM$_{stat}$*** is related to the statistical fluctuations in the generation of the electrons-holes pairs, this term is known as Fano noise and it depends only from electron-hole pair creation energy. Its contribution to energy resolution can be expressed in terms of incident radiation energy (E), pair creation energy (w) and the Fano factor (F), a dimensionless number varying between 0.06 and 0.16 (*Devanathan, 2006*):

$$FWHM_{stat} = 2.355\sqrt{FEw} \qquad \textbf{(1.10)}$$

- $\boldsymbol{FWHM_{det}}$ represent the contributions due to physical properties of semiconductor, is related to the incomplete charge collection of generated charges;

- $\boldsymbol{FWHM_{elettr}}$ is the contribution related both to the noise of the read-out system and to the leakage current of detector.

1.4. Critical Issues and Challenges

Here, the typical critical issues in CZT detectors will be presented, pointing out the state-of-art techniques for their mitigation and correction.

1.4.1 Incomplete charge collection

Ideally, the charge induced on an electrode is equal to N·e, but, as widely shown in the literature, charge trapping reduces that amount.

The influence of trapping on the induced charge can be simply described quantitatively by assuming for the initial charge Q_0 a decreasing exponential time behaviour, with a time constant equal to the average life time τ of the charge carriers (*Schlesinger and James, 1995*):

$$PQ(t) = Q_0 e^{-\frac{t}{\tau}} \quad \textbf{(1.11)}$$

In the case of uniform trapping, it is possible to express the position of the charge carrier in function in the generic instant of time t:

$$x = x_0 \pm \mu E t \quad \textbf{(1.12)}$$

Where x=0 and x=L are the positions of the cathode and anode respectively.
(+ and – sign for electrons and holes respectively) so combining 1.11 and 1.12

$$Q(x) = Q_0 e^{-\frac{x_0 \mp x}{\mu \tau E}} \quad \textbf{(1.13)}$$

An infinitesimal shift of the charge carriers (dx) will induce on a detector electrode an amount of charge equal to (Shockley-Ramo):

$$dQ(x) = \frac{Q_0}{L} e^{-\frac{x_0 \mp x}{\mu \tau E}} dx \quad \textbf{(1.14)}$$

For electrons and holes, integrating, it is obtained:

$$\Delta Q_{ind,h}(t) = \begin{cases} \frac{Ne\mu_h\tau_h E}{L}\left[1 - \exp\left(-\frac{x_0 - x(t)}{\mu_h\tau_h E}\right)\right] & t < t_{c,h} = \frac{x_0}{\mu_h E} \\ \frac{Ne\mu_h\tau_h E}{L}\left[1 - \exp\left(-\frac{x_0}{\mu_h\tau_h E}\right)\right] & t \geq t_{c,h} \end{cases}$$

$$Q_{ind,e}(t) = \begin{cases} \frac{Ne\mu_e\tau_e E}{L}\left[1 - \exp\left(-\frac{x(t) - x_0}{\mu_e\tau_e E}\right)\right] & t < t_{c,e} = \frac{L - x_0}{\mu_e E} \\ \frac{Ne\mu_e\tau_e E}{L}\left[1 - \exp\left(-\frac{L - x_0}{\mu_e\tau_e E}\right)\right] & t \geq t_{c,e} \end{cases} \quad \textbf{(1.15)}$$

In the presence of trapping and excluding detrapping phenomena, charge induced for time greater than the collection times of the charge carriers ($t > t_r$) will no longer be equal to the charge generated by the radiation (Ne), but it will also depend on the interaction depth x_0 (distance between the interaction point and the cathode) through the following relationship:

$$Q_{ind} = Ne\left\{\frac{\mu_h\tau_h E}{L}\left[1 - \exp\left(-\frac{x_0}{\mu_h\tau_h E}\right)\right] + \frac{\mu_e\tau_e E}{L}\left[1 - \exp\left(-\frac{L - x_0}{\mu_e\tau_e E}\right)\right]\right\} \quad \textbf{(1.16)}$$

Equation 1.16 is the Hecht equation (*Hecht K.,1932*).

The point of interaction of the incident photons (x_0) varies statistically according the exponential law of absorption, causing a widening of the response function of the detector. This further widening is affected by normalized drift length for both electrons and holes $\lambda/L = \mu\tau E/L$.

The effects of the depth of interaction on charge induced can be minimized by increasing the λ/L ratio for both charge carriers (*Knoll, 2000*). In CdTe and CZT detectors, this ratio is quite low but it is also different for electrons and holes; the major trapping for the holes and therefore a consequent shorter average mobility-time product gives rise to a series of distortions mainly expressed by an asymmetrical widening of the energy peaks of the measured spectra and by the presence of tails on the low energy side of the peaks (hole tailing, figure 1.19).

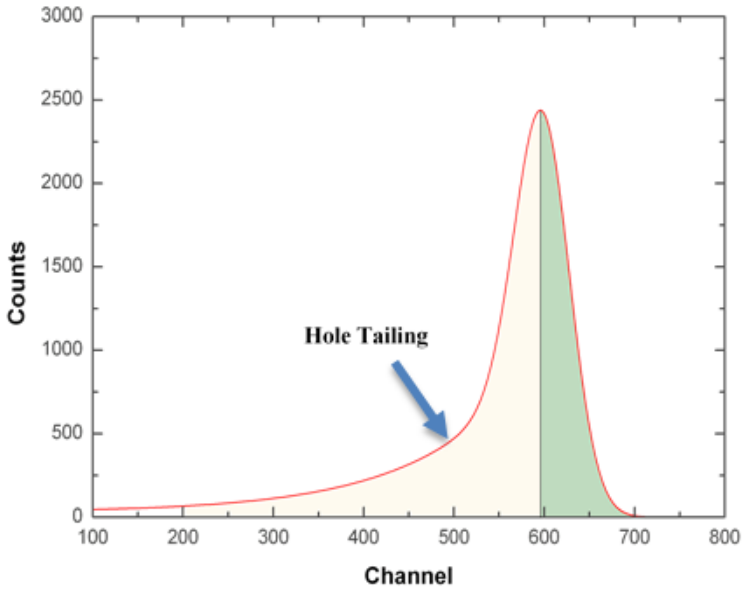

Figure 1.19 *The Hole Tailing effects.*

To reduce the effects generate by hole trapping many detectors are based on the *one carrier collection* method. This method tries to reduce the signal due to the holes by creating particular geometric layouts of the electrodes like *Frisch Grids, Coplanar Grids, Pixels and Strips* (Figure 1.20).

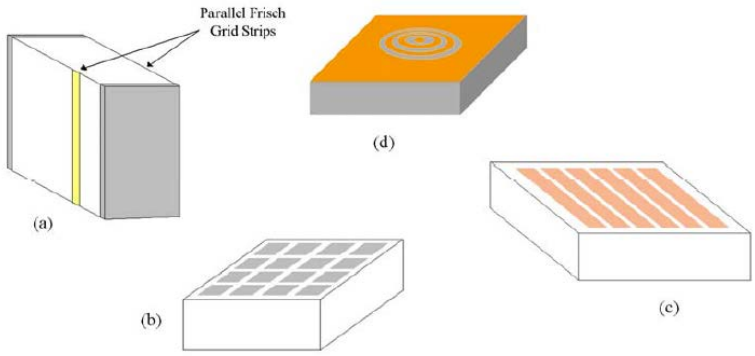

Figure 1.20 *Single charge collection electrode configurations widely used in CdTe and CdZnTe detectors:* ***(a)*** *parallel strip Frisch grid design,* ***(b)*** *pixels,* ***(c)*** *strips and* ***(d)*** *multiple electrodes.*

With these types of electrodes, weighting potential is significantly reduced near the cathode and grows more rapidly near the anode (as shown in figure 1.21). So, the charge induced on the anode, that is proportional to the weighting potential, will mainly depend on charge carriers that will drift towards the anode, thus leading the device sensitive only to electrons (unipolar detector).

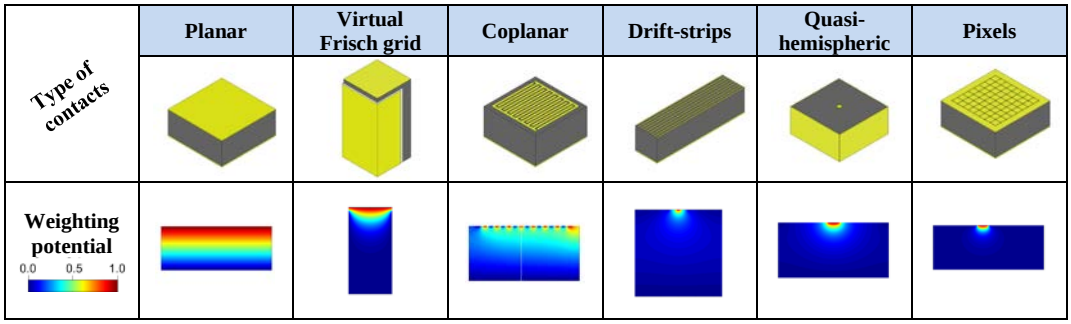

Figure 1.21 *Qualitative results of the simulation on different detectors: contacts type and detectors shape are represented in the first row; weighting potential maps of a cross-section of each detector are in the second row (Bettelli, 2020).*

Other techniques to reduce the effects of the hole trapping on spectra concern the analysis of the pulse shape (rise time, peaking time, etc.).

Pulse shape discrimination, first introduced by Jones and Woollam in 1975, is a common technique to reduce the effects of incomplete charge collection in CdTe/CZT detectors. Usually, this technique is based on the selection of a range of peaking time values of the pulses that are less influenced of incomplete charge collection. The pulses mostly influenced by the hole contribution are generally characterized by longer peaking times. These effects are more marked increasing the energy of radiation (i.e. the depth of interaction of radiation); the events, with a greater depth of interaction, take place close to the anode electrode producing pulses mostly due to the hole transit. Figure 1.22 shows the improvements of energy resolution in a CdTe detector after the application of PSD (*Abbene et al. 2013*).

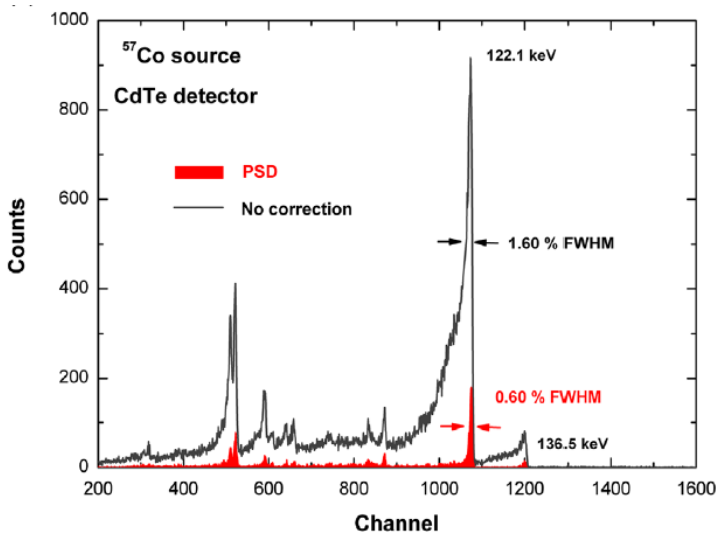

Figure 1.22 *Measured ^{57}Co spectra after PSD. After PSD, an energy resolution of 0.60% FWHM at 122.1keV was obtained. (Abbene, 2013).*

As proposed by Sjöland and Kristiansson in 1994, pulse shape discrimination can also be used to minimize peak pile-up events. Because the shape (peaking time) of a peak pile-up pulse differs from that of a pulse not affected by pile-up, analyzing the measured spectra at different peaking time regions (PTRs) in the peaking time distribution is helpful to reduce peak pile-up.

The improvements obtained through the use of the PSD are at the expense of the throughput, as many events are discarded. To avoid the rejection of the events, pulse shape correction (PSC) methods, based on the measurement of both the peaking time and the height of the pulses have been developed. The approach developed by *Abbene and Gerardi (2011)* foresees the modelling of the measured energy (photopeak centroids of energy spectra) through a linear function:

$$E_{det} = m_e T_p + E_{corr} \quad \textbf{(1.17)}$$

where E_{det} is the photopeak centroid, m_e is the slope of the linear function, T_p is the peaking time and E_{corr} is the corrected centroid at zero peaking time. The corrected centroid, E_{corr}, is the result of correcting E_{det} to an ideal point of zero peaking time and it is the desired height for a pulse. It is interesting to note that both the slope m_e and E_{corr} are linear functions of the true photon energy E, as shown in Figures. 1.23. The fitting equations are:

$$m_e = k_1 E + k_2 \quad \textbf{(1.18)}$$

$$E_{corr} = k_3 E + k_4 \quad \textbf{(1.19)}$$

where k_1, k_3 and k_2, k_4 are the slopes and the y-intercepts of the linear functions, respectively. Combining Eqs. (1.18) and (1.19), yields:

$$m_e = \frac{k_1}{k_3}(E_{corr} - k_4) + k_2 \quad \textbf{(1.20)}$$

If one put the following:

$$A = \frac{k_1}{k_3}$$
$$B = \frac{k_2 k_3 - k_1 k_4}{k_3} \quad \textbf{(1.21)}$$

combining Eqs.(1.17) (2.20) and (1.21), yields:

$$E_{corr} = \frac{E_{det} - BT_p}{1 + AT_p} \qquad \textbf{(1.22)}$$

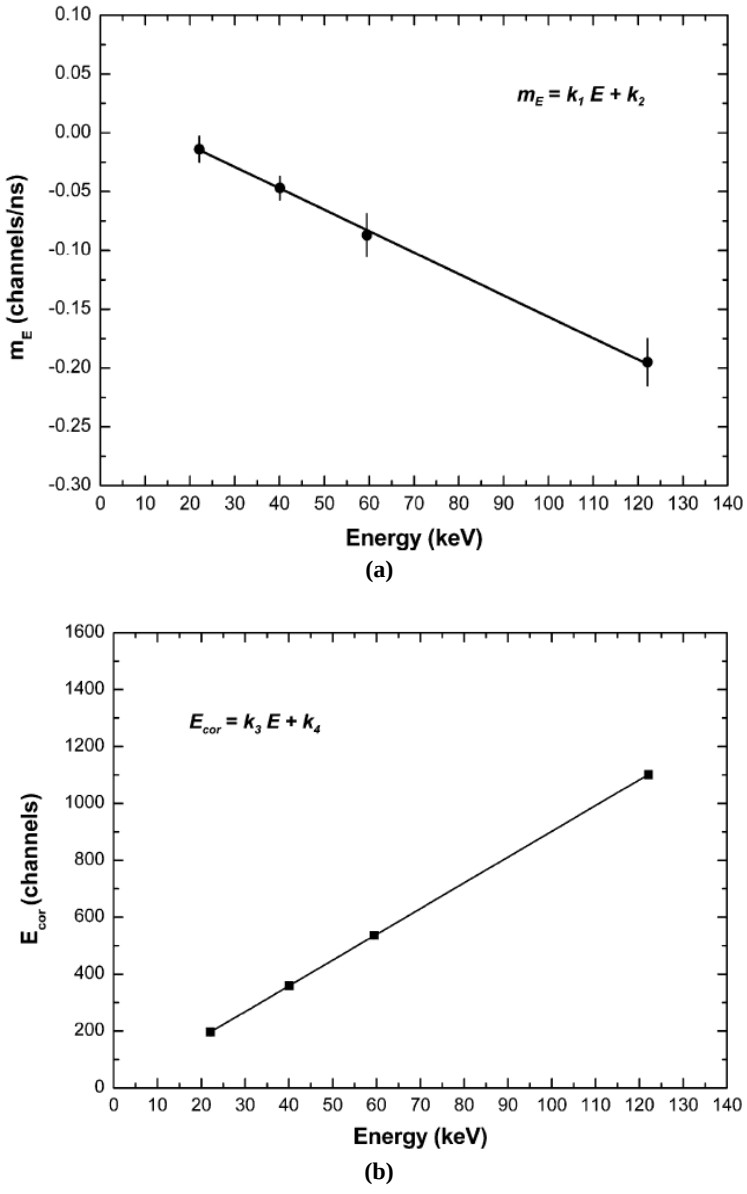

Figure 1.23 (a) *Slope m_E and* ***(b)****corrected centroid E_{cor} vs. the radiation energy.*

By using Eq.(1.22) it is possible to adjust the detected pulse height (E_{det}) of a pulse through the knowledge of the bi-parametric distribution and of the constants A and B obtained by the calibration procedure (Eqs.1.21)). Fig 1.24.shows an example of PSC in a CdTe (Abbene et al. 2013).

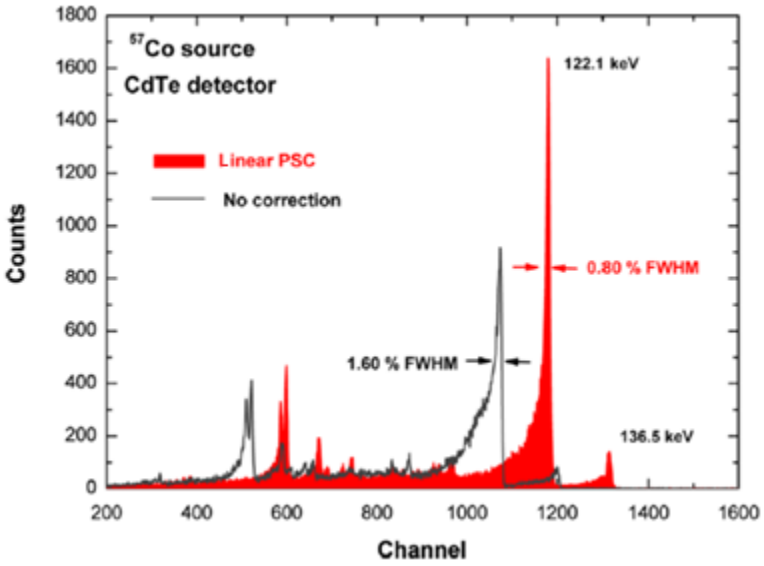

Figure 1.24 *^{57}Co spectra measured with no correction and after linear pulse shape correction (PSC). The detector, after PSC, shows low tailing and an energy resolution of 1.6% (FWHM) at 122.1 keV (Abbene, 2013).*

1.4.2 High-flux radiation induced polarization

Imaging applications typically require photon flux fields that generate very high count-rates within the CZT crystal. In particular, medical computer tomography applications represent a large potential market for this technology but require detectors capable of handling high count of $(20\text{-}200)\cdot 10^6$ counts$\cdot$mm$^{-2}\cdot$s^{-1} (*Bale and Szeles 2008*).

Therefore, high speed counting is required in order to avoid the accumulation of charge inside the crystal, which would collapse the electric field causing spectral distortions or, in extreme cases, the complete destruction of the detector.

This phenomenon is called ***high-flux radiation induced polarization***.

The temporal response of the detector depends on the charge density distribution and the electric field distribution inside the detector, the high densities of impurities and defects in the semiconductor affect the charge carrier densities, creating a series of energy level in bandgap, these energy levels constitute trapping sites for the charge carriers, figure 1.25 schematically shows the processes that the presence of these levels can generate on the charges (for simplicity, one level for the holes and one for the electrons are shown) (*Du et al, 2002*)

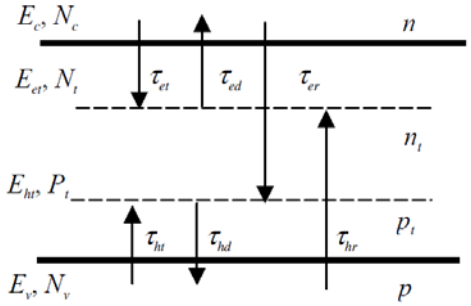

Figure 1.25 *The major processes that determine the electron and hole trapping.*

In steady states generated by high-flux x-rays, the concentrations of free carriers can be many orders of magnitude larger. The accumulation of space charge at deep levels can distort the electric field with critical issues in charge collection (*Sellin, 2010*).

This degradation effect is more marked at low temperatures, with increasing the detector thickness and the photon energy; while these effects can be mitigated by increasing the bias voltage and by using CZT materials with high charge transport properties. (*Sellin et al 2010, Abbene at al 2016*). Figure 1.26 show an example of detected ^{57}Co spectra by a Planar CZT under two different fluence rate, the collapse of detector is clearly visible at higher rate (blue line) (*Abbene et al, 2016*).

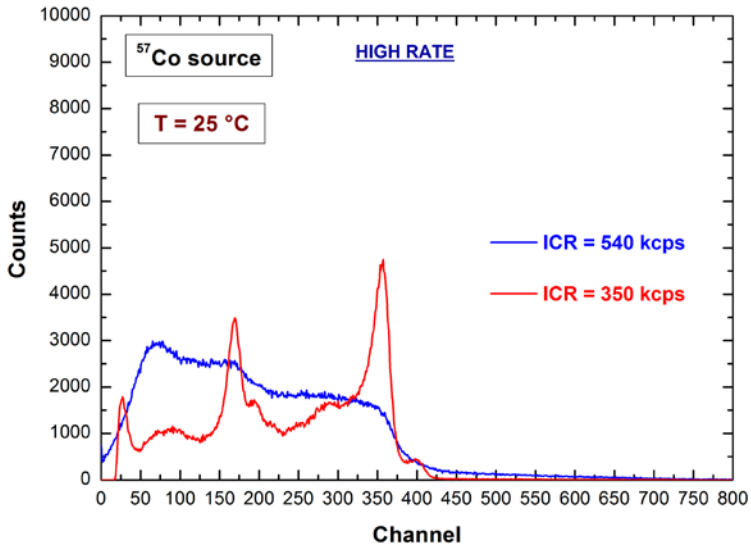

Figure 1.26 *High-rate ^{57}Co spectra measured with a planar detector. The collapse of detector is clearly visible at the higher rate (Abbene et al, 2016)*

1.4.3 Charge sharing

The effects of charge broadening in pixel/strip detectors are generally refered to charge sharing. Due to the applied bias voltage, the electrons migrate to the anode, charge cloud expands during drifting through the thickness of the detector (Figure 1.27).

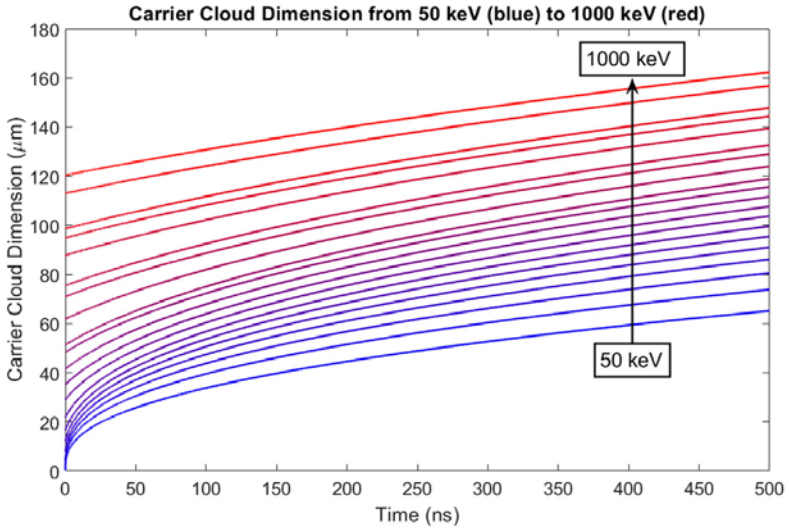

Figure 1.27 *Time evolution of carrier cloud size generated by photoelectrons in the range 50–1000 keV due to Coulomb repulsion and charge diffusion. (M. Bettelli, et al, 2020)*

The broadening of the electron cloud is mainly due to charge diffusion, Coulomb repulsion, K-shell fluorescence and Compton scattering (*Bolotnikov et al., 2007; Kim et al., 2011*).

The broadening of the carrier cloud as a function of the time due can be calculated with the following equation (*M. Bettelli, et al, 2020*):

$$\sigma^2(t) = \sigma_0^2 + 2Dt + \frac{\mu N e}{2\sqrt{5}\epsilon}\int_0^t \frac{dt'}{\sqrt{\sigma^2(t')}} \qquad (1.23)$$

where $\boldsymbol{\sigma_0}$ is the initial width (express as variance), $\boldsymbol{D = \mu k_B T/e}$ is the diffusion coefficient, $\boldsymbol{T}$ is the absolute temperature, $\boldsymbol{N}$ is the number of charges and $\boldsymbol{\epsilon}$ is the electric permittivity of the semiconductor.

To simplify, the size of the electron cloud can be approximated by a Gaussian distribution (*Bolotnikov et al., 2007; Kim et al., 2011*) and express as:

$$\sigma = \sqrt{2\frac{k_B T d L}{eV}} \qquad (1.24)$$

where ***d*** is the drift distance, ***L*** is the detector thickness, ***e*** is the charge of the electrons and ***V*** is the cathode bias voltage. Another reason for cloud broadening, is related to the secondary products of X-ray interaction in the material. This includes the emission of K-edge characteristic X-rays which are reabsorbed far from the original interaction point. Indeed, at energies greater than the K-shell absorption energy of the CZT material (saw in table 1.4), fluorescent X-rays are also emitted (approximately 70% of all photoelectric absorptions in the CZT material result in K-edge characteristic X-rays) (*Abbene et al., 2018a*).

Electron cloud broadening is a very important aspect, and produces relevant effects in multi-electrode devices, in fact in detectors where the size of the electrodes and the gap between them is comparable to the size of the electron cloud it is observed that the electronic cloud can be splitted between two or more electrodes giving rise to the effect called “charge sharing” (Figure 1.28).

Charge sharing in segmented CZT detectors was studied extensively using numerical simulations, with validations through experimental measurements. Since shared events mainly occur with photon interactions near the interpixel gap, a coarse approximation of the percentage of shared events between adjacent pixels can be simply given by the ratio of the inter-pixel gap area to the total detector area.

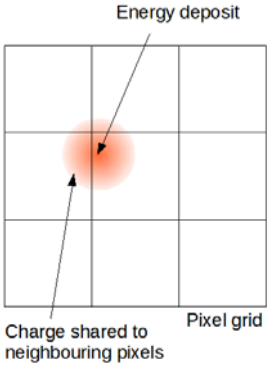

Figure 1.28 *Charge sharing scheme, the electronic cloud (in red) is “shared” between more pixels.*

In literature (*Iniewski et al. 2007*) was proposed an analytical model to calculate the probability of shared events through the geometric characteristics of the detectors, taking electron cloud broadening into account. Experimental validations of the model have been presented by several groups (*Kuvvetli et al., 2007; Veale et al., 2014b*). According to this model (*Iniewski et al., 2007*), the probability P of sharing between two adjacent pixels is given by:

$$P = 1 - \frac{(a + 2c - s)^2}{(a + g)^2} \qquad (1.25)$$

where $\boldsymbol{a}$ is the pixel size, $\boldsymbol{g}$ is the inter-pixel gap and $\boldsymbol{s}$ is the diameter of the electron cloud calculated by eq. 1.24 as: $s = 2.355\sigma$. The parameter $\boldsymbol{c}$ is the collection width describing the width over which a pixel collects the total charge deposited in an interaction (*Iniewski et al., 2007*), and for a small inter-pixel gap it can be expected to be close to 0.5g (*Veale et al., 2014b*).

Detection of charge-sharing events is generally performed through a time coincidence analysis (TCA), which consist of detecting the events of the pixels that are in temporal coincidence within a selected coincidence time window (CTW). These coincidence events can be removed from the spectrum, this technique is named charge-sharing discrimination (CSD), the application of the CSD involves a throughput worsening.

To recover the rejected shared events and so enhance the throughput, charge-sharing addition (CSA) technique was performed, which consists of summing the energies of the coincidence events.

Nevertheless, the energy obtained after summing the coincidence pulses of two adjacent pixels is often lower than the expected value.

Several explanations have been given for the presence of charge losses after CSA due to charge sharing (*Abbene et al., 2018a*):

a) a non-zero energy threshold of the electronics;
b) electric field distortions in the inter-pixel gap;

In the first case, when charge sharing occurs, a small amount of charge can be collected by a pixel, however this charge can be so small that it is below the energy threshold, so it will not be detected.

In the second explanation, charge can also be physically lost in the gap between pixels where electric field distortions are present (*Bolotnikov et al., 1999, 2014, Hubert Chen, 2002*). In many cases, due to the high conductivity of the surface compared with that of the bulk, some fraction of the electron cloud can reach the surface between adjacent pixels and thus not be collected by the pixel. These losses can be reduced by decreasing the size of the interpixel gaps or by using steering electrodes between the pixels (*Abbene et al., 2007; Kalemci & Matteson, 2002*).

1.4.4 Cross-talk

By TCA ones can also observe cross talk events, a kind of these are the transient pulses: in which the charges of an event fully collected by a pixel, generate a small induced-charge pulse on adiacent pixels.

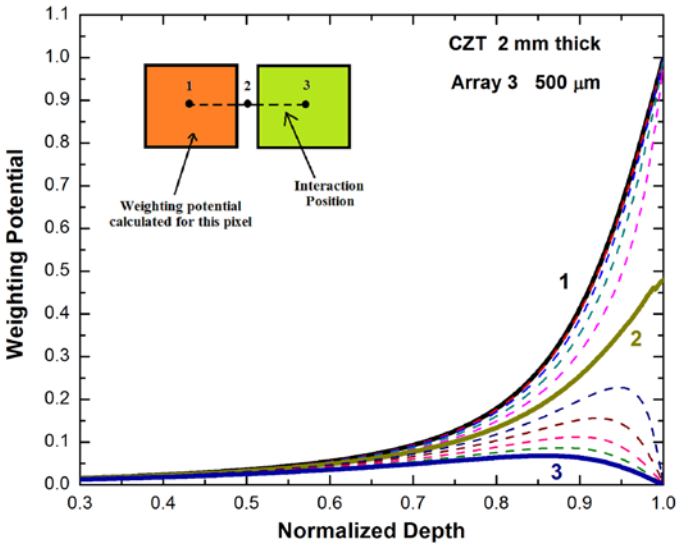

Figure 1.29 *The weighting potential of a reference pixel (orange pixel) at different interaction points, up to the centre of the adjacent pixel (green pixel) (Abbene et al., 2018a).*

The transient pulses are created by the particular shape of the weighting potential of a pixel detector, which is characterized by non-zero values even for interaction far from the collecting pixel. Figure. 1.29 shows an example of weighting potential of a reference pixel (orange pixel) at different interaction points, up to the centre of the adjacent pixel (green pixel).

The weighting potential was calculated by solving the Laplace equation (COMSOL Multiphysics software; https://www.comsol.com/).

These transient pulses are generally characterized by a different shape from the typical collected-charge pulses: they rise as the electron cloud moves to the collecting pixel and then rapidly decrease to zero as the electrons are collected this effect is known as ***weighting potential cross talk***. These pulses, measured in temporal coincidence with the collected pulses, are strongly used for both spatial and energy resolution improvements in gamma-ray detectors.

Whenever charge sharing occurs, both collected and induced-charge (transient) signals are generated on the neighbouring pixels. The transient contribution can alter the collected-charge signal by lowering the total energy after summing (*Abbene et al., 2018a*).

When charge sharing does not occur, an interaction near the edge of the pixel can also create a transient pulse on the adjacent pixel, thus generating false signals that increase the total energy after summing (*Kim et al., 2014*).

Moreover, fluorescent X rays, escaping from the pixels, can also produce cross-talk events between pixels (as shown in figure 1.30),

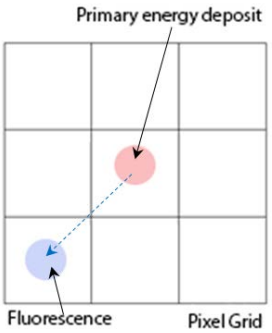

Figure 1.30 *Schematically example of a cross talk event in which primary (red) and fluorescent (blue) event are recorded by different pixels.*

2. HIGH-BIAS VOLTAGE CZT PIXEL DETECTORS

Sub-millimetre CZT pixel detectors with high-bias voltage operation were developed. In this chapter, the spectroscopic performance of these new detectors will be presented taking into account the mitigation and correction of charge sharing effects. The prototypes represent the basic detection system of spectroscopic imagers for the next generation X-ray scanners for food safety inspections.

2.1. The Avatar X Project

Recently, the *Detector & Electronics* research group of the Department of Physics and Chemistry of Palermo (DiFC Emilo Segrè) was in involved to lead the AVATAR X project funded by the Italian Ministry for University and Research (MUR). The goal of the project is the development of prototypes of innovative energy resolved photon counting (ERPC) X-ray imaging systems able to operate under high photon fluxes (input counting rates > 10^6 cps per pixel). The systems cover the 5-140 keV energy range, very appealing for several applications in which the improvement of X-ray image quality with minimum radiation exposure times is continuously desired: from medical imaging to security screening, food inspection, non destructive testing and analysis of materials. Innovative detectors and electronics were proposed. The proposed ERPC systems (Figure 2.1) are constituted of Cadmium-Zinc-Telluride (CZT) pixel detectors coupled to low noise and high-speed Application Specific Integrated Circuits (ASICs) followed by innovative Digital Pulse Processing (DPP) electronics.

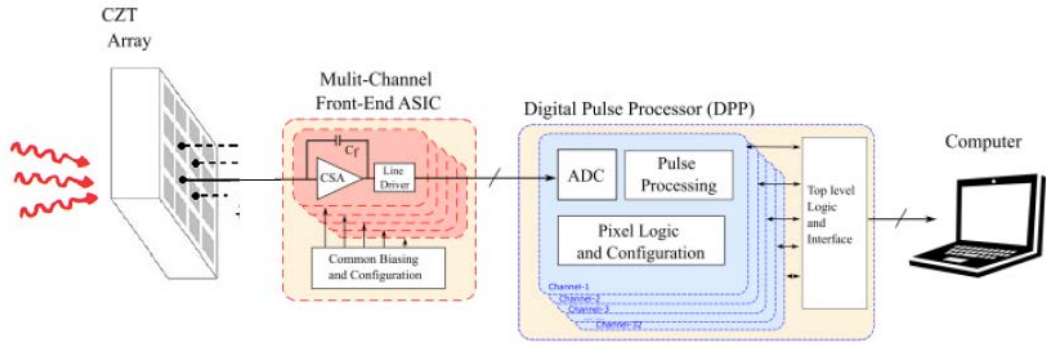

Figure 2.1 Schematic view of the proposed ERPC system architecture.

The research activities are focused to achieve high energy-spatial resolution even at high throughputs:

i. high energy resolution (< 5% (3 keV), 4% (4.9 keV) FWHM at 60 keV and 122 keV, respectively);
ii. capability to work under ultra-high photon fluxes (up to 10^6 cps);
iii. high position resolution (below 500 μm);
iv. performances time stability.

The system, due to the flexibility of the digital signal processing approach, will be able to work at different flux-resolution conditions, following the needs of several X-ray imaging applications. In particular, this triggers with the requirements of detection of defects and contaminants in food safety inspections, a very hot topic in Europe and worldwide.

The project also involves the collaboration of the IMEM/CNR of Parma (Italy) and the Rutherford Appleton Laboratory (UK).

2.2. CZT Pixel Detectors

New CZT pixel detectors with high-bias voltage operation (> 5000 $V \cdot cm^{-1}$) were developed. All detectors are characterized by the same electrode layout shown in Figure 2.2.

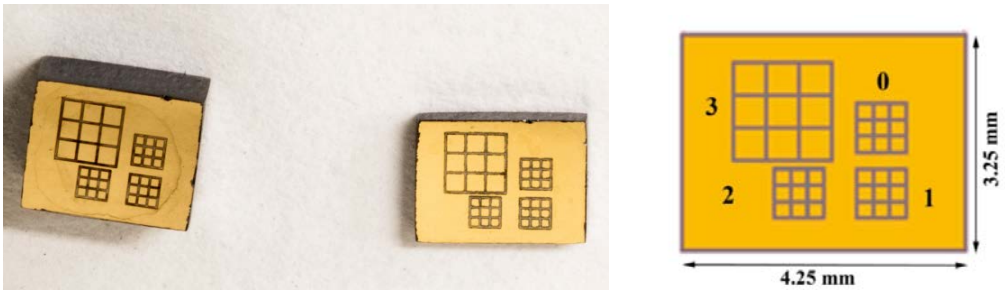

Figure 2.2 *Anode layout of the investigated CZT pixel detectors. Each detector is characterized by four arrays of 3x3 pixels with pixel pitches of 500 μm and 250 μm.*

The anode layout is characterized by four arrays of 3x3 pixels with pixel pitches of 500 μm and 250 μm, the width of the inter-pixel gaps for all arrays is equal to 50 μm; the arrays are surrounded by a guard-ring electrode (Figure 2.2), while the cathode is a planar electrode. Different CZT pixel detectors were investigated (Table 2.1), which crystals are based on traveling heater method (THM) and boron oxide encapsulated vertical Bridgman (B-VB) growth techniques:

A. B-VB CZT detectors;
B. Low Flux- LF-THM CZT detectors;
C. High Flux- HF-THM CZT detectors.

- Detectors A are CZT pixel detectors fabricated by IMEM-CNR of Parma and due2lab s.r.l. (Reggio Emilia, Italy; http://www.due2lab.com).
  These detectors are based on CZT crystals (4.25 x 3.25 x 1 mm^3) grown by the boron oxide encapsulated vertical Bridgman (B-VB) technique *(Abbene et al., 2016; Zappettini et al., 2007, 2009).* Gold electroless contacts were realized on both the anode, prepared by using water solutions, and the cathode, prepared using alcoholic solutions *(Benassi et al., 2017; Marchini et al., 2009).*

B-VB CZT detectors, with gold electroless contacts, are characterized by good room-temperature performance and high-bias voltage operation (electric field up to 10000 $V \cdot cm^{-1}$) *(Abbene et al., 2016)*.

- Detectors B are 3 mm thick CZT pixel detectors realized at IMEM/CNR of Parma from commercial CZT crystals provided by Redlen (Canada) (4.25 x 3.25 x 3 mm^3) grown by the using the travelling heater method (THM) technique. Contact deposition has been realized using gold electroless technique (by IMEM/CNR), like the detectors A.

- Detectors C are based on new CZT crystals (4.25 x 3.25 x 2 mm^3), grown with the traveling heater method (THM) technique with platinum contacts.
  These detectors are entirely produced by Redlen Technologies (Canada) and characterized by enhanced hole charge transport properties to minimize radiation induced polarization at high fluxes (*Abbene et al., 2018b; Veale et al., 2020; Koch-Mehrin et al, 2021*).

Table 2.1 *Characteristics of the CZT pixel detecors.*

DETECTOR	Dimension (mm^3)	Crystal grown technique	Contact deposition	Supported electric field ($V \cdot cm^{-1}$)
(A) B-VB CZT	4.25 x 3.25 x 1	Boron Encapsulated Vertical Bridgman	Gold electroless	10000
(B) LF-THM CZT	4.25 x 3.25 x 3	Travelling Heater Method	Gold electroless	6000
(C) HF-THM CZT	4.25 x 3.25 x 2	Travelling Heater Method	Platinum	5000

2.3. Analog Front-end Electronic: PIXIE

A low-noise ASIC (PIXIE ASIC), developed at RAL (*Allwork et al., 2012; Veale et al., 2011*), was used as charge-sensitive preamplifier (CSP). The PIXIE ASIC consists of four arrays of 3 x 3 pixels (Figure 2.3), flip-chip bonded directly to the detector pixels.

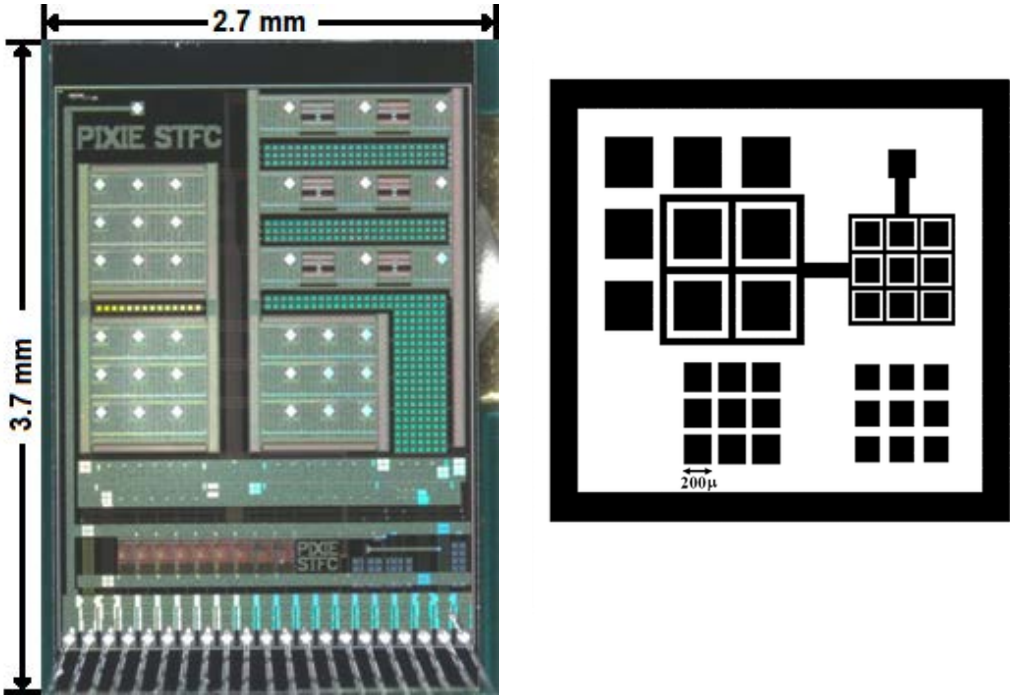

Figure 2.3 *PIXIE ASIC**: a)** photo of circuit, **b)** detector geometry of four pixels array.*

The active circuitry of each pixel is a Charge Sensitive Preamplifier (CSP) (with no shaping filter) and an output buffer which is multiplexed directly off the chip. The nine outputs from each of the four arrays are multiplexed onto a common nine-track analogue bus which is driven off-chip by the output buffers. The outputs of all nine pixels of the selected array are read out simultaneously, allowing analysis of the height and shape of the output pulses from the CSPs.

The ASIC has two selectable ranges: a high-gain mode sensitive up to 150 keV and a low gain mode that allows measurements up to 1.5 MeV. A calibration circuit in the central pixel of each array allows a pulser signal to be passed through the CSP. The feedback circuit was designed to provide detector leakage-current immunity of up to 250 pA per pixel.

The pulses are characterized by rise times less than 60 ns and a noise level (ENC) less than 80 electrons. The bonding process was performed at RAL using low-temperature curing (<150°C) via the silver-loaded epoxy and gold stud-bonding technique (*Schneider et al., 2015*).

Another advantage of the PIXIE ASIC is that multiple contact geometries can be tested on the same crystal. The use of a single piece of CZT removes some of the uncertainty introduced from comparing different contact structures on different pieces of material. By digitizing the output of each channel, it is also possible to directly study the effect of contact geometry on the shape of pulses generated by X-ray events.

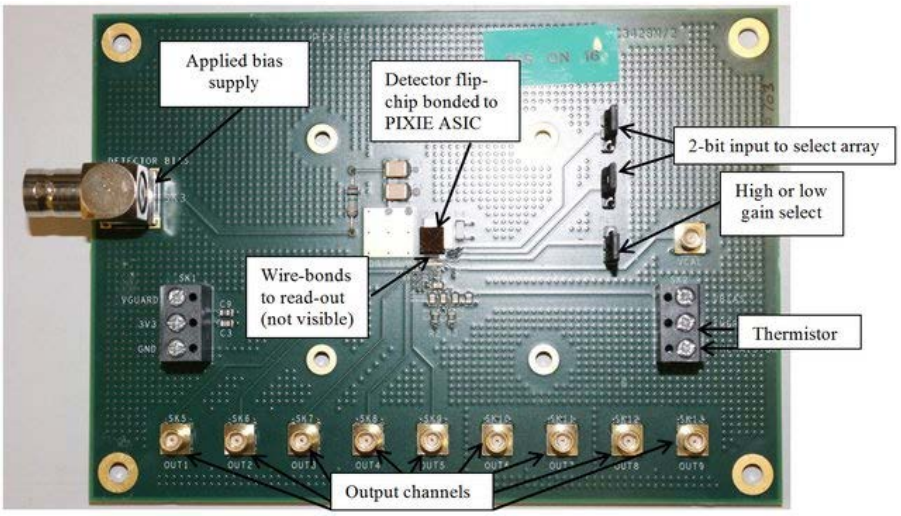

Figure 2.4 *PIXIE board in which components are highlighted.*

2.4. Digital Pulse Processing Electronics

The output waveforms from the PIXIE ASIC are digitized and processed by custom digital electronics. The digital system was developed at the DiFC of the University of Palermo (*Abbene et al., 2013, Abbene & Gerardi, 2015; Gerardi & Abbene, 2014*).

The digital electronics is able to perform a real-time pulse shape and height analysis (event arrival time, pulse height, pulse time width etc.) of the CSP waveforms, even at high rates and different throughput and energy-resolution conditions. The digital system consists of four digitizers (DT5724, 16-bit, 100 MS s^{-1}, CAEN S.p.A., Italy; http://www.caen.it) and a PC, through which the user can control all the digitizer functions, the acquisition and the analysis. The digitizers are connected and synchronized to realize a digitizing system with 16 channels (Figure 2.5).

Figure 2.5 *The 16-channel digital readout electronics. The central box is the clock splitter used to synchronize all digitizers.*

The digital pulse processing (DPP) analysis is performed using custom DPP firmware uploaded to the digitizers (Figure 2.6). The DPP firmware is able to perform two different shaping analyses: a fast and a slow pulse shape and height analysis (PSHA). To ensure high throughputs even at high rates, one only used the

fast PSHA. Despite the short time widths of the output shaped pulses, the fast-shaping analysis allows reasonable energy resolution at both low and high rates.

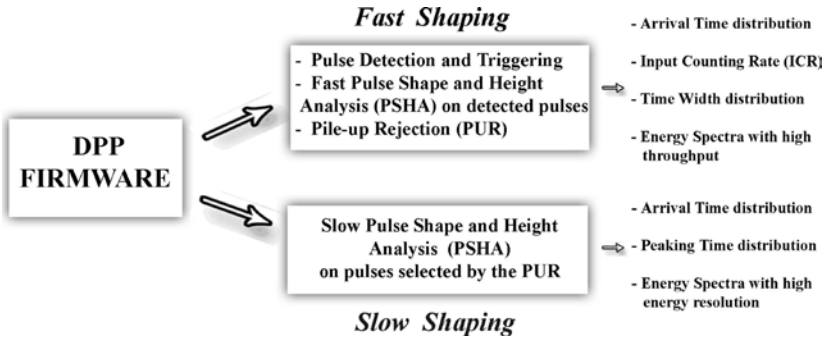

Figure 2.6 *The main operations and output data of the digital pulse processing (DPP) system.*

The digital analysis starts with the shaping of the output waveform from the detector ASIC using the classical single delay line (SDL) shaping technique (*Knoll, 2000*). SDL shaping is obtained by subtracting from the original pulse its delayed and attenuated fraction. SDL shaping gives short rectangular output pulses with fast rise and fall times (Figura 2.7).

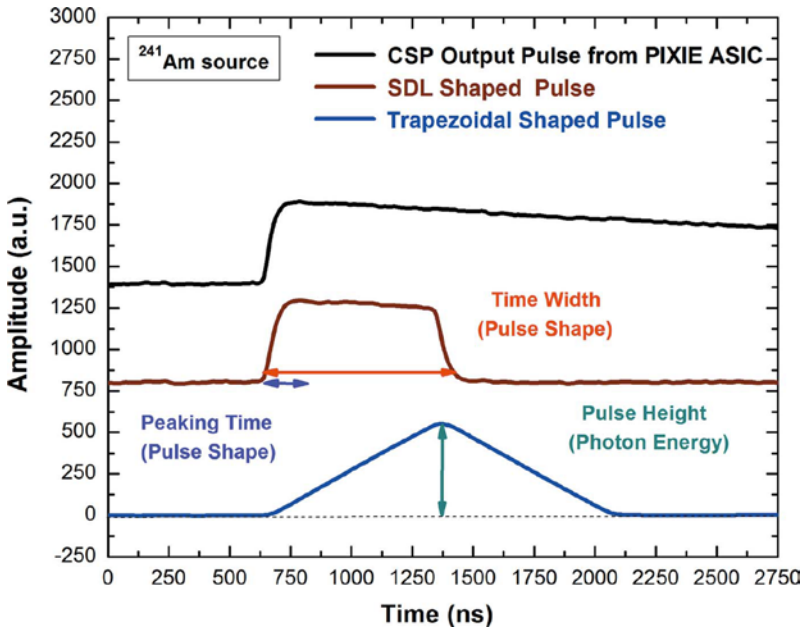

Figure 2.7 *A typical CSP pulse from the PIXIE ASIC (brown line) and from the digital system after fast SDL shaping (black line) with a delay time of 700 ns and after trapezoidal filtering (blue line).*

Generally, two main features characterize SDL shaping: (i) the time width of each SDL shaped pulse is well defined (delay time + CSP peaking time); and (ii) if the delay time is greater than the peaking time of the preamplified pulse, the SDL shaping also preserves the leading edge (pulse height and peaking time) of each CSP output pulse. These features make SDL shaping very appealing for timing and PSHA at both low and high rates. To increase the SNR a further shaping with a trapezoidal filter (Figura 2.7) was also performed. Through the fast PSHA, the system is able to provide, for each CSP pulse, the following results, recorded and presented in list mode:

(i) the arrival time;
(ii) the height of the fast SDL shaped pulses after baseline restoration and trapezoidal filtering, i.e. the energy of each event;
(iii) time width (TW) of the fast SDL shaped pulses and its relation to the pulse height can be very helpful for improving the detector performance (*Abbene et al., 2015, 2017*),.

To minimize the effects of baseline shifts in the measured spectra, especially at high rates, the system performs a fast baseline recovery using the running average of a fixed number of samples preceding the SDL pulse, where no further pulses are present.

An important feature of the digital system is that the deadtime is well defined. The time width of the pulses from fast shaping is a dead-time for the system, following a well-known model (paralysable dead-time) (*Knoll, 2000*). In particular, the fast PSHA is characterized by a dead-time equal to the mean of the time widths of the fast shaped pulses. As shown by Abbene and Gerardi, *(2015*), the true input counting rate (ICR) can be estimated from an exponential best fit of the measured time-interval distribution (TID) of the fast shaped pulses, or by inverting the throughput formula of the fast analysis (paralysable model).

To perform pulse shape analysis, the DPP system carried out the measurement of the peaking time of the analyzed pulses (after SDL shaping). First the rise time of the pulses is evaluated, i.e. the interval between the times at which the shaped pulse reaches 10% and 90% of its height (after baseline restoration). The times,

corresponding to the exact fractions (10% and 90%) of the pulse height, are obtained through a linear interpolation. Estimate the peaking time is equal to 2.27 times the rise time (i.e. about five times the time constant). Due to the precise measurement of the pulse height-baseline and interpolation, the method allows fine peaking time estimations (with a precision of 2 ns) both at low and high photon counting rates.

The system can also provide a sequence of CSP output pulses together with the related arrival times, within selected time windows (snapshots) centred on each pulse peak position. This working mode is very helpful for performing a quick look and further off-line analysis on the CSP output pulses.

2.5. Experimental Set-up

The detectors and CSPs are placed into a metallic box (Figure 2.8) that provides shielding from electromagnetic interferences. A thin beryllium window allows detector irradiation.

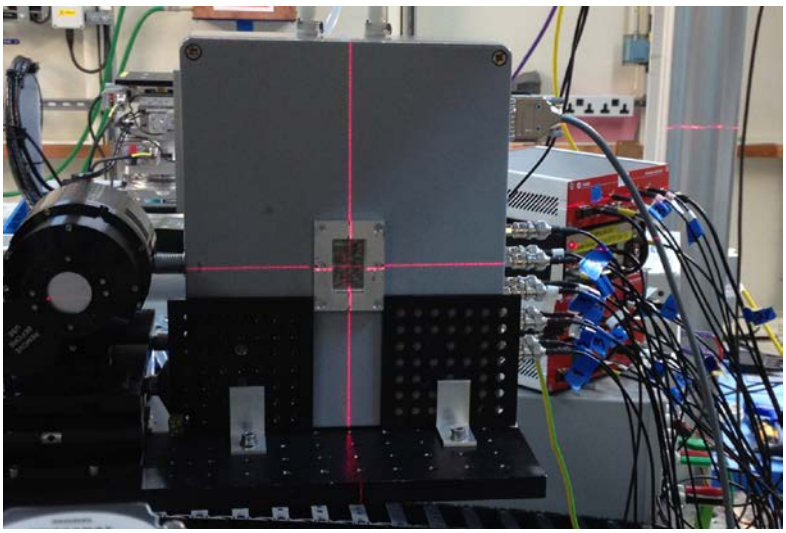

Figure 2.8 *The experimental setup used.*

The experimental activities concerning the spectroscopic characterization of the detectors were carried out at the *"Detectors & Electronics"* laboratory of the "E. Segrè" Department of Physics and Chemistry of the University of Palermo.

The spectroscopic response of the detectors was investigated by using uncollimated X-ray and gamma-ray calibration sources (^{109}Cd: 22.1, 24.9 and 88.1 keV; ^{241}Am: 59.5 and 26.3 keV; ^{57}Co: 122.1 and 136.5 keV). The ^{57}Co energy spectra also feature the W fluorescent lines produced in the tungsten source backing ($K_{\alpha 1}$ = 59.3 keV, $K_{\alpha 2}$ = 58.0 keV, $K_{\beta 1}$ = 67.2 keV, $K_{\beta 3}$ = 66.9 keV). The source holders shield the 14 keV gamma line of the ^{57}Co source and the Np L X-ray lines of the ^{241}Am source.

The detectors were irradiated from the cathode side, negatively biased. All measurements were performed at temperature T= 20°C, kept constant by a dedicated cooling system.

Measurements with collimated synchrotron X-ray beams were done at the Diamond Light Source (UK). Diamond Light Source is located in the Harwell Science and Innovation Campus (Didcot, UK) and operated by the Science and Technology Facilities Council.

Figure 2.9 *Diamond Light Source Synchrotron at the Harwell Science and Innovation Campus.*

X-ray photons, generated in a ring by accelerated electrons close to light speed, are directed into a series of beamlines that are tangential to the ring. To perform these measurements beamline B16 was used, this beamline is suitable to test optics and detectors, its principal specifications are:

(i) selectable photon energy in the range of 4÷50 keV;

(ii) adjustable beam size donw to 10x10μm^2;

(iii) adjustable beam position with micrometric precision.

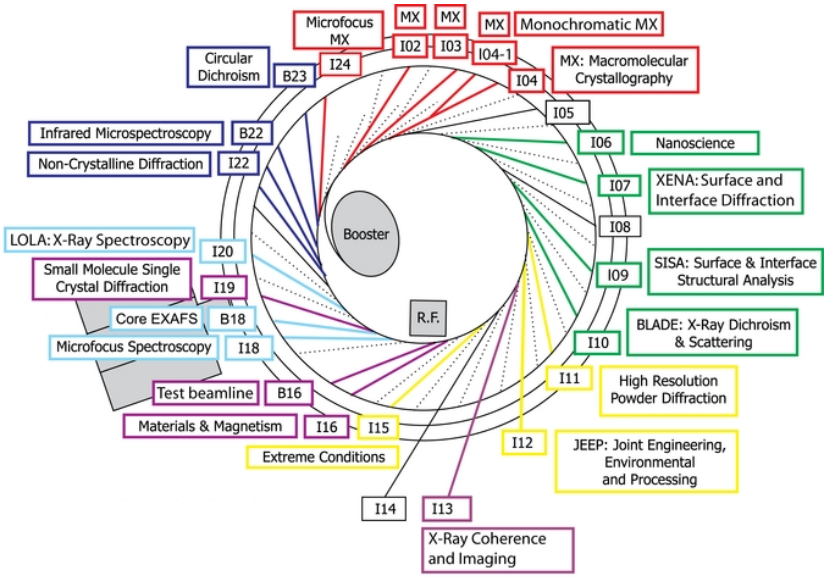

Figure 2.10 *Diamond Light Source map.*

High-rate measurements were performed at the Livio Scarsi Laboratory (LAX) of the University of Palermo. A Seifert SN60 tube equipped with different targets (Ag, Co, Cr, Cu, Fe, Mo and W) allows the production of X-rays in the 1–60 keV energy range and with fluence rates of 10^5–10^8 photons mm^{-2} s^{-1} (*Principato et al., 2015*). In this work, X-rays from a Mo target were used. The experimental setup used at LAX is shown in Figure 2.11.

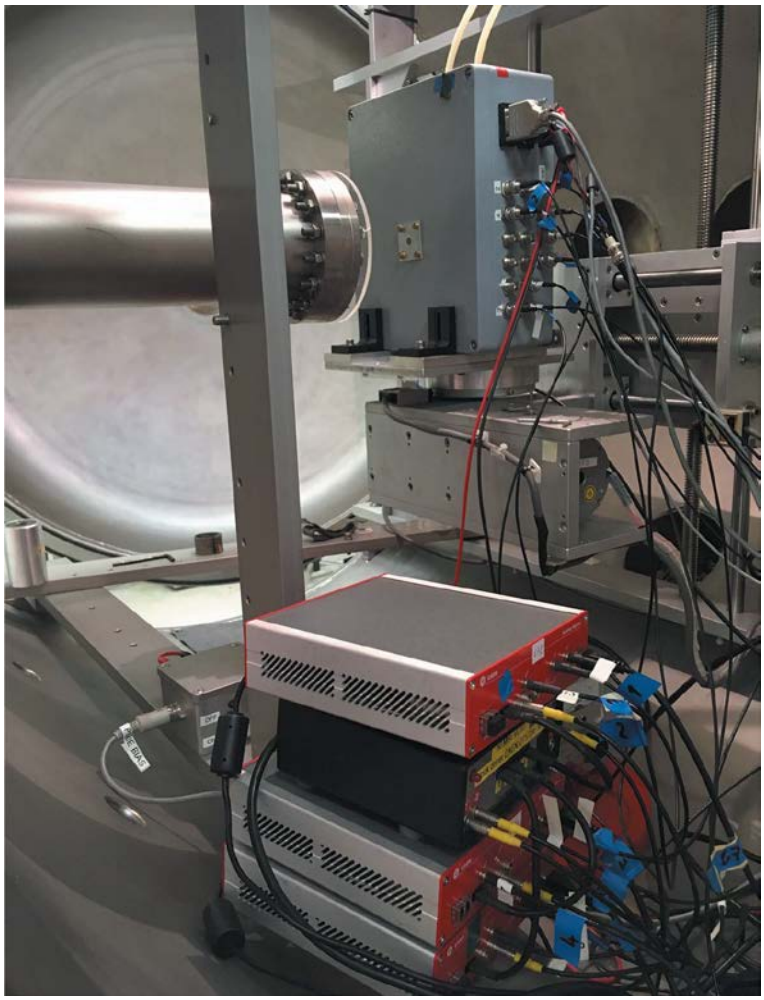

Figure 2.11 *Experimental setup at Livio Scarsi Laboratory (LAX) of the University of Palermo.*

2.6. Measurements and Results

In this section, the spectroscopic response of the detectors will be shown, taking into account the charge sharing effects and possible corrections. Sub-pixel investigations were performed with synchrotron X rays. High-flux radiation polarization effects were also studied.

2.6.1 Spectroscopic response and energy resolution

Figure 2.12 shows the energy resolution at different cathode bias voltages of a selected pixel of large array (with pitch 500 μm) of the detector A (B-VB CZT). The results highlight the high-bias voltage operation of the detectors, up to 9000 $V \cdot cm^{-1}$. This is due to the low leakage current of the detectors; despite the quasi-ohmic contacts of the electrodes, they allow low-leakage currents even at high voltages (38 $nA \cdot cm^{-2}$ at 10000$V \cdot cm^{-1}$).

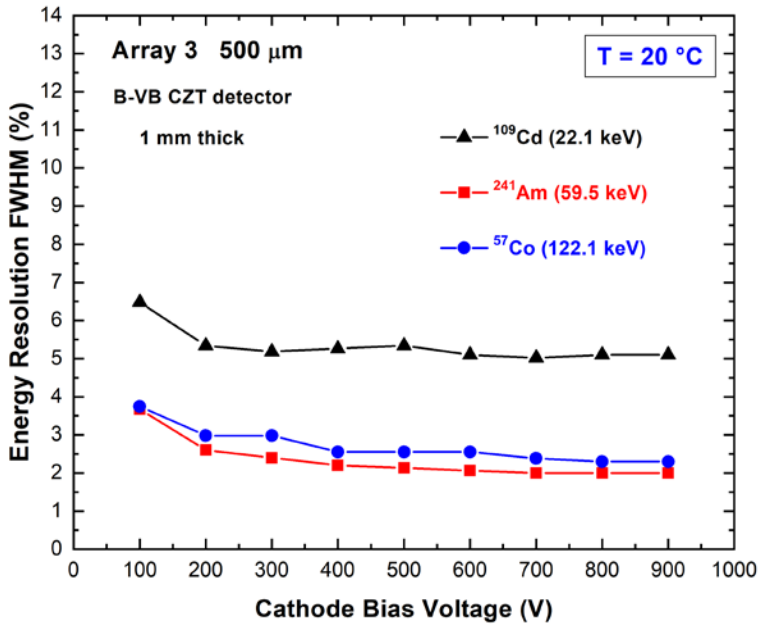

Figure 2.12 *Room-temperature energy resolution (FWHM) of a selected pixel (n° 8) of the large array 3 (500 μm) of B-VB CZT detector (A) at different cathode bias voltages. The energy-resolution values of the detector at the main energies of uncollimated radiation sources are reported.*

.

The bias voltages used during the experiments are indicated in table 2.2
Linear energy calibration was measured for all pixels and detectors (Figure 2.13).

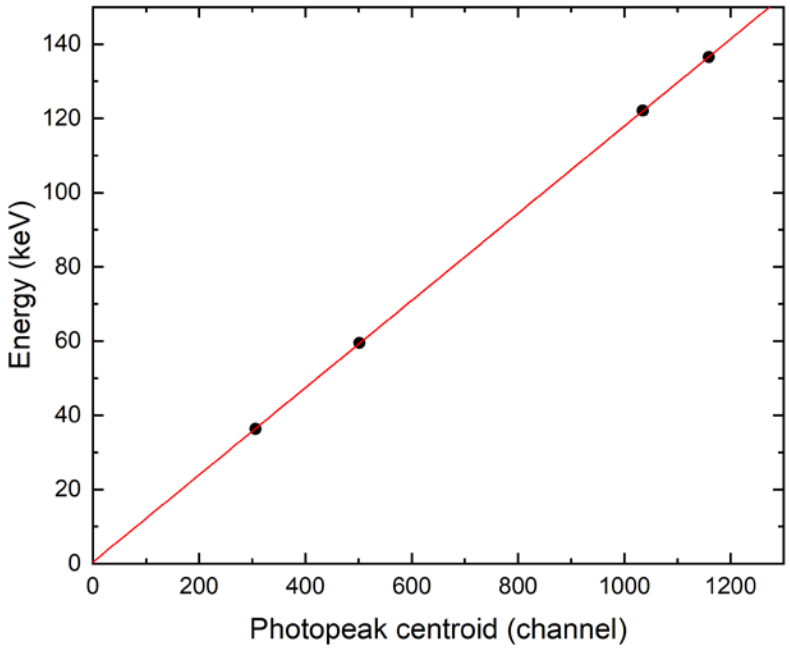

Figure 2.13 *The centroid of the pulse height spectrum at different photon energies for the pixel N°8 of the large array 3 (500 μm) of LF-THM detector (B).*

An overview of the low-rate performance of the pixels of the arrays is presented in figures. 2.14 and 2.15. Despite the good room-temperature performance of the pixels of the large array, poor energy resolution characterizes the measured spectra of the pixels of the small array, as shown in figure 2.15(b). This can be attributed to the charge-sharing effects that are more severe for small pixels and when the gap-area-to-pixel area ratio is increased. The room-temperature energy resolution values are reported in table 2.2.

Table 2.2 *Spectroscopic performance of the best pixels of the detectors at T = 20°C.*
The Fano noise was calculated by using a Fano factor F = 0.1 (Devanathan et al., 2006; Kuvvetli & Budtz-Jorgensen, 2005; Owens & Peacock, 2004). No charge-sharing corrections were applied. The poor energy spectra of the small arrays of detector B did not allow to measure energy reolution (see figure 2.15b).

DETECTOR (thickness)	Bias Voltage	Array (Pitch)	Energy resolution @ 22.1 keV (keV) Fano noise: 0.2 keV	Energy resolution @ 59.5 keV (keV) Fano noise: 0.4 keV	Energy resolution @ 122.1 keV (keV) Fano noise: 0.6 keV
(A) B-VB (1mm)	**900 V**	**N°3 (500 µm)**	**1.1 (5.1%)**	**1.2 (2.0%)**	**2.8 (2.3%)**
		N°0 (250 µm)	**0.9 (4.0%)**	**1.0 (1.7%)**	**1.6 (1.3%)**
(B) LF-THM (3mm)	**1800 V**	**N°3 (500 µm)**	**1.6 (7.3%)**	**1.7 (2.8%)**	**2.0 (1.6%)**
		N°0 (250 µm)	**----**	**----**	**----**
(C) HF-THM (2mm)	**1000 V**	**N°3 (500 µm)**	**1.2 (5.4%)**	**1.4 (2.4%)**	**1.8 (1.5%)**
		N°0 (250 µm)	**1.6 (7.2%)**	**1.7 (2.9%)**	**2.7 (2.2%)**

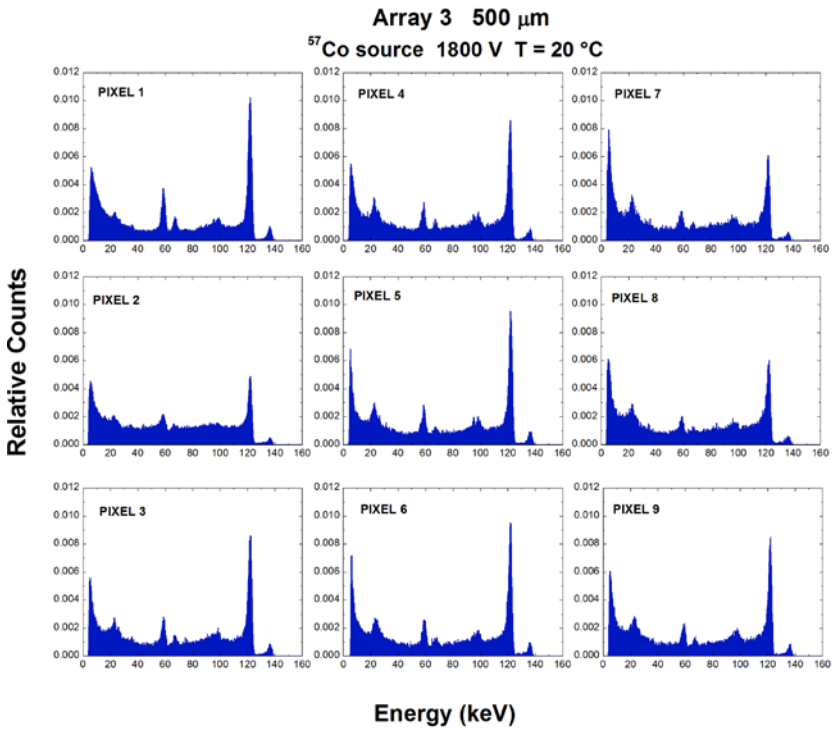

Figure 2.14 *The measured ^{57}Co spectra of all nine pixels of the large array 3 (500 µm) of detector B. The energy resolution (FWHM) of the best pixel (pixel 3) is 2.8% (1.7 keV) and 1.6% (2 keV) at 59.5 keV and 122.1 keV, respectively.*

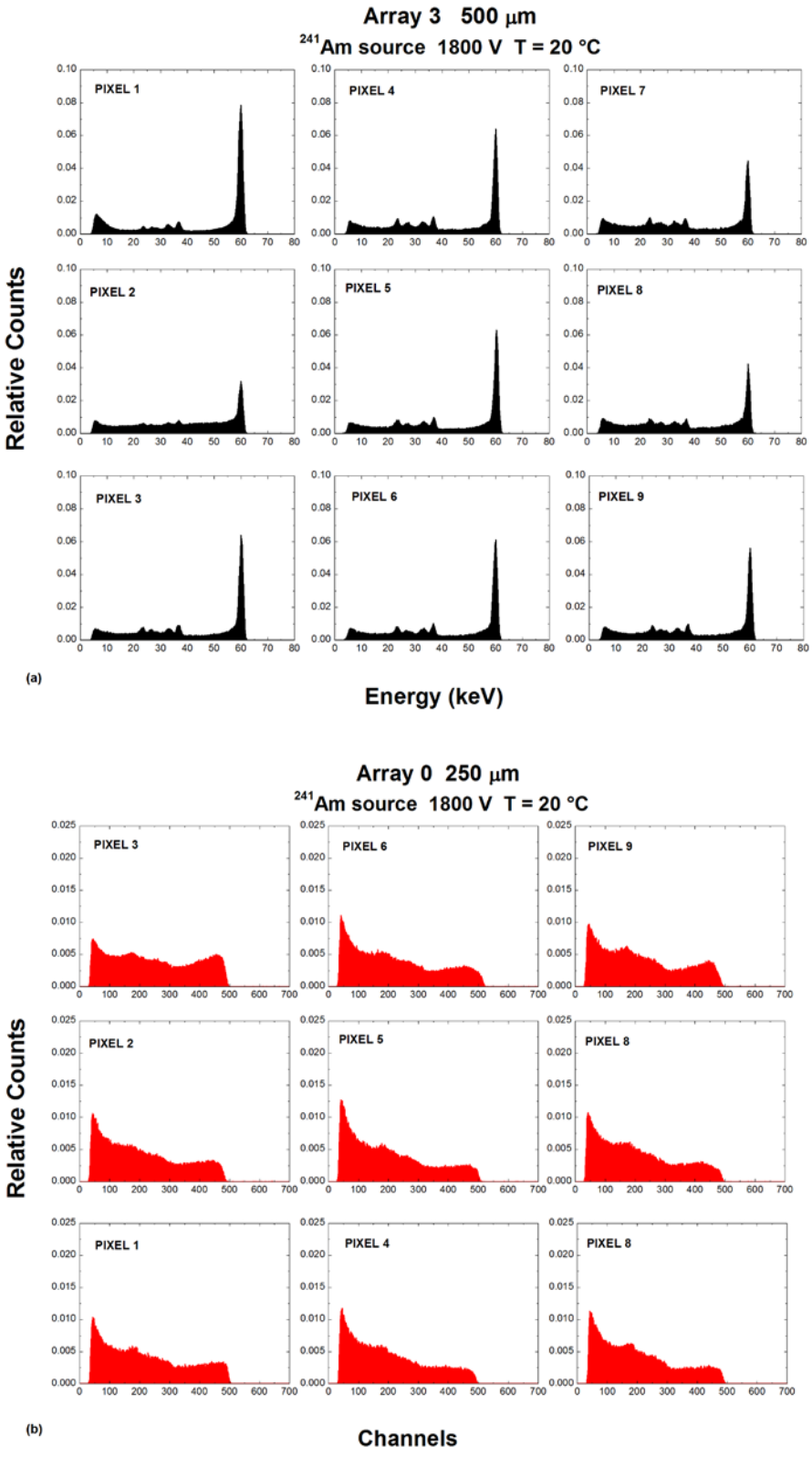

Figure 2.15 *Overview of the measured uncollimated ^{241}Am energy spectra of all nine pixels of large array (a) and small array (b) of detector B The energy resolution (FWHM) of the best pixel (pixel 3) of large array is 1.6% (2 keV) at 59.5 keV under low-rate conditions (< 600 counts s^{-1}). The poor energy resolution of the measured spectra of small array is caused by charge-sharing effects (ICR< 600 counts s^{-1}).*

2.6.2 Charge transport properties

The charge-carrier-transport properties were investigated through the estimation of the mobility-lifetime product of the electrons ($\mu_e \tau_e$). To evaluate the $\mu_e \tau_e$, the detectors were irradiated with the ^{109}Cd source from the cathode side and the energy spectra at different bias voltages were measured. Figure 2.16 show ^{109}Cd spectra for a pixel (n° 8) of big array of the detector A acquired at different cathode voltages.

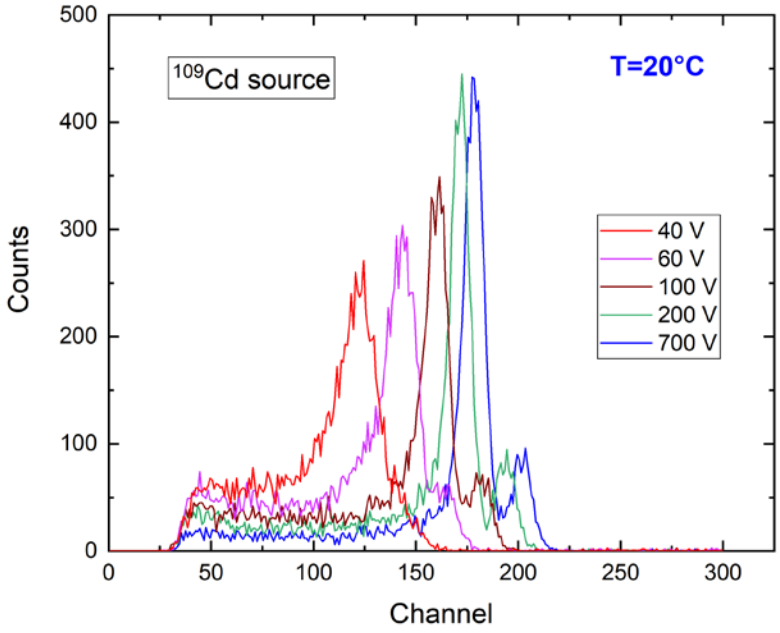

Figure 2.16 *Uncollimated ^{109}Cd energy spectra of a selected pixel of the large array of detector A (array 3: 500 μm pixel pitch) at different cathode bias voltages.*

Typically, the estimation of $\mu_e \tau_e$ e on planar detectors, where the weighting field can be considered uniform, is performed through the simplified Hecht equation (*Sellin et al., 2005*). In pixel detectors, the presence of non-uniform weighting potential and electric field (*Barret et al., 1995; Zanichelli et al., 2012*) limits the application of the Hecht equation in the estimation of $\mu_e \tau_e$. To account for these non-uniformities, charge-collection efficiency (CCE) was modelled through the equation 2.1, based on the Shockley–Ramo theorem (*He, 2001*),

$$CCE = \int_0^L exp\left[-\frac{x}{\mu\tau E(x)}\right] W(x)dx \qquad (2.1)$$

where x is the interaction depth, L is the detector thickness, W(x) is the weighting field and E(x) is the electric field. By simulating the weighting field W(x) of a pixel detector (COMSOL Multiphysics) and by modelling the electric field E(x) with a linear behaviour (*Zanichelli et al., 2012*), the CCE can be written as follows:

$$CCE = \int_0^L exp\left(-\frac{x}{\mu\tau\{(V/L) + \alpha[x - (L/2)]\}}\right) W(x)dx \qquad (2.2)$$

where α is the slope of the linear behaviour of the electric field E(x), and V is the applied bias voltage. CCE of a selected pixel of detector A at 22.1 keV versus the bias voltage is reported in Figure 2.17.

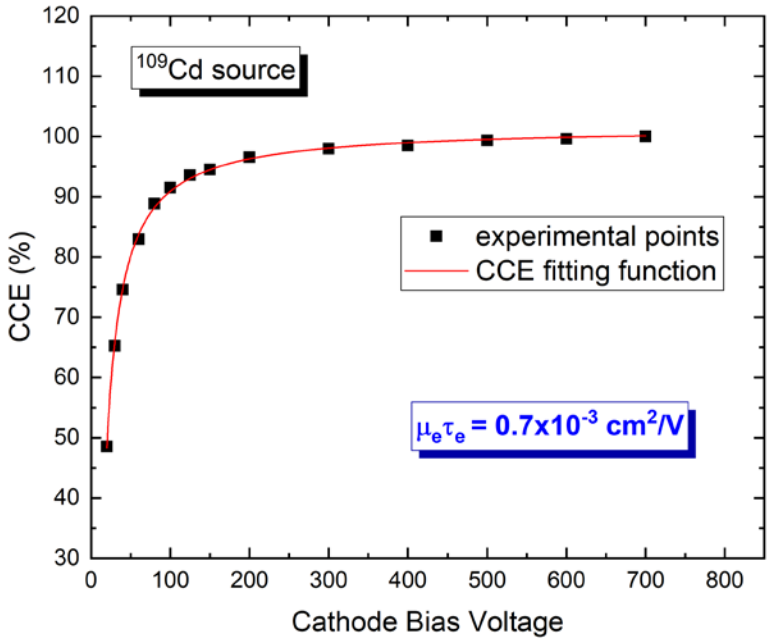

Figure 2.17 *CCE of a selected pixel of detector A at various cathode bias voltages. The fitting function [equation (2.2)] takes into account the non-uniform behaviour of both the weighting and the electric fields.*

Through a best-fitting procedure with equation 2.2, $\mu_e\tau_e$ values ranging from 0.6 to 0.7 x 10^{-3} $cm^2 \cdot V^{-1}$ (α values between -1.9 and -2 x 10^3 $V \cdot cm^{-2}$) was estimated for detector A (grown with B-VB technique). The estimated $\mu_e\tau_e$ values (5-10 x 10^{-3} $cm^2 \cdot V^{-1}$) for the THM grown detectors (B and C detectors) are in agreement with the typical values presented in the literature (*Chen et al.,2007; Awadalla et al., 2014; Chen et al.,2008*).

2.6.3 2-D mapping

To investigate the presence of non-uniformities, a 2D mapping of the detectors was performed with collimated synchrotron X rays. A 10x10 μm^2 micro-beam was scanned across the detectors for both the 500 and 250 μm pitch arrays, with scan steps of 25 and 12.5 μm, respectively.

The results of the mapping for detector B are shown in Figure 2.18, where the 40 keV photopeak energy at different positions is presented.

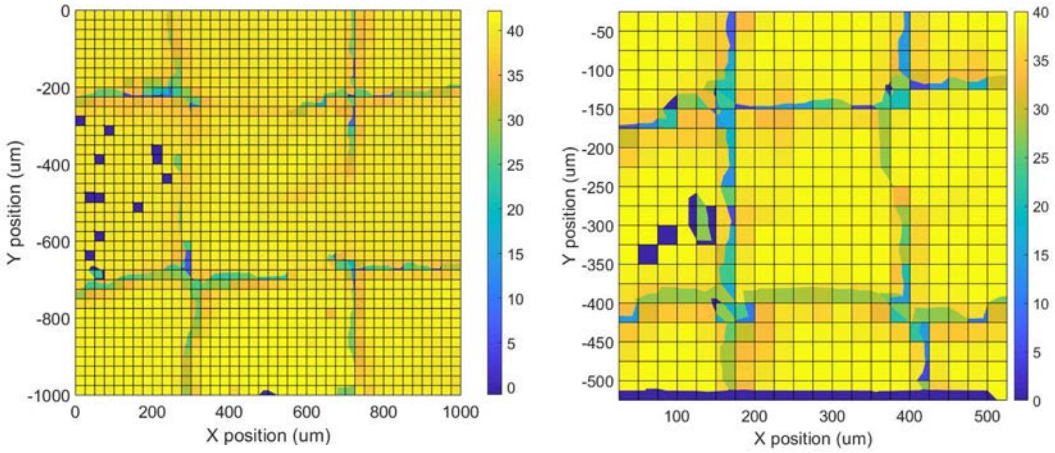

Figure 2.18 *The results of a 2D synchrotron mapping for the large (**a**) and small (**b**) pixel arrays at 40 keV. The changes in the photopeak energy are confined near the inter-pixel gaps because of charge-sharing effects. The violet squares are caused by acquisition failures.*

As clearly shown in figure 2.18, variations in the photopeak energy are mainly confined near the inter-pixel gaps because of charge sharing effects (as will be described in the next paragraph), violet squares are caused by acquisition failures.

2.6.4 Charge sharing measurements

Charge-sharing effects were also investigated. The shared events were analysed by detecting the events of a pixel which are in temporal coincidence, within a coincidence time window (CTW), with the neighbouring pixels. This technique is generally termed *time coincidence analysis* (TCA). Figure 2.19 shows an example of CSP output pulses related to a typical charge-sharing event (^{241}Am source) involving four pixels (event multiplicity m = 4) of small array 0 (250 μm pitch) of the detector C, within a CTWof 10 ns. The shape of the CSP output pulses is typical of collected-charge pulses and no pure transient pulses were observed.

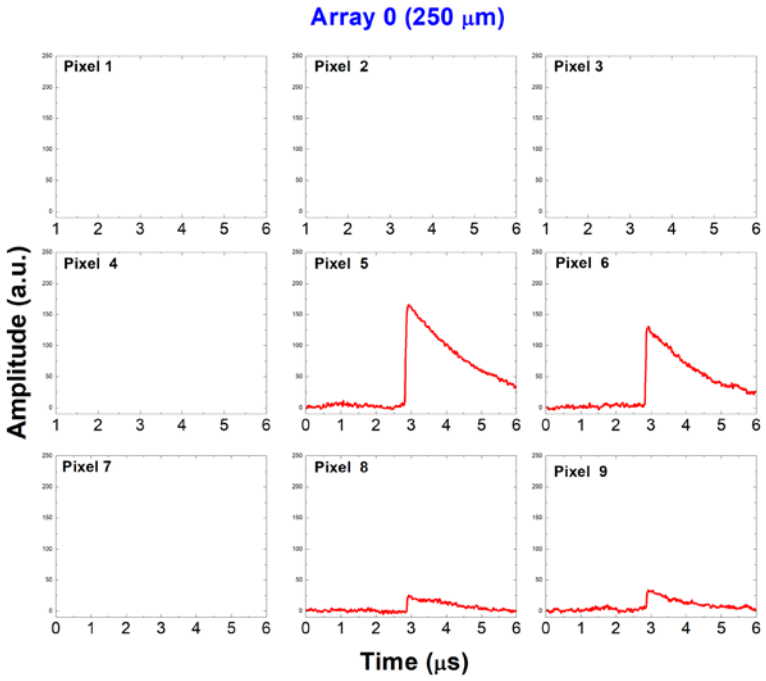

Figure 2.19 *Typical charge-sharing event (^{241}Am source) involving four pixels of small array 0 (250 μm) of the detector C. The pulses are in temporal coincidence within a CTW of 10 ns.*

In particular, the events of the central pixel (n° 5) of each array that are in temporal coincidence with the adjacent pixels were measured, within selected coincidence time windows (CTWs). The digital electronics allow fine TCA with CTWs up to 10 ns. Figure 2.20 shows the percentages of shared events of the central pixel with the eight adjacent pixels at different CTWs (for detector C).

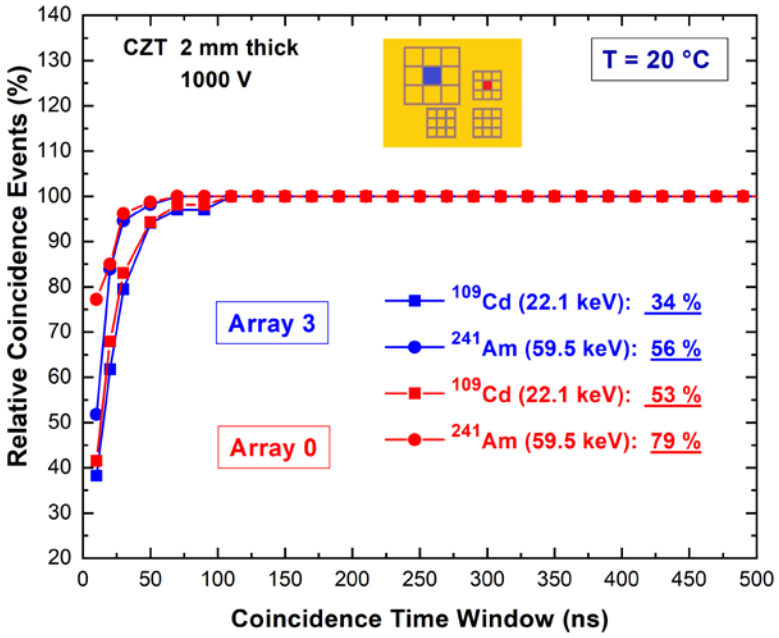

Figure 2.20 *Relative coincidence events (percentage) of central pixel 5 for arrays 3 (detector C) and 0 with all adjacent pixels at different CTWs and energies (^{109}Cd and ^{241}Am). An energy threshold of 3 keV for all pixels was used. The percentage values of the coincidence events of pixel 5 with all pixels, for both energies and arrays, are also shown (CTW of 450 ns).*

Almost all shared events (>94%) are detected within a CTW of 50 ns and the saturation of the curves clearly shows the full detection of the shared events within the investigated CTW range. Due to the higher G/A ratio, the small array (array 0) is characterized by more shared events; moreover, the difference in charge sharing between the energies below (^{109}Cd) and above (^{241}Am) the K-shell absorption energy of the CZT material points out the critical role of the X-ray fluorescence. Fluorescent X-rays broaden the initial electron cloud and can create cross-talk events in neighbouring pixels (side and back escape events).

In figure 2.21 are shown three different energy spectra of uncollimated 59.5 keV photons from ^{241}Am source, related to the central pixel of the 250 μm array of the detector C. The black line represents the energy spectrum of all events (raw spectrum) and the red line is the spectrum of the events in temporal coincidence with all eight neighbouring pixels.

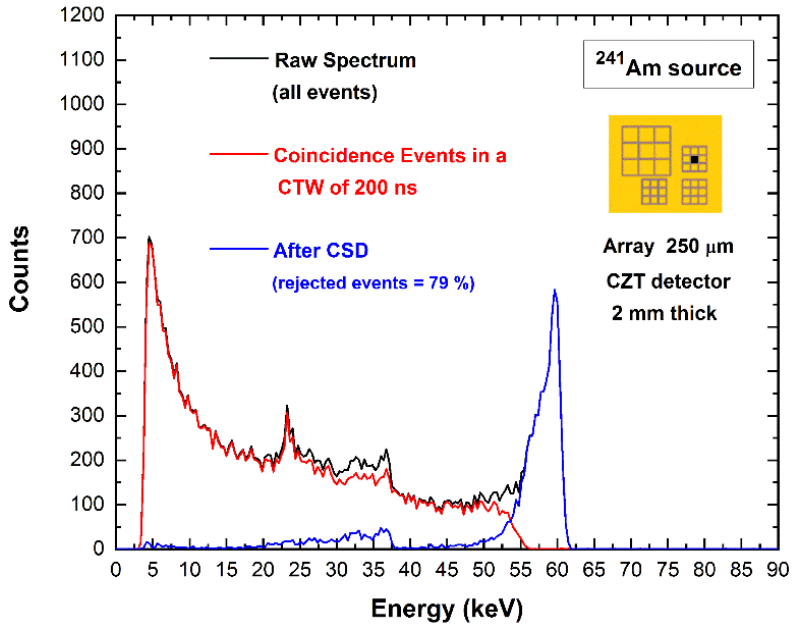

Figure 2.21 *Charge sharing measurements for the central pixel of the 250 μm array. The blue line represents the uncollimated ^{241}Am spectrum after charge sharing discrimination (CSD). The raw spectrum (black line) of all events and the spectrum of the coincidence events with all eight neighbouring pixels (red line) are also shown. The yellow inset shows the layout of the anode of the detector.*

As clearly visible in figure 2.21, the percentage of coincidence events is very high (79 %) and the typical distortions related to charge sharing and fluorescent cross talk are clearly visible: the fluorescent peaks and the low-energy background and tailing. The blue line is the spectrum after charge sharing discrimination (CSD), i.e. after the rejection of coincidence events (79%). The coincidence analysis was performed with a coincidence time window (CTW) of 200 ns, ensuring the detection of all events. The CSD works well allowing the rejection of all charge sharing distortions, even if produces a strong reduction of the pixel throughput and counting efficiency (79 % rejected events). The tailing below the main photopeak is not mitigated; these events are not in temporal coincidence with neighbouring pixels, due to their energies below the detection energy threshold (4 keV). Moreover, escape peaks are also present in the spectra even after CSD, due to fluorescence events escaping from the cathode or absorbed on the guard-ring.

The multiplicity *m* of the coincidence events represents the number of the involved pixels within a coincidence detection, was also measured (Figure 2.22).

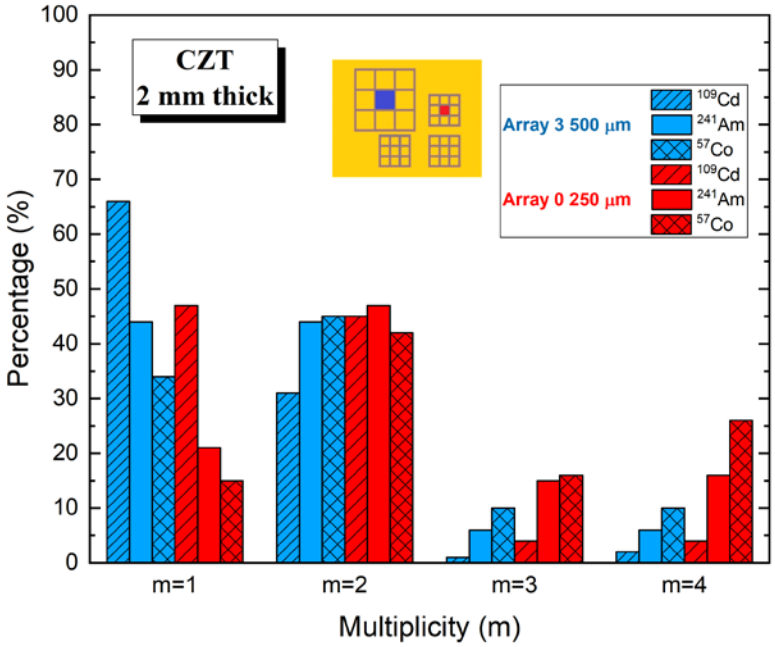

Figure 2.22 *The multiplicity m of the coincidence events of the central pixels for the 250 μm and 500 μm arrays. The multiplicity m is referred to the number of pixels involved in a coincidence detection.*

The multiplicity of the events of the central pixel for both arrays and at different energies was measured: ^{109}Cd (main energy line at 22.1 keV), ^{241}Am (main energy line at 59.5 keV) and ^{57}Co (main energy line at 122.1 keV). Generally, the presence of coincidence events with $m>2$ is increased for energies (^{241}Am and ^{57}Co sources) greater than the K-shell absorption energy of the CZT material, due to the fluorescence X-ray events.

The analysis of multiplicity was also performed on a sub-pixel level with collimated synchrotron X-ray beams. The multiplicity of the coincidence events between two adjacent pixels at different beam positions was investigated. In particular, microscale line scans between the centres of the adjacent pixels were performed, with collimated (10 x 10 μm^2) synchrotron X-ray beams at energies below (25 keV) and above (40 keV) the K-shell absorption energy of CZT material.

During the line scanning between the two pixels, the data from all nine pixels of the investigated array were acquired, at each beam position (position steps of 25 μm). Figures 2.23 and 3.24 shows an overview of the multiplicity *m* vs. the beam position for two different line scans.

The line scanning near the central region of both pixels (Figure 2.23) highlights the presence of coincidence events mainly near the inter-pixel gap, with a spatial extension beyond the gap (50 μm) at 40 keV, due to fluorescence events; double coincidence events (m= 2) represent the dominant contribute to the overall coincidence events.

Near the edge region of the pixels (Figure 2.24), double coincidence events are present over all pixel area; the number of multiple coincidence events (m > 2) is strongly increased near the inter-pixel gap, due both charge sharing and fluorescence cross talk.

The predominant contribute to the overall coincidence events is represented by the events with multiplicity $m= 2$, as clearly shown in Figure 2.22. Tiple and quadruple coincidence events ($m > 2$) are mainly due to charge shared events near the inter-pixel gap, fluorescent cross talk and mixed shared/fluorescent events.

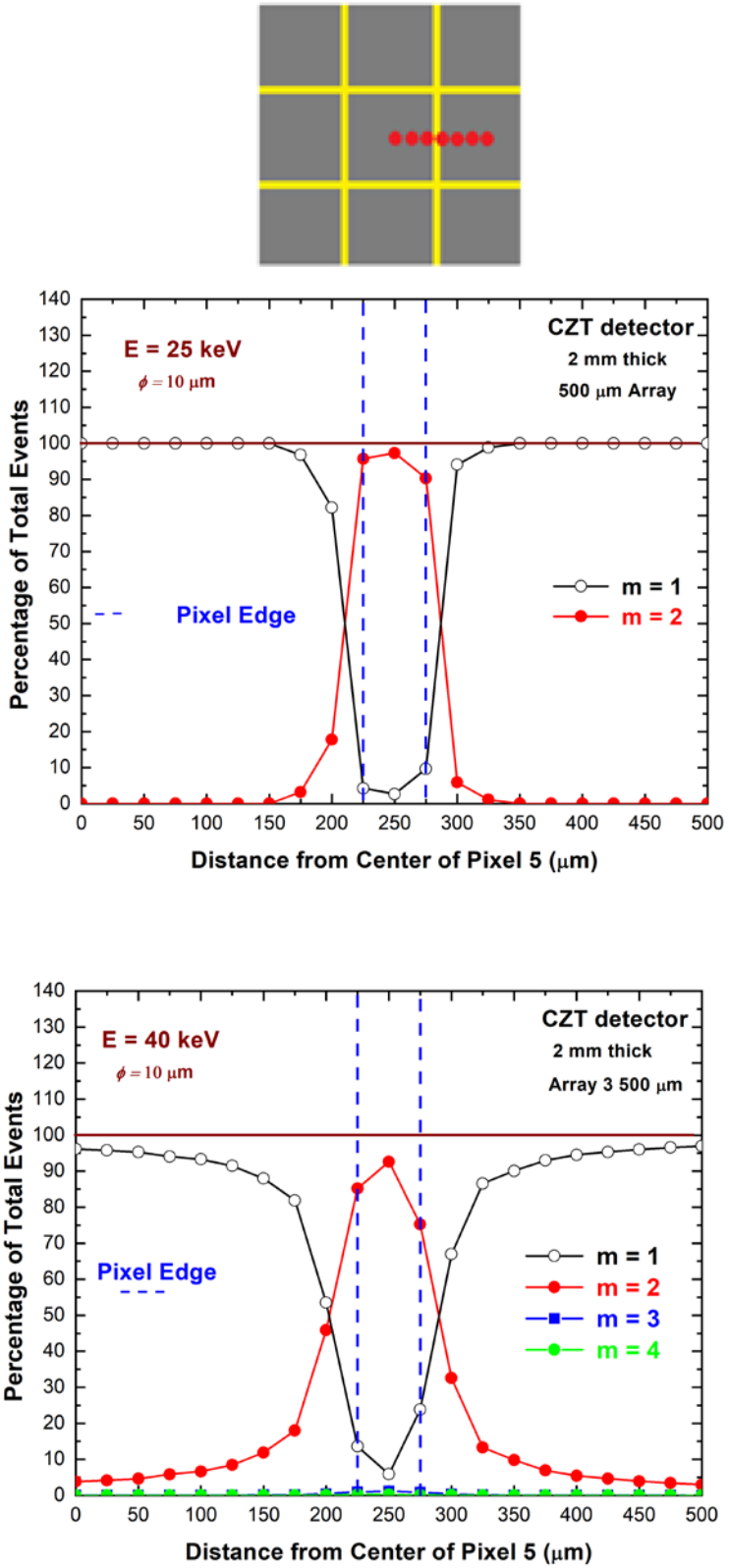

Figure 2.23 *Results of microscale line scanning with synchrotron X rays between the centres of two adjacent pixels at energy below (25 keV) and above (40 keV) the K-shell absorption energy of CZT material. The multiplicity m at various beam positions was measured*

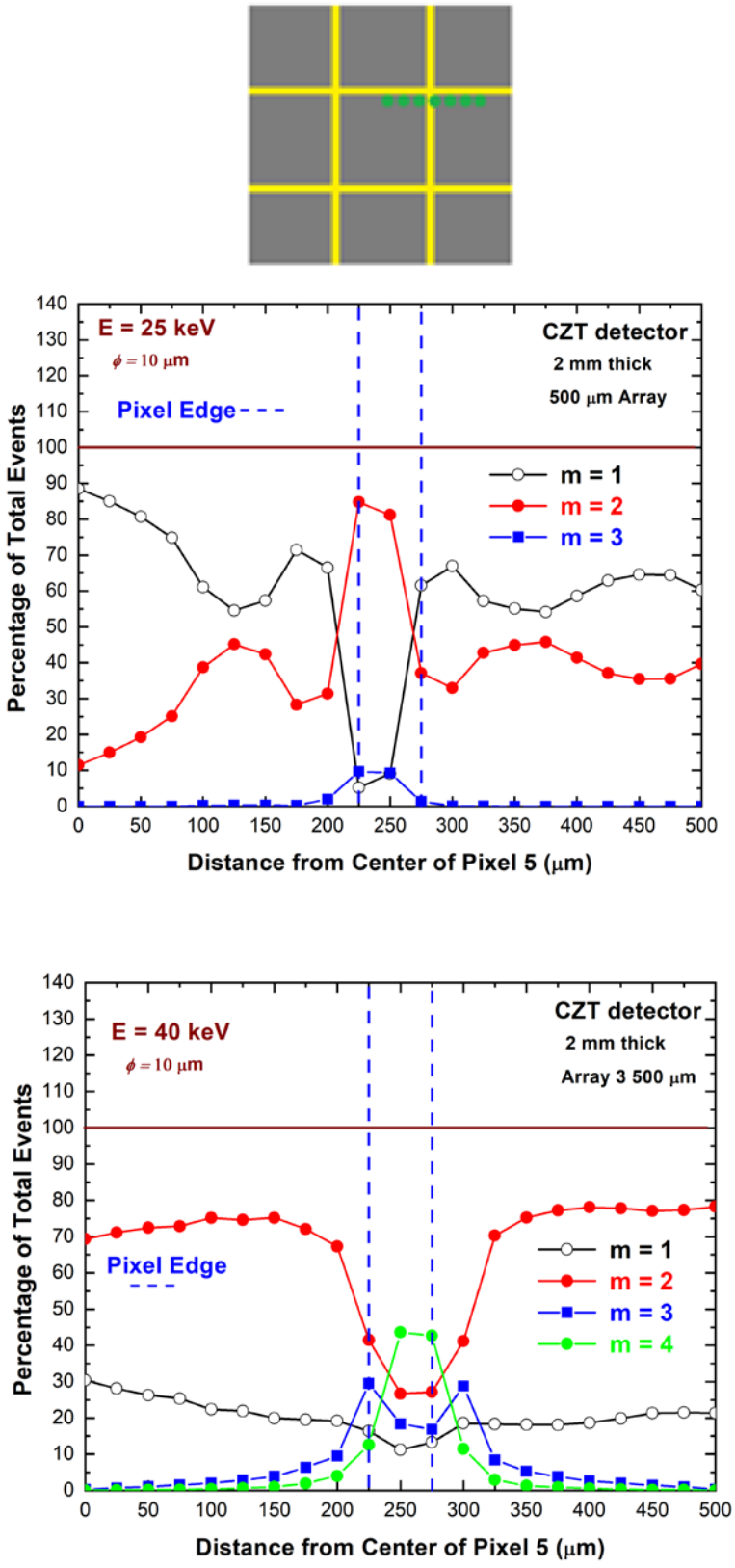

Figure 2.24 *Results of microscale line scanning with synchrotron X rays between the centres of two adjacent pixels near the gap region at energy below (25 keV) and above (40 keV) the K-shell absorption energy of CZT material. The multiplicity m at various beam positions was measured*

To better highlight the different effects of the two main contributes, the double coincidence of two adjacent pixels for a collimated irradiation (10x10 μm^2) was analysed with synchrotron X rays at the centre of one of the two pixels (Figure 2.25), in wich the energy spectra of the central pixel (Figure 2.25 (a)) and the adjacent pixel (Figure 2.25 (b)) are shown.

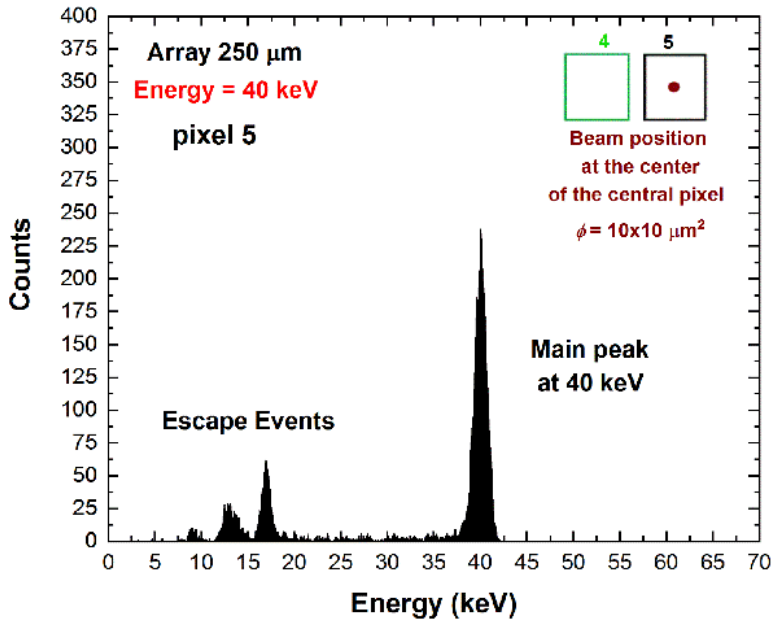

(a)

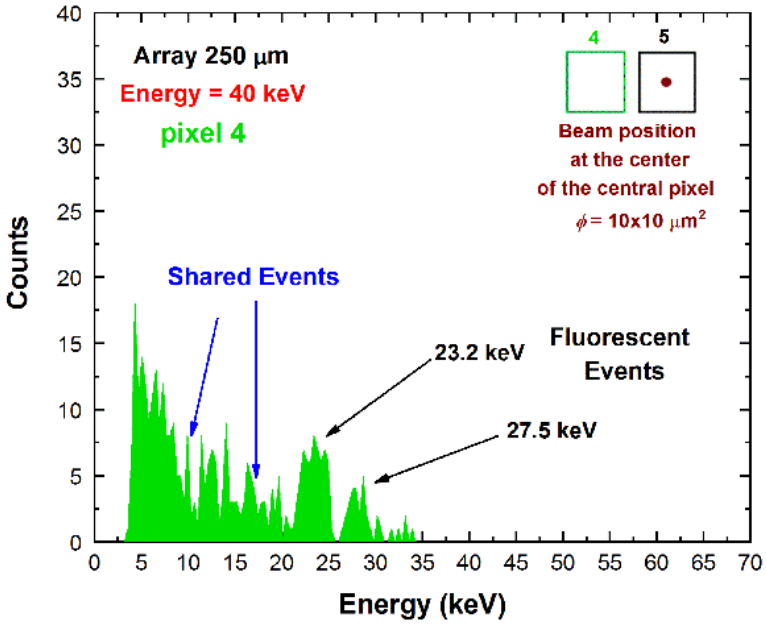

(b)

Figure 2.25 *Energy spectra at 40 keV of two adjacent pixels with a collimated X-ray synchrotron beam (10x10 μm^2) interacting at the centre of the central pixel (black pixel no.5). All events of the adjacent pixel (green pixel no. 4) are in temporal coincidence with the central pixel with multiplicity m=2. The presence of charge sharing and fluorescence cross talk events is clearly visible.*

All events of the adjacent pixel (green pixel no. 4) are in double temporal coincidence with events of the central pixel (black pixel no. 5).

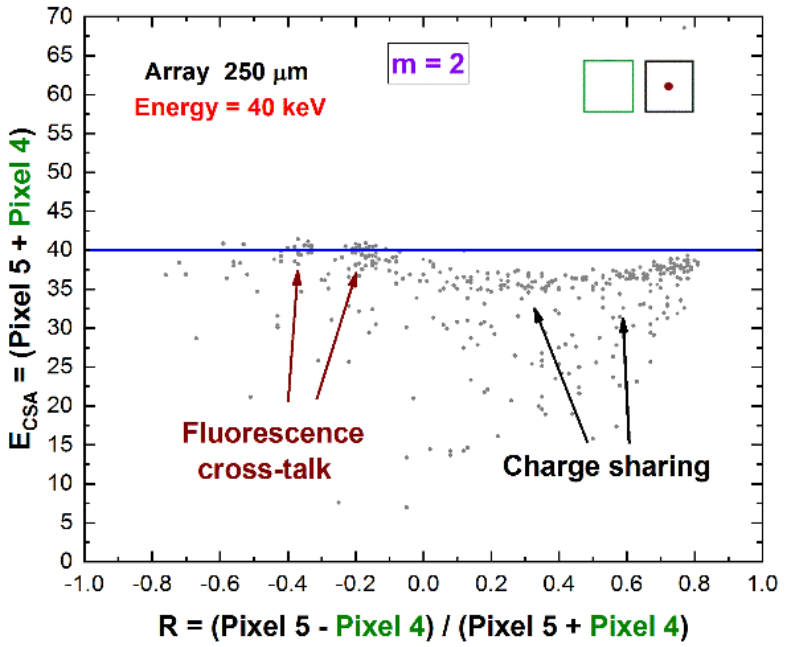

(a)

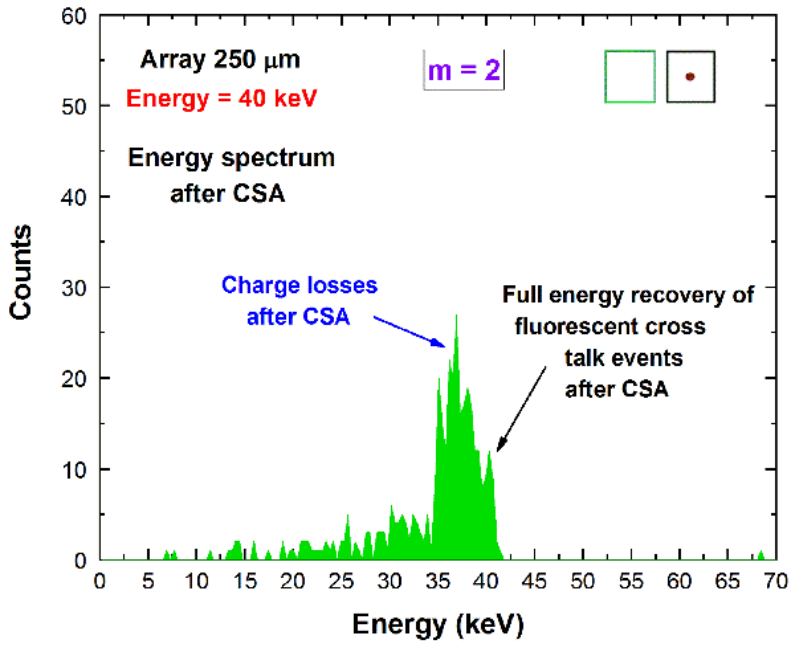

(b)

Figure 2.26 *Experimental results after CSA for m = 2 coincidence events between adjacent pixels. (a) The 2D scatter plot of the energy E_{CSA} after CSA versus the charge-sharing ratio R. (b) The energy spectrum after CSA.*

The shared events and fluorescent events are clearly visible in figure 2.25, and the results after charge sharing addition (CSA) are presented in figure 2.26.

The R parameter gives information about the interaction position of the shared events, it is the ratio between the energy of the pixel events: (pixel 5 – pixel4)/(pixel 5 + pixel 4).

The effects of charge sharing and fluorescent cross talk events after CSA are well distinguished. The energy of fluorescent cross events is fully recovered after CSA, as shown by the energy peak and the two kinks at R = -0.160 and R = -0.375 related to the 23.2 keV and 27.5 keV fluorescent X rays respectively; while charge losses characterized the double shared events after CSA, highlighted by a reduction of the centroid of the main peak.

2.6.5 Charge sharing correction

Coincidence events with multiplicity m=2

To recover the energy of double coincidences, two separate procedures for adjacent and diagonal pixels were proposed. The double coincidence events between adjacent pixels are mainly dominated by charge shared events and by a small contribute of fluorescent cross talk events. The energy of double shared events can be recovered through the correction technique, termed double charge sharing correction (CSC) (*Abbene et al., 2018b*). It consists of the modelling of the 2D distribution of the energy after CSA (E_{CSA}) vs. the charge-sharing ratio R with a parabolic function, (as shown in Figure 2.27 (a) for uncollimated ^{109}Cd source):

$$E_{CSA}(R) = E - \Delta E_{CSA}(0)(1 - R^2) \quad (2.3)$$

where E is the true photon energy and $\Delta E_{CSA}(0) = E - E_{CSA}(0)$ is the energy lost at the centre of the inter-pixel gap (R = 0).

The energy E_{CSA} is the centroid of the main photopeak of spectra obtained after CSA. Moreover, it is interesting to note the linear behaviour of the energy lost $\Delta E_{CSA}(0)$ with the true energy E, as shown in Figure. 2.27 (b):

$$\Delta E_{CSA}(0) = k_1 + k_2 \cdot E \quad (2.4)$$

Combining eqations 2.3 and 2.4, one obtains the following energy correction:

$$E_{corr} = (E) = \left[\frac{E_{CSA}(R) + k_1(1 - R^2)}{1 - k_2(1 - R^2)}\right] \quad (2.5)$$

This correction does not depend on the photon energy but it is related to the physical and geometrical characteristics of the inter-pixel gap, in particular the ratio between the gap area and the pixel area (*Abbene et al., 2018b*).

This technique allows the energy reconstruction of double shared events from uncollimated and poly-energetic sources (*Abbene et al., 2018b*). Figure 2.28 presents the results after the application of standard CSA and double CSC.

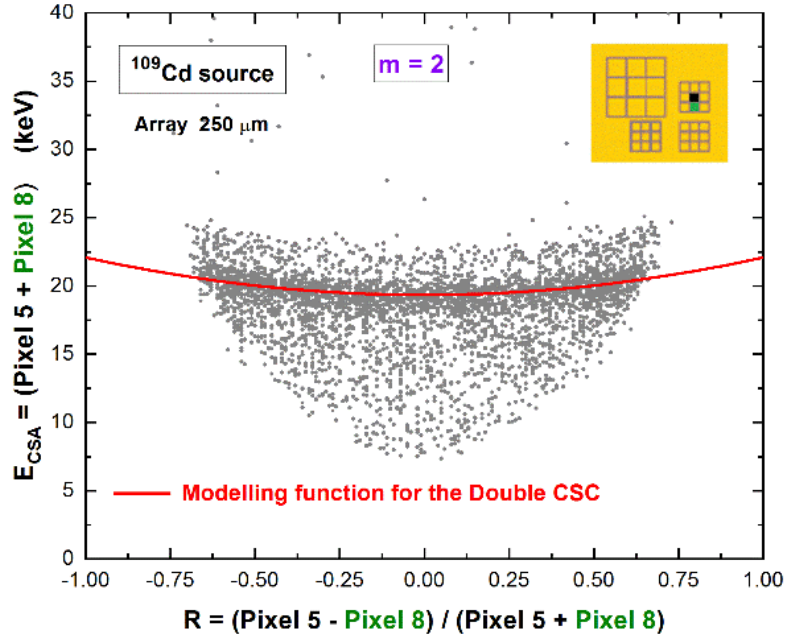

(a)

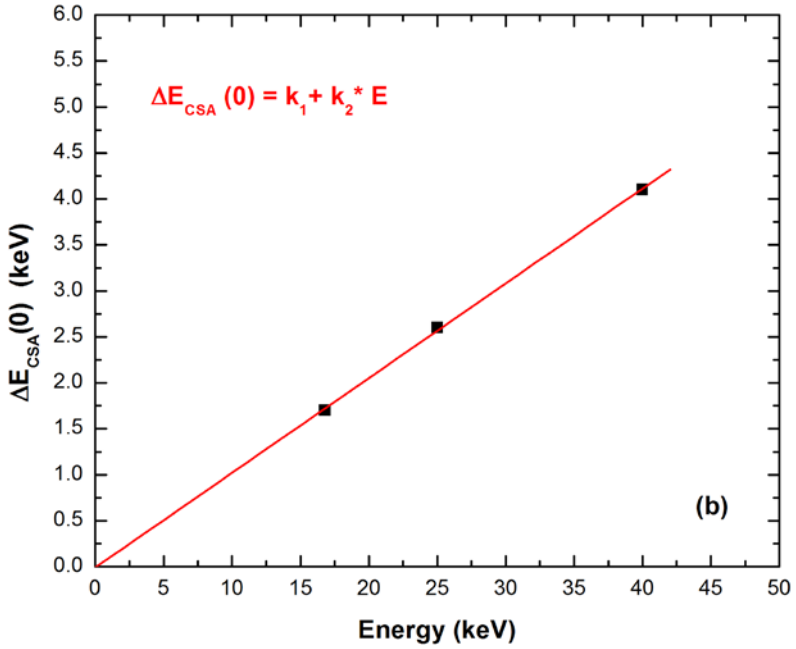

(b)

Figure 2.27 a)*2D scatter plot of the summed energy of the coincidence events (m= 2) between the pixel no. 5 and pixel no. 8, after CSA, versus the ratio R (uncollimated ^{109}Cd source). The red line is the modelling function used to correct charge losses (eq 2.3).* ***(b)*** *The linear behaviour of the charge loss ΔE_{CSA} (0) with the true photon energy E.*

After double CSC, the energy loss is recovered and the energy resolution is also improved.

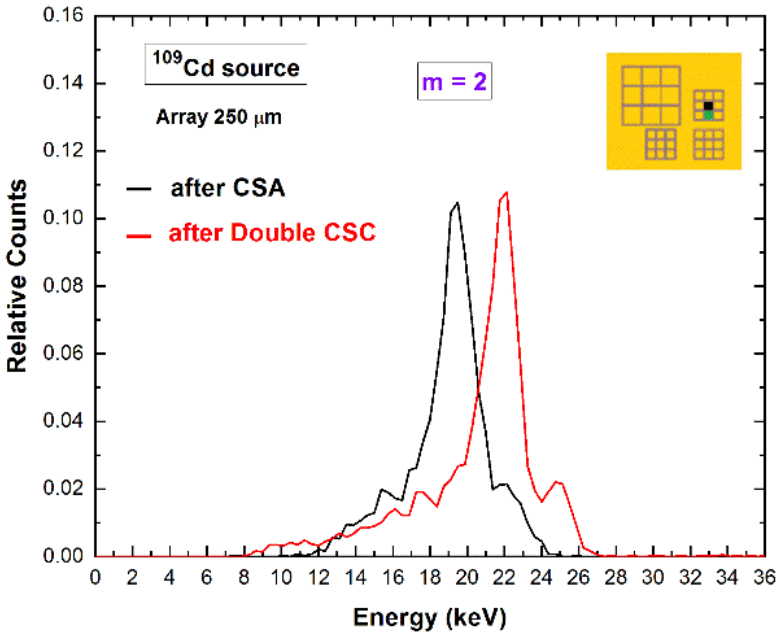

Figure 2.28 *The energy spectra after CSA (black line) and after double CSC (red line). The complete recovery of the energy after double CSC and improvements of the energy resolution are clearly visible.*

At energies greater than the K-shell absorption energy of the CZT material, the double coincidence events between adjacent pixels also contain fluorescent cross talk events, which can be easily corrected after standard CSA (Figure 2.26). The selection of these events (fluorescent event and escape peak event) is simple for mono-energetic X-ray sources, but it is challenge for poly-energetic sources.

Concerning the double coincidence events between diagonal pixels, it is observed that they are due to pure fluorescent cross talk events. This is clearly shown in Figure 2.29. In particular, the 2D scatter plot of Figure 2.29(a) highlights the energy recovery of the energy after standard CSA at about $R = \pm 0.22$ and $R = \pm 0.076$, which are related to the fluorescent X rays of 23.2 and 27.5 keV, respectively (^{241}Am source). The same result is also confirmed through the energy spectrum after CSA (Figure 2.29(b)). At energies below the K-shell absorption energy of CZT (e.g., by using ^{109}Cd source), no double coincidence events were observed between diagonal pixels.

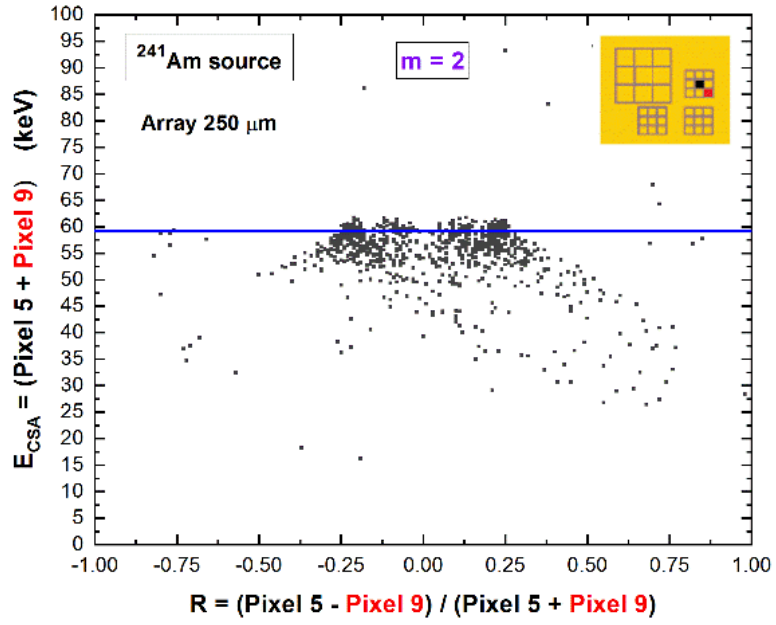

(a)

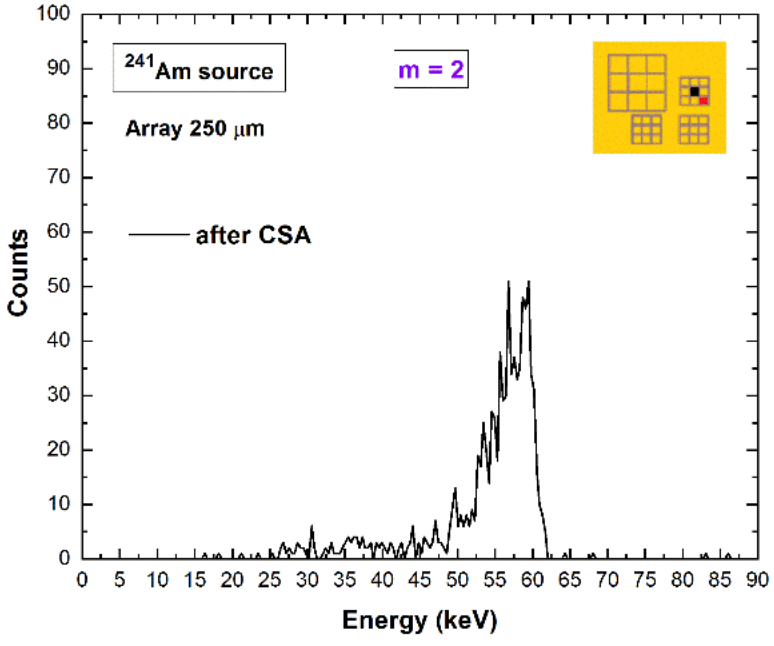

(b)

Figure 2.29 . (a) *2D scatter plot of the summed energy of the coincidence events (m= 2) between diagonal pixels (no. 5 and pixel no. 9), after CSA, versus the ratio R.* ***(b)*** *The energy spectrum shows the absence of charge losses after CSA, demonstrating as the double coincidence events between diagonal pixels are mainly due to the fluorescent/escape events.*

Coincidence events with multiplicity m>2

The results of Figure 2.22 point out the presence of coincidence events with multiplicity m>2, especially for the 250 μm array. These events are created by mixed fluorescent/shared coincidence events at the inter-pixel gap. In particular, some triple coincidence events (i.e., m = 3) can be often obtained from a true quadruple coincidence, where the energy of the pulse of one pixel is below the detection energy threshold, e.g. of 4 keV in this case. The recovery of the energy of multiple coincidence events is still challenging. In Figures 2.30-2.32, are shown the energy spectra of coincidence events after CSA at different multiplicity and energy.

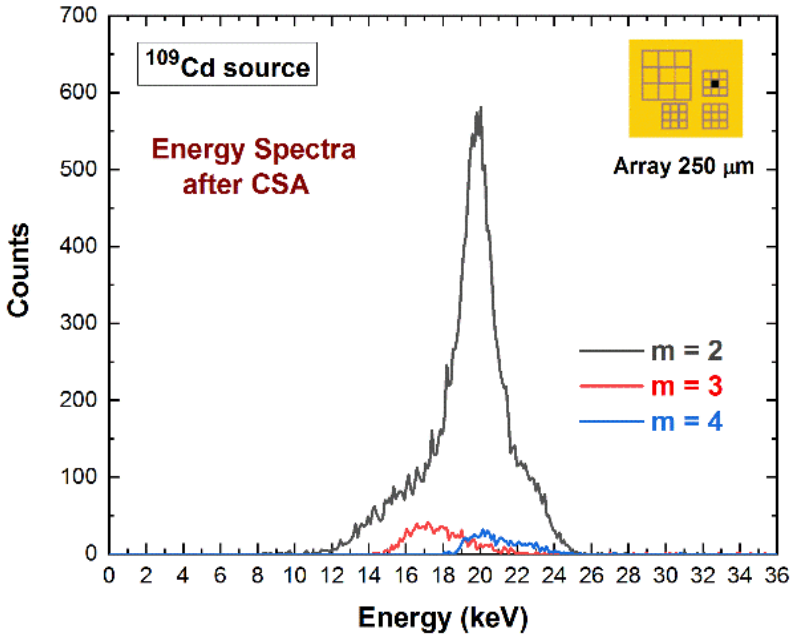

Figure 2.30 *^{109}Cd spectra after CSA at various multiplicities.*

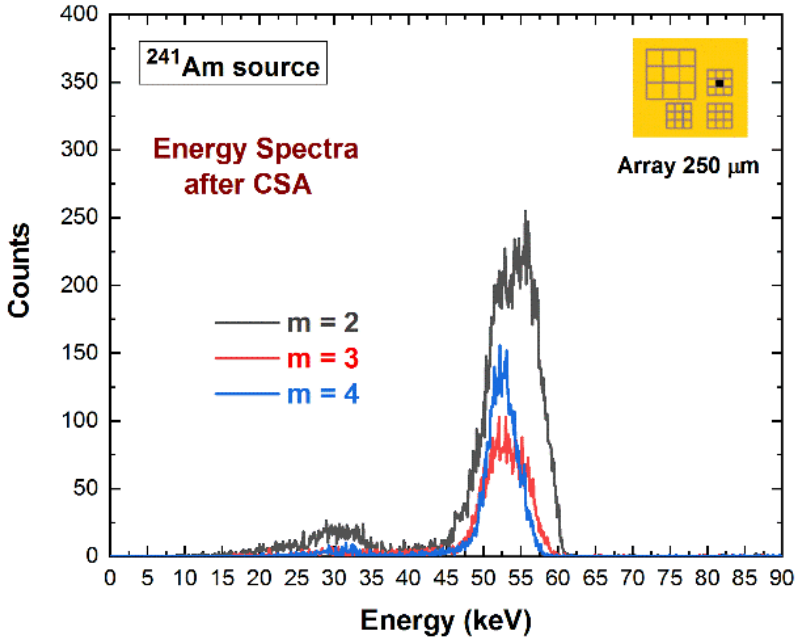

Figure 2.31 *^{241}Am spectra after CSA at various multiplicities.*

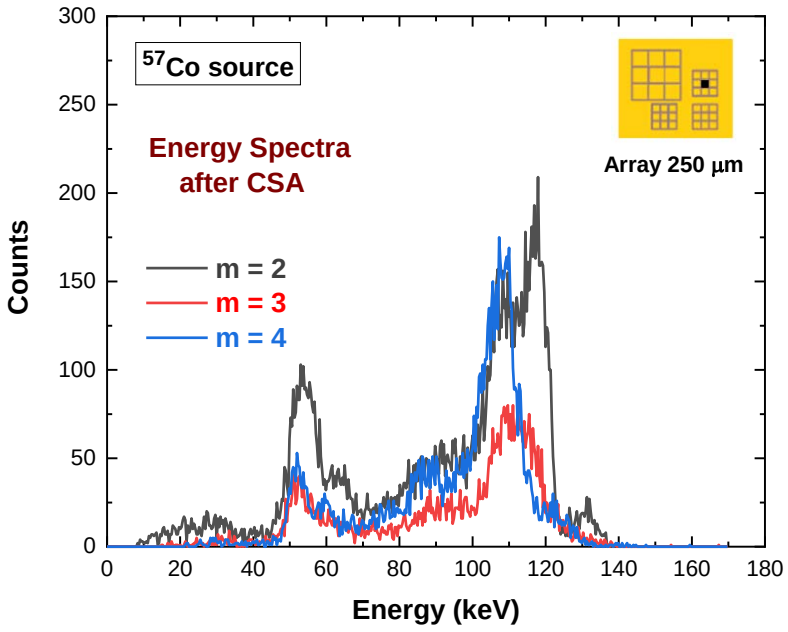

Figure 2.32 *^{57}Co spectra after CSA at various multiplicities.*

All energy spectra suffer from charge losses after CSA. However, the linear behavior of the summed energy E_{CSA} with the true photon energy (Figure 2.33) allows the recovery of the energy through a simple energy re-calibration procedure.

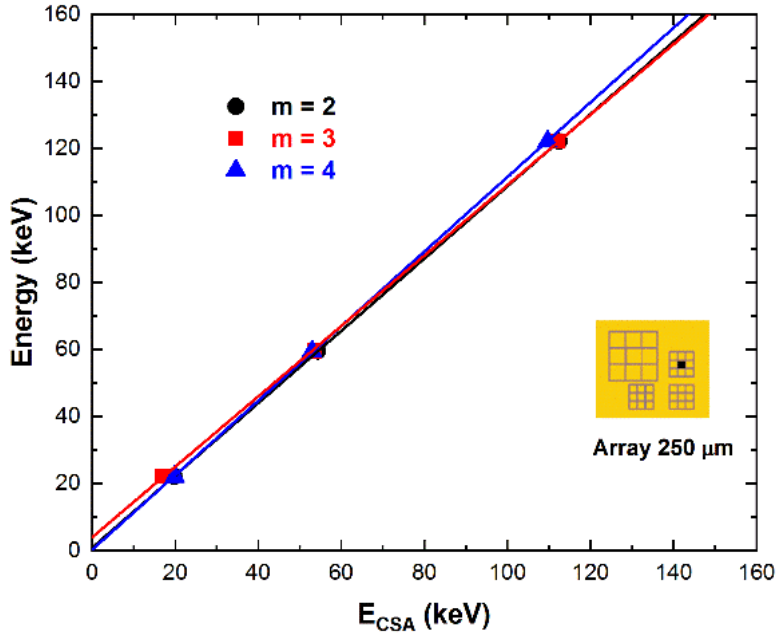

Figure 2.33 *The linearity of E_{CSA} with the true photon energy opens up to a correction of charge losses after CSA, through a simple energy re-calibration.*

The 4 keV intercept of the linear function for *m*= 3 (the red line of Figure 2.33) highlights the possible measurement of triple coincidence events from true quadruple coincidences, where the energy of one of the four pixels is below the detection threshold (4 keV) and therefore, not detected.

Finally, the various proposed correction techniques for each related multiplicity were applied: the *double CSC* technique on *m*=2 events between adjacent pixels, the *standard CSA* for *m*=2 events between diagonal pixels and the *re-calibrated CSA* for both *m*=3 and *m*=4 events. The complete correction is termed *multiple CSC* technique. The results for detectors B and C are shown in Figure 2.34.

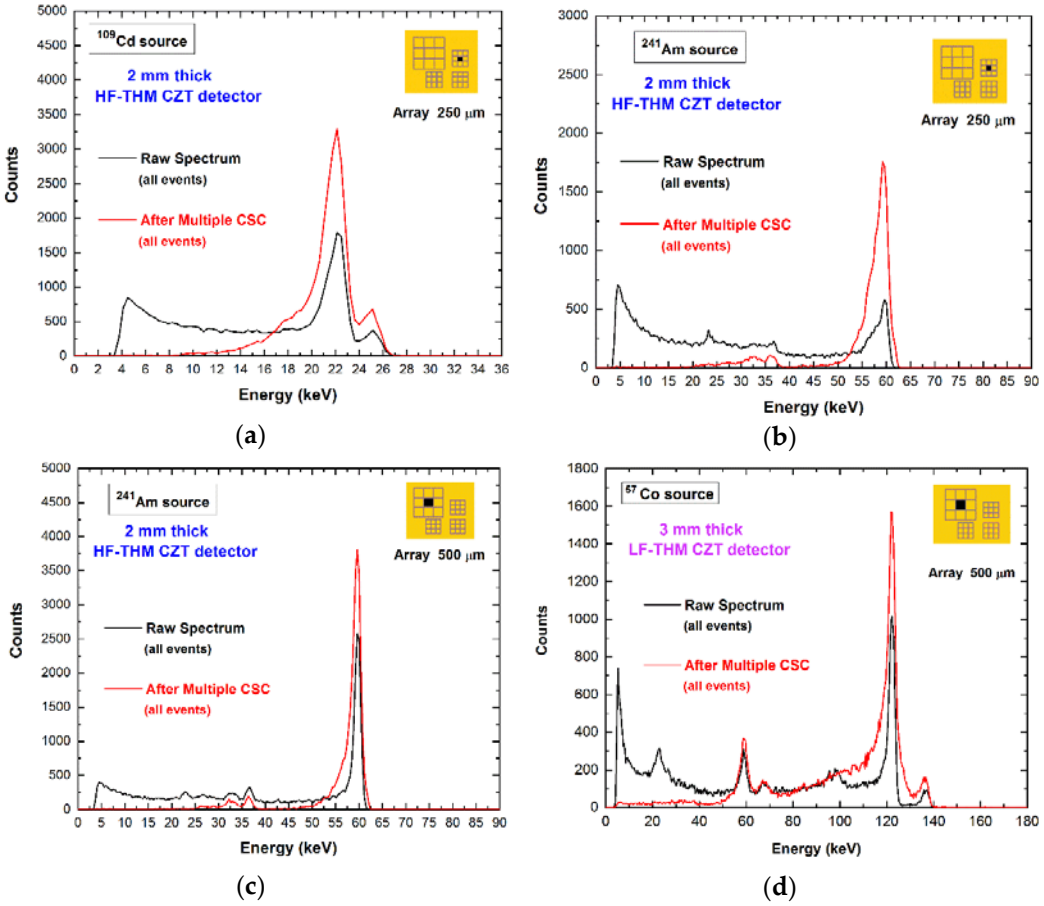

Figure 2.34 *The raw energy spectra (black lines) and the corrected spectra (red lines) after the multiple charge sharing correction (CSC) of the central pixel of 500/250 µm arrays and at different energies for B and C detectors. I applied the double CSC technique on m=2 events between adjacent pixels, the standard CSA for m=2 events between diagonal pixels and the re-calibrated CSA for both m=3 and m=4 events. The energy resolution was slightly improved.*

2.6.6 High flux measurements

To investigate the presence of high-flux radiation polarization effects in the detectors (*Abbene et al., 2016; Bale & Szeles, 2008*), the spectroscopic response of the detectors was also measured at high-rate conditions. As shown in par 1.4, high fluxes produce a charge build-up within the detectors which collapses the electric field and produces strong distortions in charge collection. This effect is mainly attributed to the poor charge transport properties of the holes (hole mobility-lifetime product $\mu_h \tau_h < 10^{-5}$ $cm^2 \cdot V^{-1}$) and, therefore, a careful choice of both crystal and device properties (electrode contact, bias voltage, thickness) is necessary to mitigate these effects. High-rate measurements were performed on the analized detectors in different contest:

- Mo-target X-ray spectra (Figure 2.35) (main fluorescent lines at 17.5 and 19.6 keV) irradiating central pixel of the detector A (B-VB 1 mm);
- Synchrotron X-ray spectra at 40 keV (Figure 2.36) by irradiating a pixel area of 400 x 40 μm^2 for central pixel of the detector B (Low Flux-THM 3 mm);
- Synchrotron X-ray spectra at 25 keV (Figure 2.37) by irradiating a pixel area of 500 x 20 μm^2 for central pixel of the detector C (High Flux-THM 2 mm);

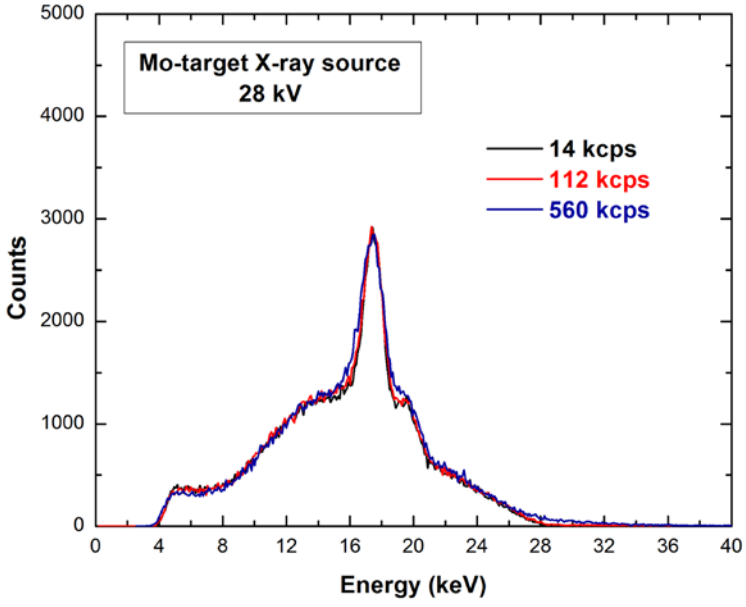

Figure 2.35 *Measured Mo-target X-ray spectra (central pixel of the large array) at different ICRs by detector A (B-VB 1 mm).*

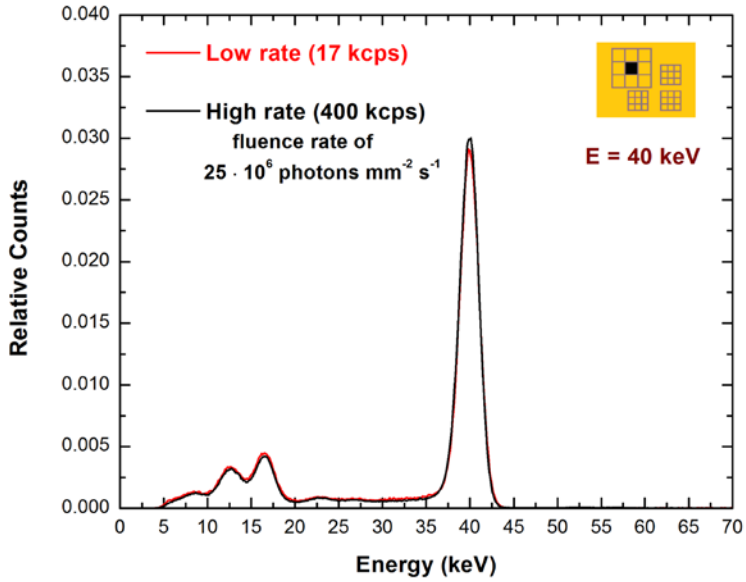

Figure 2.36 *Measured synchrotron X-ray spectra (40 keV) of the central pixel of the large array at different ICRs ICRs by detector B (LF-THM 3 mm).*

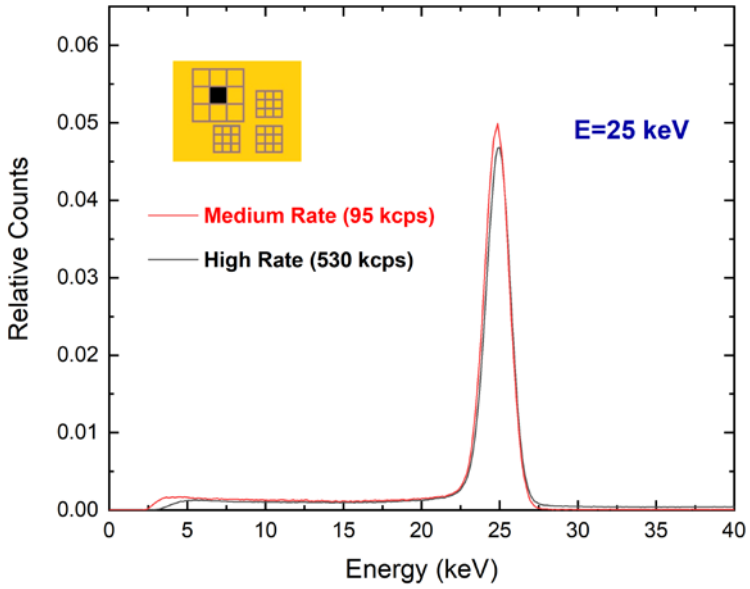

Figure 2.37 *Measured synchrotron X-ray spectra (25 keV) of the central pixel of the large array at different ICRs ICRs by detector C (HF-THM 2 mm).*

All the measured spectra show no energy shifts and low spectroscopic degradation under high flux conditions; this can mainly be attributed to the high-rate ability of the digital electronics, which minimize both the baseline shift and the peak pile-up effects in the spectra. However, no polarization effects were observed up to the investigated fluence rate conditions.

2.7. Conclusions

The performance of new CZT pixel detectors were presented. The tested CZT pixel detectors allow good spectroscopic performance and high bias voltage operation (>5000 $V \cdot cm^{-1}$) even at room temperature.

Good room temperature energy resolution was obtained, between 1 keV and 1.7 keV at 59.5 keV.

Charge-sharing measurements, with both uncollimated and collimated beams, highlighted high sharing percentages and the presence of charge losses near the interpixel gaps.

Original techniques able to perform the full recovery of the charge losses after charge sharing addition (CSA) in CZT pixel detectors were developed. Different approaches were used for adjacent and diagonal pixels, taking into account the number of involved pixels (i.e. the multiplicity m).

One approach, exploiting the relation between the summed energy after CSA and the charge-sharing ratio R of double coincidence events ($m = 2$), allowed the recovery of charge losses between adjacent pixels.

A second technique, based on the linear behavior of charge losses after CSA with the true photon energy, was also implemented to reconstruct multiple coincidence events with $m > 2$ (which are combinations of shared and fluorescent cross talk events).

The energy of double coincidence events between diagonal pixels, mainly due to fluorescent cross talk events, was successfully recovered after the standard CSA.

Results on different CZT pixel detectors, showed improved counting efficiency compared to using only isolated events (i.e. after CSD) and improved energy resolution compared to the standard CSA techniques.

The absence of high-flux radiation-induced polarization effects was also observed up to the investigated fluence rate conditions.

3. 3-D CZT DRIFT STRIP DETECTORS

3D CZT drift strip detectors for X and gamma ray spectroscopic imaging (10-1000 keV) were developed in the framework of the 3-CaTS (*High performance **3**D **Ca**dmium- Zinc-**T**elluride **S**pectro-imager for X and gamma -ray applications*), funded by the (Italian) National Institute for Nuclear Physics (INFN). The detectors are prototypes of a more complex 3-D imaging system for real-time dosimetric measurements during BNCT (Boron Neutron Capture Therapy) radiotherapy. The aim of this chapter is to present the spectroscopic abilities of this new detectors, with particular emphasis to the dedicated analysis of the different output pulses (*zoo of pulses*) for performance improvements. The potentialities of the detector for prompt gamma ray and neutron detection in BNCT will be also shown.

3.1. The 3-CaTS Project

The 3-CaTS project (*High performance **3**D **Ca**dmium- Zinc-**T**elluride **S**pectro-imager for X and gamma -ray applications*) (*Altieri et al**.**, 2018, Fatemi et al., 2018*), funded by the (Italian) National Institute of Nuclear Physics (INFN) aims to develop a 3-D spectroscopic imaging system capable to monitor the patient dose under the BNCT radiotherapy technique in realtime mode (*Moss R. L., 2014*). The project makes use of a multidisciplinary collaboration between the BNCT group of Pavia (INFN, Pavia), the research groups on detectors/electronics of Bologna (INAF, Bologna), of Parma (IMEM-CNR, Parma), of Palermo (DiFC, University of Palermo) and a company (due2lab, Reggio Emilia).

The BNCT technique is a localized therapy capable of selectively destroying cancer cells. It is part of the so-called binary therapies **^{10}B (n, α) ^{7}Li** since it is based on the synergistic action of two components which, individually, would have less effect in the treatment of neoplasms. These two components are the isotope stable of ^{10}B which is properly concentrated in cancer cells and a low energy neutron beam (thermal neutrons).

The BNCT exploits the neutron capture process that occurs by irradiating ^{10}B with a thermal neutron beam (energy E <0.5 eV). The idea to performs neutron capture therapy first came to G. L. Locher of the Franklin Institute of Pennsylvania in 1936, only four years after J. Chadwick's discovery of the existence of neutrons.

Locher's idea was the one that is still the basis of the BNCT today: to introduce what he called "neutron absorbers" (such as a soluble and non-toxic compound of boron, lithium, gadolinium or gold) in the area where you want generate ionization energy by bombarding with thermal neutrons.

^{10}B has a high neutron capture cross section (3838 barn at 0.025 eV) compared to the other elements that make up biological tissues.

The capture process leads to the production of an excited ^{11}B nucleus, which almost immediately decays into two particles: ^{7}Li and α particle (^{4}He nucleus). The process can take place in two different ways:

$$^{10}B + n_{th} \rightarrow {}^{11}B^{*} \rightarrow \begin{matrix} \alpha + {}^{7}Li \ \ (6\%) \\ \alpha + {}^{7}Li + \gamma\ [478\ keV] \ \ (94\%) \end{matrix} \qquad \textbf{(3.1)}$$

The reaction products have a LET (Linear Energy Transfer) of 150 keV·μm^{-1} for the α particles and 175 keV·μm^{-1} for the ^{7}Li nuclei. Thus, per unit of length, high-LET particles release a greater amount of energy than low-LET particles, however their penetration into the material will be small.

In fact, ^{7}Li path in biological tissue is about 5 μm while that of the α particles is about 9 μm, and since the cell size is about 12 μm, this allows to irreversibly damage the tumor cells causing apoptosis, preserving however healthy ones.

In reality, the actual destructive effect is due to the α particles; 7Li, despite being a high LET particle, has a shorter path inside the cell and can only rarely cause serious damage to the cell nucleus.

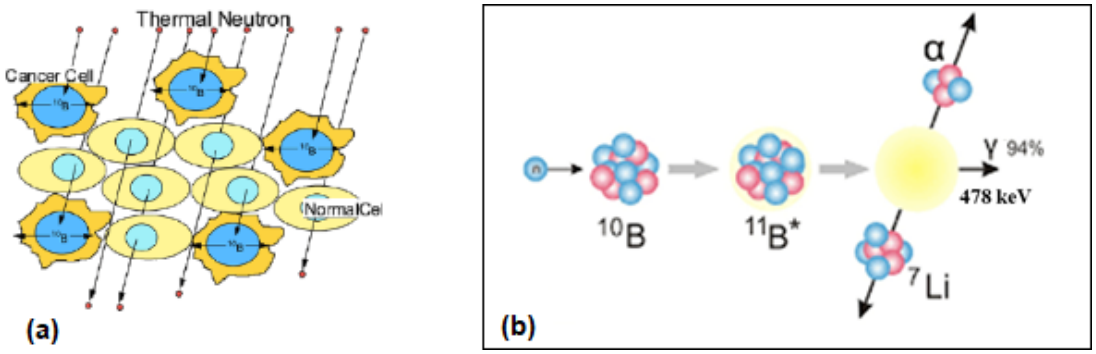

Figure 3.1 (a) *Thermal neutron bombing of carcerous tissues* ***(b)*** *capture process resulting in the creation of an excited ^{11}B nucleus, which almost immediately decays into two highly ionizing particles: ^{7}Li and α particles and emission of a gamma ray (in 94% of cases) with energy of 478 keV.*

A fundamental aspect of this treatment is the need for a much higher concentration of boron within the tumor cells than that present in non-diseased tissues. Among the many nuclides that have a significant cross section, the choice fell precisely on ^{10}B as this has a number of useful features:

i. it is a non-radioactive and readily available isotope;
ii. the particles emitted have a particularly high LET;
iii. the fission products are absorbed in an average radius of 5 - 9 μm, this value is lower than the average diameter of tumor cells;
iv. the chemistry of boron is quite well known and this allows to incorporate boron species in countless types of compounds.

Another important aspect in the application of BNCT, both for the effectiveness of the treatment plan and for the dosimetric aspects, is represented by the knowledge of the distribution (concentration) of boron in the cells during clinical treatment *(Kobayashi T. et al.,2000).* Currently, the estimation of these concentrations is carried out in off-line mode, i.e., before or after clinical treatment, through simulations and measurements with phantoms (*Kobayashi T. et al.*,2000; *Imahori, Y. et al.,1998).* The main limitation of these procedures is represented by the impossibility to perform estimation during the treatment (real time measurements) and carrying out personalized treatments. In clinical cases, the distribution of ^{10}B varies from patient to patient causing important fluctuations in the estimation of concentrations.

In this scenario, the aim of the 3CaTS project is to create a detector prototype capable of estimating the ^{10}B concentration in real time through the detection of 478 keV photons emitted in 94% of the capture reactions. It is planned to use SPECT (Single Photon Emission Computed Tomography) instrumentation based on CZT detectors with drift strip electrodes. The room temperature capabilities of CZT, the particular shape of the electrodes and digital analysis techniques will be exploited for a 3D reconstruction of key events (photons at 478 keV).

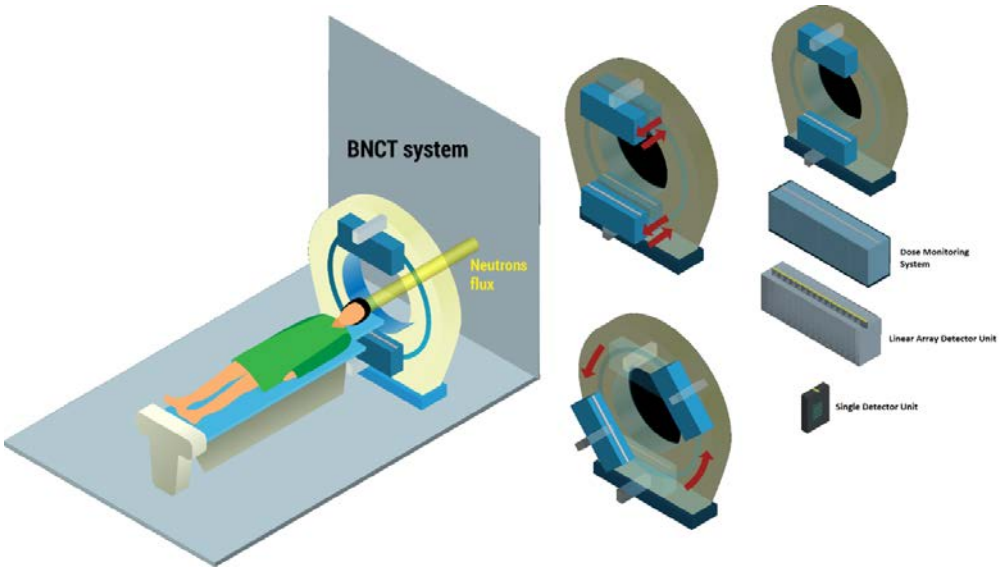

Figure 3.2 *Scheme of BNCT system (due2lab.com).*

3.2. 3-D Drift Strip Detectors

CZT detectors with a particular electrode geometry were developed. The drift strip electrode approach was implemented in order to optimize the collection of charges (electrons). Moreover, the presence of crossed strips allows the 3-D detection of photons. 2D positioning is made possible by the cross strips e on the anode and cathode of the detectors, while the third coordinate is determined through the analysis of the cathode/anode (C/A) pulses. The cross-strip configuration, if compared with the pixel one *(Zhang et al., 2012)*, allows a significant reduction of the channel number of the detection system: *n (anodes)+m* (cathodes) channels are required for 2D positioning, while *n·m* channels are needed by a pixel structure. The drift electrodes (or steering electrodes) were first introduced by Gatti and Rehak in 1983 for silicon detectors *(Gatti et al., 1984a, 1984b)*.

This approach, combined with the electron charge sensing electrode geometries of the detectors (pixels, strips, circular rings), was successfully used in CZT detectors with strong improvements in charge collection efficiency and energy resolution (*Abbene et al., 2007; Alruhaili et al., 2014; Lingren et al., 1998; Owens et al., 2007; Kalemci & Matteson, 2002; Kuvvetli & Budtz-Jorgensen, 2005; Van Pamelen et al., 1998*). Recently, new CZT drift strip detectors were realized at IMEM-CNR of Parma (Parma, Italy; http:// www.imem.cnr.it) in collaboration with due2lab (Reggio Emilia, Italy; http://www.due2lab.com). The detectors were fabricated from CZT crystals (19.4 x 19.4 x 6 mm^3) grown by the travelling heather method (THM) technique. More specifically, the prototypes were realized starting from Redlen CZT pixel detectors after electrode removal and surface treatments.

As well known (*Chen et al., 2008; Iniewski, 2014*), Redlen (http://redlen.ca) is able to produce spectroscopic grade CZT crystals with excellent charge transport properties (mobility-lifetime products of electrons $\mu_e\tau_e > 10^{-2}$ $cm^2 \cdot V^{-1}$).

In this project, used CZT materials are characterized by $\mu_e\tau_e$ ranging from $1x10^{-2}$ $cm^2 \cdot V^{-1}$ to 3×10^{-2} $cm^2 \cdot V^{-1}$. The anode layout is characterized by gold-strip electrodes with a pitch of 0.4 mm (0.15 mm strip width and 0.25 mm inter-strip gap) (left of figure. 3.3); however, the cathode side is divided into ten gold strips

orthogonal to the anode strips with a pitch of 2 mm (1.9 mm strip width and 0.1 mm inter-strip gap), as shown in figure. 3.3 (right).

Figure 3.3 *Anode (left) and the cathode (right) layouts of the CZT drift strip detectors. The anode strips (0.4 mm pitch; 0.25 mm gap) are orthogonal to the cathode strips (2 mm pitch; 0.1 mm gap). The anode strips are organized into collecting strips (1.6 mm pitch) and drift strips (0.4 mm pitch) which are negatively biased to optimize electron charge collection.*

The anode strips are organized into collecting strips (1.6 mm pitch) and groups of three drift strips between each collecting strip. The drift strips are negatively biased to optimize electron charge collection at the collecting strips. The key goal in CZT drift strip detector development is to allow the application of high bias voltages between the drift strips in order to optimize electron charge collection, maintaining the leakage currents (i.e. the electronic noise) to be as low as possible. To obtain this, great efforts were made in developing new detector processing techniques. The realization of a drift strip structure is generally a challenging procedure; first, it requires a double-patterning processing in segmenting both the cathode and the anode; second, the surface passivation is a critical operation in order to reduce the leakage currents.

Regarding 3-CaTS detectors, the CZT crystals were lapped with abrasive SiC paper, polished and extensively cleaned before starting the cleanroom process. The cathode strips are patterned by means of wet-chemical electroless gold deposition, standard photolithography and subsequent Br-based etching in ethylene glycol of

the gap between the strips. On the anode side, a dedicated surface passivation procedure was applied in three steps:

(i) deposition of negative photoresist with the anode pattern on the as-polished CZT surface;

(ii) strip deposition by means of the wet-chemical electroless technique from methanol solution, after a short Br-based etching for surface oxide removal;

(iii) reduction of surface leakage current between the anode stripes by using special surface passivation techniques with Al_2O_3.

This lithographic process for the anode side is challenging if one considers that Au electroless deposition is carried out in alcoholic solution (instead of typical water solution) after photolithographic patterning. Indeed, Au electroless deposition from methanol provides better mechanical adhesion than water-based deposition (*Benassi et al., 2017*), and patterning of the electrodes prior to Au deposition avoids a detrimental etching step, and the passivation with Al_2O_3 ensures lower leakage currents than the common wet passivation techniques (*Zanettini et al., 2018*). In this case, the detectors are characterized by very low-leakage currents between the drift strips (~1 nA at 50 V and twice this value at 100 V) (Figure 3.4) and uniformity among them.

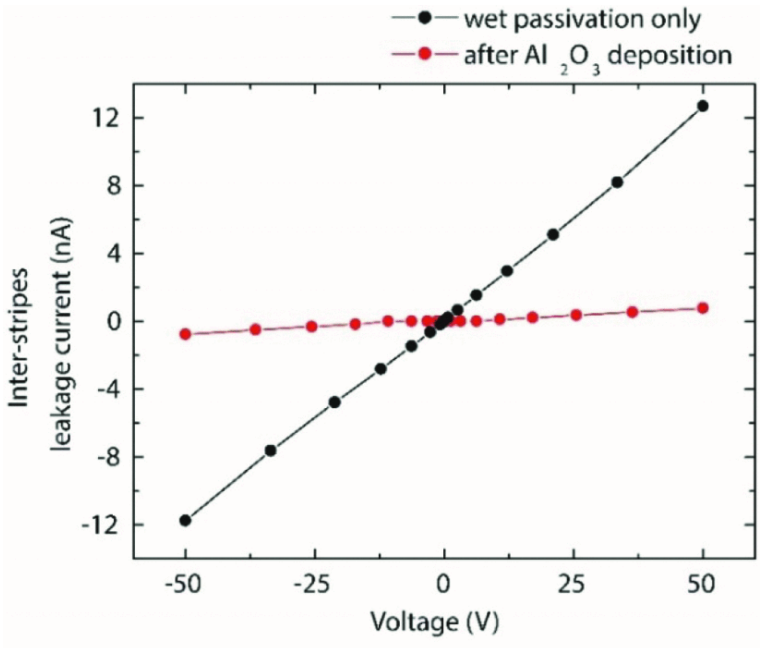

Figure 3.4 *Typical inter-strip leakage current I-V characteristics before (black) and after passivation (red).*

The sensor unit support and electrical interface board consist of five superimposed layers of different materials (Roger, Kapton and FR4) and are rolled together.

By means of a non-trivial bonding procedure, each metallic strip of the 3D CZT sensor is electrically connected with conductive glue to Au lines insulated by Kapton film.

With regards to the working mode, each detector is characterized by 12 drift cells; as shown in figure 3.5, each drift cell is defined by 15 strips: a collecting anode strip surrounded by two drift strips on the right side (RD), two on the left side (LD) and ten cathode strips. The two most external drift strips are actually shared between adjacent drift cells. The central drift strip of each group of three is more negatively biased than the two drift strips close to the collecting anodes. The dimensions of a single drift cell are 1.6 x 6 x 20 mm^3. The anode drift strips and the cathode strips are negatively biased to focus the electrons toward the collecting anode. Regarding the signal readout, the drift strips are connected in two groups of LD and RD drift strips. Each group contains three drift strips. Therefore, a drift cell is characterized by 13 readout channels. Overall, each detector drives 24 readout channels (12 collecting anode strips, 10 cathode strips and 2 drift anode strips).

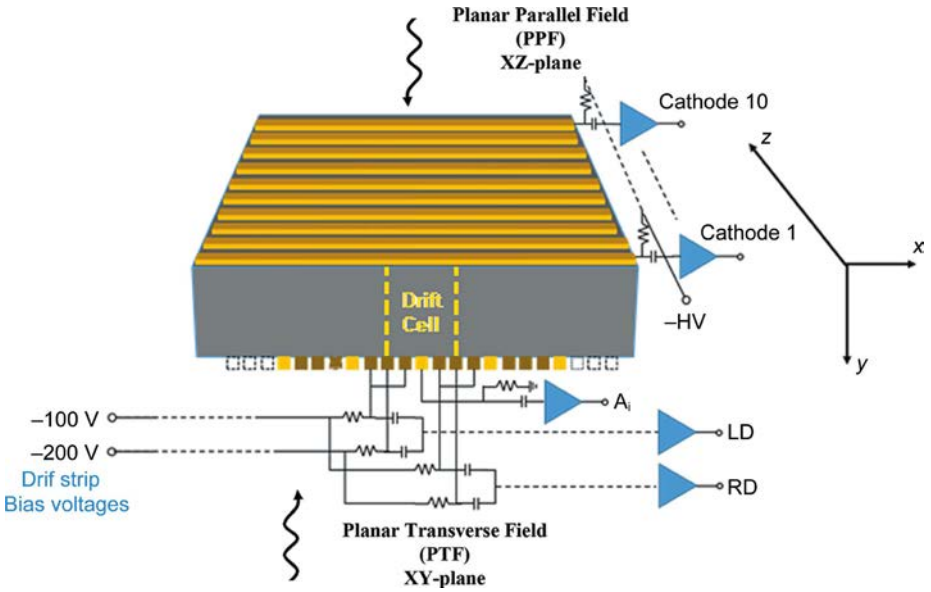

Figure 3.5 *Layout of a single drift cell of the 3D drift strip CZT detectors. Each drift cell (1.6 x 6 x 20 mm^3) contains a collecting anode strip and four drift strips, two RDs and two LDs of the collecting strip. The bias voltage values are optimized to collect electron charges on the collecting anode. The PTF and PPF irradiation geometries are also shown.*

3.3. Analog Front-end and Digital Electronics

The collecting anode strips, the drift strips and the cathode strips were a.c.-coupled to hybrid charge-sensitive preamplifiers (CSPs) and processed by 32-channel digital electronics. Both the CSPs and the digital electronics were developed at DiFC of the University of Palermo (Italy).

The CSPs are characterized by an equivalent noise charge (ENC) of 100 electrons and equipped with a resistive-feedback circuit with a decay time constant of 150 ms.

Like 2-D pixel detectors (Par. 2.4), the digital electronics consists of eight digitizers (DT5724, 16 bit, 100 $MS \cdot s^{-1}$, CAEN S.p.A., Italy; http://www.caen.it) driven by an original firmware (*Abbene et al., 2015, Abbene & Gerardi, 2015; Gerardi & Abbene, 2014*).

The data from each channel are transmitted through USB to PCs, where the user can control both the acquisition and the analysis. Due to the complex analysis required by the different pulse shapes, at this step, a mixed online/offline pulse processing was performed. For each CSP output channel, the digital system performs online pulse detection, time-tag triggering and provides to the PCs a sequence of selected pulses with the related arrival times ('*Snapshot Waveform*').

The Snapshot Waveforms are processed offline with dedicated analysis taking into account the different features of collected-charge pulses and induced-charge pulses. The height (i.e. the photon energy), the saturation levels (contribution induced by trapped charges) and the peaking time (i.e. the pulse shape) of the pulses are estimated offline after SDL and trapezoidal shaping.

3.4. Experimental Set-up

The detector and CSPs are placed into a metallic box (Figure 3.6) that provides shielding from electromagnetic interferences

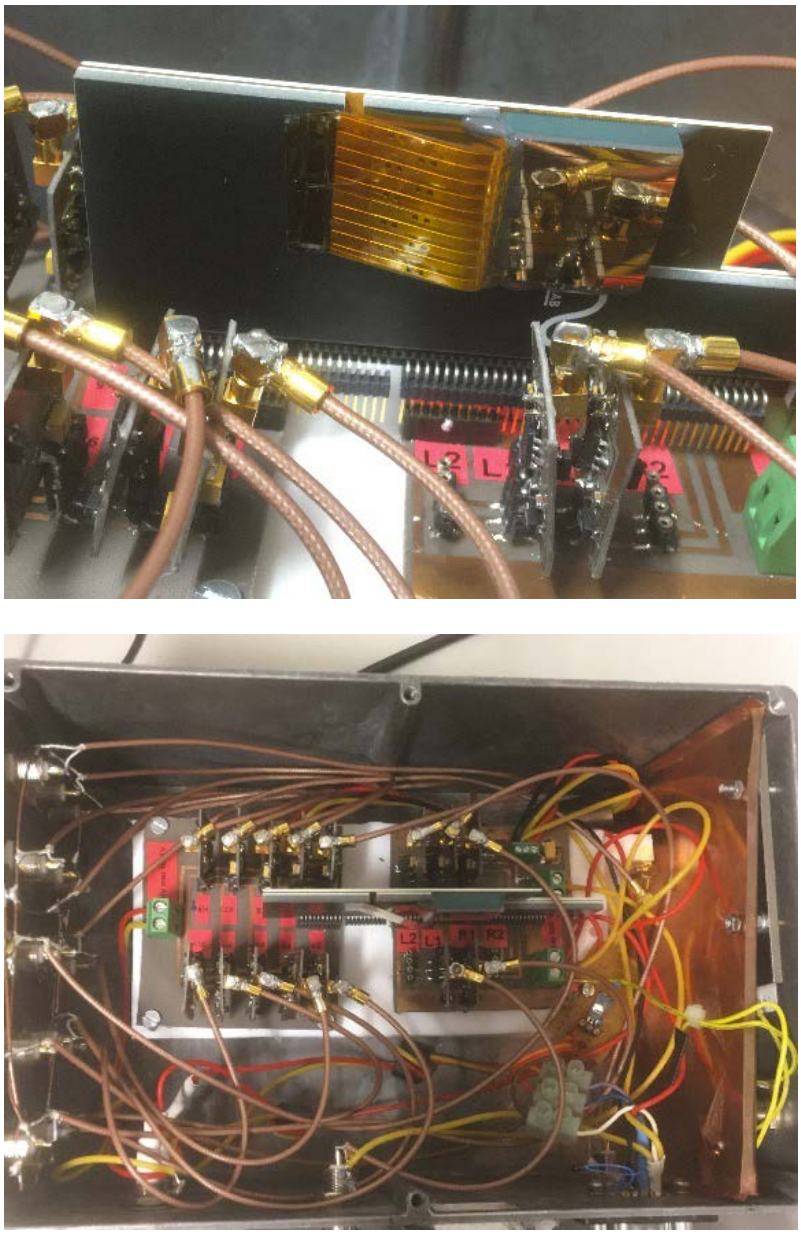

Figure 3.6 *Detector coupled to CSPs.*

The spectroscopic response of the detectors was investigated by X-ray and gamma-ray calibration sources (main gamma lines: ^{241}Am, 59.5 keV and 26.3 keV; ^{57}Co, 122.1 keV and 136.5 keV; ^{137}Cs: 661.7 keV).

The 3D working mode of the detectors foresees the PTF irradiation geometry (xy plane), exploiting the 20 mm thickness of the CZT material in the z direction. For comparison, the spectroscopic performance through the PPF geometry (zx plane) was also evaluated.

All measurements were performed at T = 20°C.

Anode strips are put at ground, cathodes and drift strips are polarized with negative voltages through a multichannel power supply able to provides 4 independent High Voltage channels. Each channel also features an independently selectable polarity.

Measurements with thermal neutron were performed at the TRIGA Mark II Reactor at L.E.N.A. of the University (Pavia, Italy).

Figure 3.7 *The TRIGA Mark II Reactor at L.E.N.A. of the University (Pavia, Italy).*

3.5. Measurements and Results

The structure of the strip electrodes and the effects of the physical processes that occur in the CZT detectors (photoelectric and Compton interaction, charge collection effects…) generates a real "*zoo*" of charge pulses with different characteristics and shapes. Thus, an overview of the various pulses generated in CZT drift strips detectors are presented at first, with the aim to better understanding, through simulations and experimental measurements, the nature of these pulses and their role in the detector performance. This is very important for a proper analysis setting, impulse processing and the development of new strategies for the improvement of the spectroscopic and spatial performances.

3.5.1 Pulse analysis

As previously introduced (Par 1.3), the pulses generation in CZT detectors can be explained through the Shockley-Ramo theorem, with the concept of weighting potential. In this case, the pulses that are formed in the detector if irradiated with 662 keV mono-energetic photons (^{137}Cs radioactive source) were measured. The nature of the interaction (photoelectric and Compton) creates single events and double events (Figures 3.8 and 3.9).

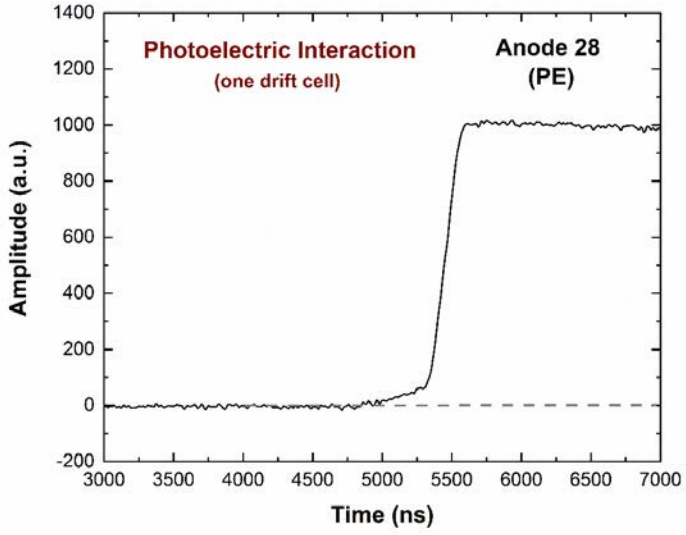

Figure 3.8 *Photoelectric single event measured by the collecting anode. The detector was irradiated with a ^{137}Cs source (662 keV).*

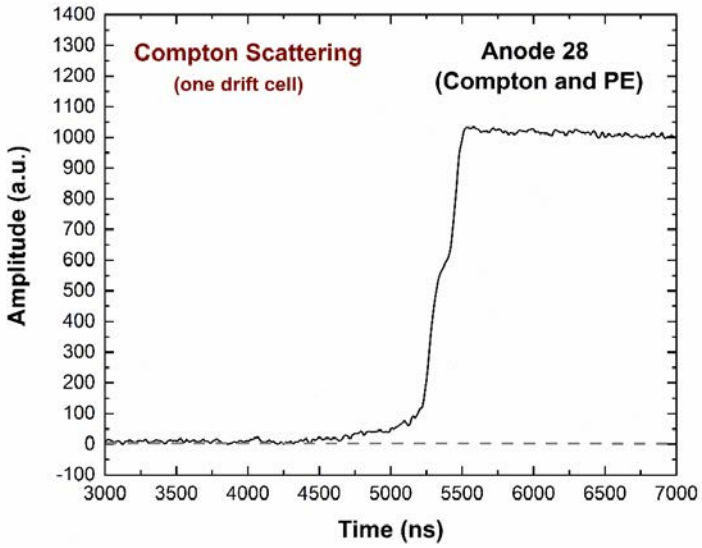

Figure 3.9 *Double event after Compton and photoelectric interaction. The detector was irradiated with a ^{137}Cs source (662 keV).*

In this work, the single pulses after photoelectric interaction were analyzed.

Due to the behavior of the weighting potential, pulses with different shapes are created, strongly related to the various positions and trajectories of the charge carriers.

Generally, the detector pulses can be classified into collected and induced charge pulses. The collected charge pulses (*collecting pulses*) are generated by the charge carriers really collected by an electrode (*collecting electrode*), while the *induced pulses* are generated by the *weighting potential cross talk effect* (Par. 1.4.4).

Moreover, due to the presence of the trapping of the charge carriers, induced pulses often saturate at a non-zero level and, moreover, the contributions of both induced and collected charges can also coexist in a single pulse (*Bolotnikov et al., 2014*).

In this way, a real variety of induced and collected charge impulses (*zoo of pulses*) is created:

- Collected pulses;
- Induced pulses with zero saturation level;
- Induced pulses with positive or negative saturation level.

The measured pulses (i.e., the output pulses from the charge sensitive preamps) are the result of purely photoelectric interactions of photons at 662keV.

The simulated pulses were obtained through a custom procedure organized in three main blocks:

a. radiation-semiconductor interaction with Monte Carlo methods (GEANT4) (*Agostinelli et al., 2003*);
b. calculation of the electric field and weighting potential by the finite element method (FEM) with COMSOL Multiphysics;
c. calculation of charge carrier transport and pulse formation in MATLAB environment (*Bettelli et al., 2020*).

The charge carrier transport properties in the simulation are typical of Redlen CZT materials for low-flux applications (LF-CZT materials): μ_e=1100 $cm^2V^{-1}s^{-1}$and τ_e=11 μs for electrons, and μ_h=88 $cm^2V^{-1}s^{-1}$ and τ_h=0.2 μs for holes (*Thomas et al., 2017*). Figure 3.10 shows a section of the detector with measured pulses by the anode, cathode and drift.

Figure 3.11 shows an overview of simulated and measured pulses from the anode, cathode and drift strips (electrode voltages: -350 V for the cathodes, -200 V for the central drift strips and -100 V for the adjacent drift strips). The photon interactions near the cathode (top) and the anode (bottom) are mainly focused (the black circular points represent the photon interaction positions). For each photon interaction, the measured pulses are detected in temporal coincidence. Both simulations and measurements produce similar results on the key features of the pulses.

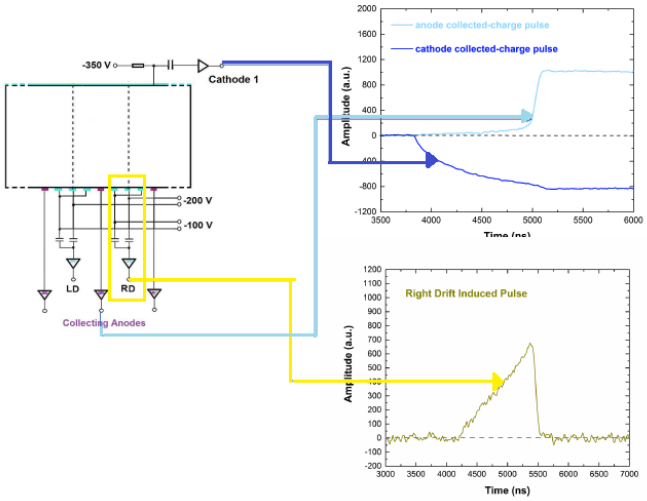

Figure 3.10 *Section of the detector with measured pulses by the anode, cathode and drift.*

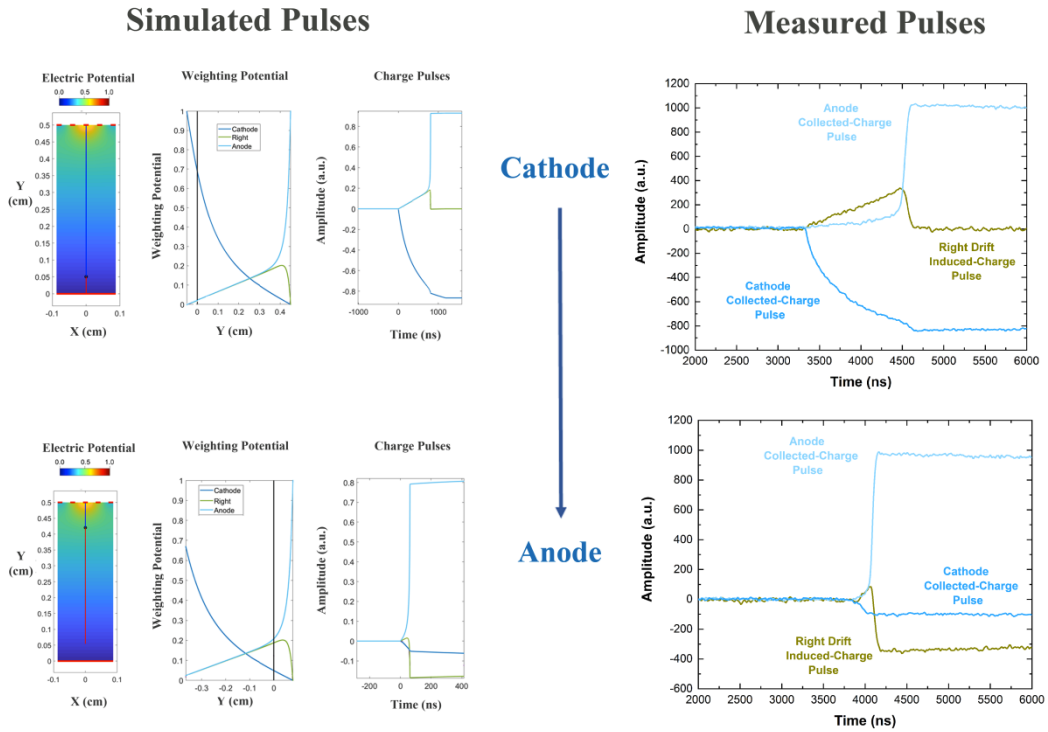

Figure 3.11 *Measured and simulated pulses from the anode, cathode and drift strips. Calculated electric and weighting potential profiles are also reported. Collected and induced-charge pulses are clearly visible, related to photon interaction near the cathode (top) and near the anode (bottom).*

Regarding ***collected charge pulses***, typically, these pulses, positive and negative, are created from anode and cathode strips, respectively. As shown in Figure 3.11, the weighting potential of the anodic strips shrunks near the anode, thus reducing the contribution of the holes in the charge pulses. However, as also observed in pixel detectors (*Abbene et al., 2018a; Barrett et al., 1995*), the contribution of the holes becomes more important for the interactions of photons near the anode. The shape of the anode collected charge pulses (positive light blue pulses of figure 3.10) strongly depends on the point of generation of the charge (photon interaction). For the interactions of photons near the cathode (upper side of figure 3.11), the anode pulses are characterized by a leading edge with slow and fast slopes, following the behavior of the weighting potential of the anode; while, near the anode (bottom side of figure 3.11), the leading edge is characterized only by a fast slope. In particular, initial slow leading edge represents a critical problem in estimating the arrival time of events. Due to a coarse strip segmentation, the weighting potential of the cathode strips spans between the cathode and anode electrodes, producing charge pulses

more sensitive to the hole contribution. Unlike to the anode pulses, the collected charge pulses from cathode strips have a well-defined slope of the leading edge (negative blue pulses of figure 3.10), which allows a better estimation of the arrival time. The peaking times of the pulses can reach maximum values of 2 μs and 3 μs for the anode and cathode, respectively. This indicates that a long shaping time constant of the shaper amplifier is required to avoid ballistic deficit distortions (*Knoll, 2000*).

Induced-charge pulses with zero saturation level (dark yellow pulses shown in the upper part of figure 3.11) are observed in drift strips. These pulses are mainly due to the interactions of photons near the cathode and are related to the drift of the electron charge: the electron charge, which moves towards the anode, also intercepts the non-monotonic weighting potential of the drift strips (yellow dark curve). The pulses rise as the electron charge moves to the collecting anode and then rapidly decrease to zero as the electrons are collected. Their amplitude (pulse height) can be used to estimate the photon interaction positions among the anode/drift strips (x-positioning) (*Howalt Owe et al., 2019; Budtz-Jørgensen & Kuvvetli, 2017*). These pulses are also observed in cathode strips and can be helpful to improve z-positioning among the cathodes, with spatial resolution better than the geometrical strip pitch (2 mm).

Induced-charge pulses with a negative saturation level are also characteristic of drift strips, particularly for photon interactions near the anode, as shown in the bottom side of figure 3.11. This negative saturation level is due to the charge induced by holes trapped in the detector (*Bolotnikov et al., 2014, 2016; Zhu et al., 2011*), as also confirmed by simulation.

Since the amplitude of this negative level is related to hole trapping, this information can be used to reduce the effects of incomplete charge collection in the collected-charge pulses of the anode strips, detected in temporal coincidence.

Drift strips also generate ***induced-charge pulses with positive saturation levels*** (Figure 3.12). These pulses, mainly related to photon interactions near the cathode, are due to the charge induced by electrons trapped in the detector.

In general, due to the moderate trapping of electrons, the number of these pulses is very low if compared with those due to hole trapping. When a ^{137}Cs photon is fully

absorbed near the cathode side of the CZT detector, the size (FWHM) of the electron cloud, after drifting through the entire thickness of the crystal, can be estimated to about 350 μm (*Bettelli et al., 2020; Bolotnikov et al., 2007*).

Figure 3.12 also shows three different cathode pulses due to the effects of charge sharing between cathode strips: the pulse from cathode 7 (brown pulse) is an example of mixed induced collection charge pulses, due to the effects of both charge sharing and weighting potential cross talk. Mixed induced-collected charge pulses generally have a strong presence in pixel detectors (*Bolotnikov et al., 2014, 2016*), representing a critical issue in the estimation of photon energies.

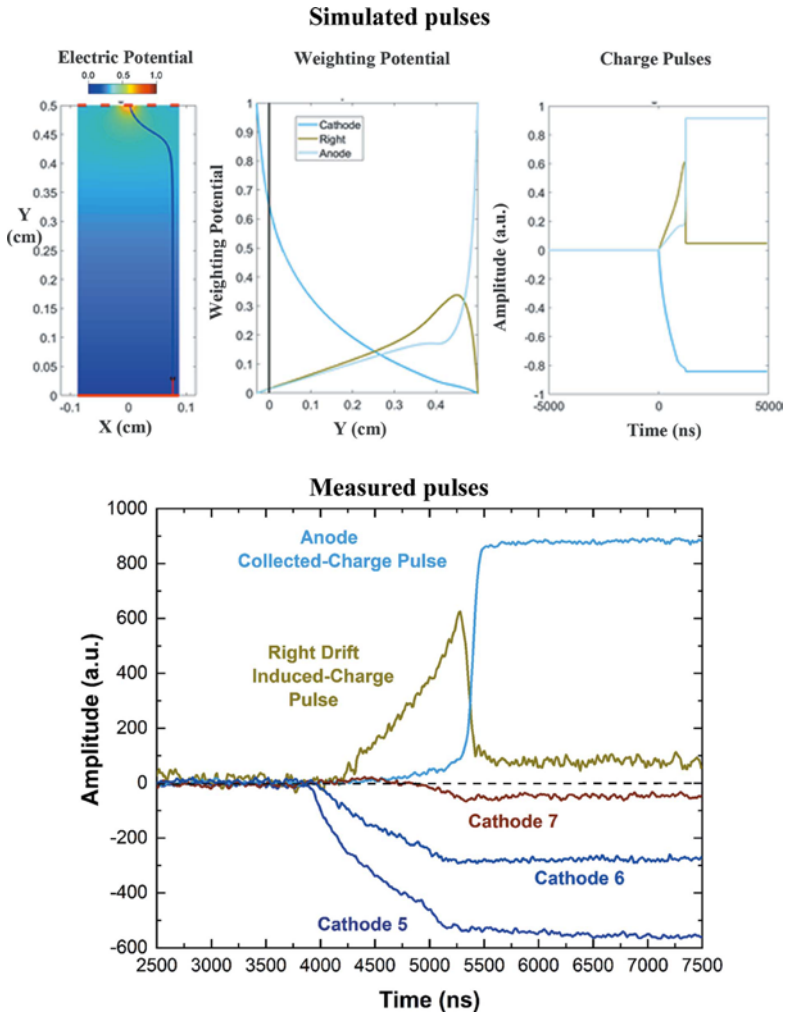

Figure 3.12 *Simulated and measured pulses from the anode, cathode and drift strips. Induced-charge pulses with positive saturation levels can be attributed to the electron trapping. Mixed induced-collected charge pulses (cathode 7) are also observed, due to both charge sharing and weighting potential cross talk.*

3.5.2 Energy resolution

After pulse analisys, spectroscopic characterization of detector was performed.

The first operation concerned the optimization of the voltages of the electrodes (cathodes and drift strips).

In figure 3.13 the measured 662 keV photopeaks of uncollimated ^{137}Cs spectra for a collecting anode strip at different cathode bias voltages are shown.

The drift strip bias voltages of -100 V for adjacent drift strips and -200 V for central drift strips represent the best compromise between charge collection improvements and leakage current increasing.

The results clearly highlight that the best energy resolution was obtained at low cathode voltage values (-350 V; 583 V·cm^{-1}). This is due to the particular electrode structure of the detector: once the drift strip voltages are fixed, higher cathode voltages worsen the electron charge collection on the collecting anode, although the photopeak shifting to higher energy there is a worsening of the energy resolution. Spectra with excellent energy resolution of 1.3% FWHM at 661.7 keV are obtained without any corrections for charge sharing or trapping (Figure 3.14).

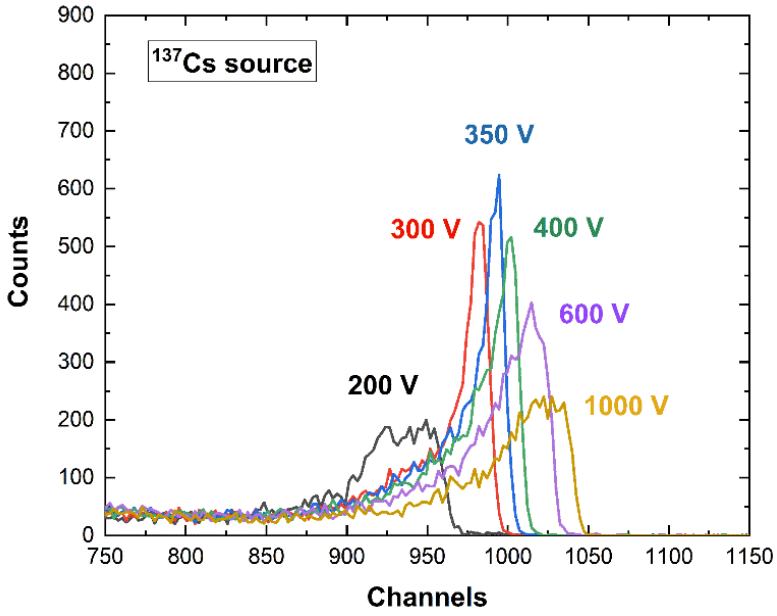

Figure 3.13 *662 keV photopeaks of the measured ^{137}Cs spectra from a collecting anode strip at different cathode bias voltages; fixed drift strip voltages (adjacent drift strips: -100 V; central drift strips: -200 V) are used. The detector, irradiated in PTF geometry, shows the best energy resolution (1.3% FHWM at 661.7 keV) at a cathode voltage of -350 V (583 V·cm^{-1}).*

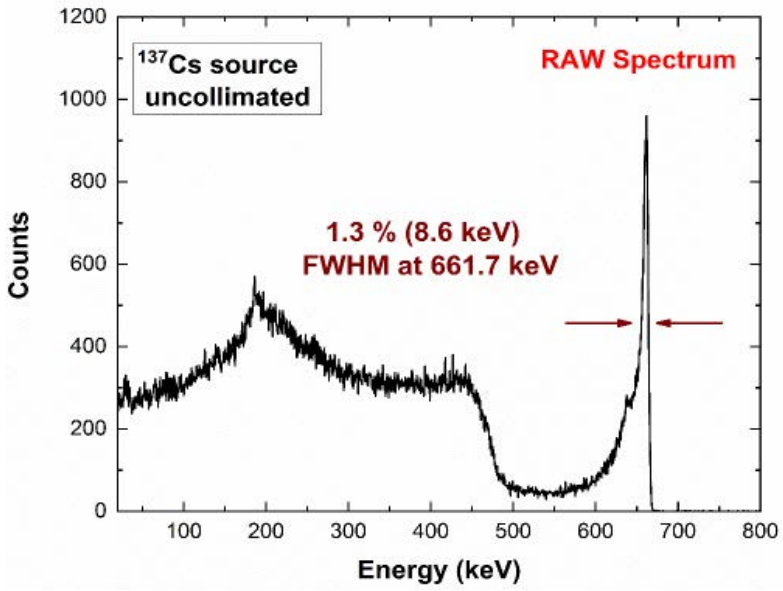

Figure 3.14 *Raw ^{137}Cs spectrum. The energy resolution is 1.3% FWHM at 661.7 keV without correction techniques.*

This is a very good result, which confirms the important technological improvements achieved in the manufacture of the CZT drift strip detectors. According to the current state of the art, the typical energy resolution is of 3 ~ 4% at 662 keV for CZT drift strip detectors (*Budtz-Jørgensen et al., 2017; Howalt Owe et al., 2019; Kalemci et al., al., 2002; Kuvvetli et al., 2010*).

Fig. 3.15 shows uncollimated ^{57}Co spectra measured using the PTF and PPF geometries.

At lower energies (^{241}Am and ^{57}Co sources), the PPF geometry guarantees better performance than the PTF one, thanks to the generation of charge near the cathode due to the lower interaction depth of the photons. In this case, the impulses are less sensitive to the contribution of the gaps. However, at higher energies (^{137}Cs source), with photon interaction present over the entire cathode-anode distance, the two irradiation geometries guarantee similar performance, as reported in Table 3.1. However, the PTF geometry will ensure greater detection efficiency on the 20 mm of CZT (instead of the 6 mm anode-cathode distance).

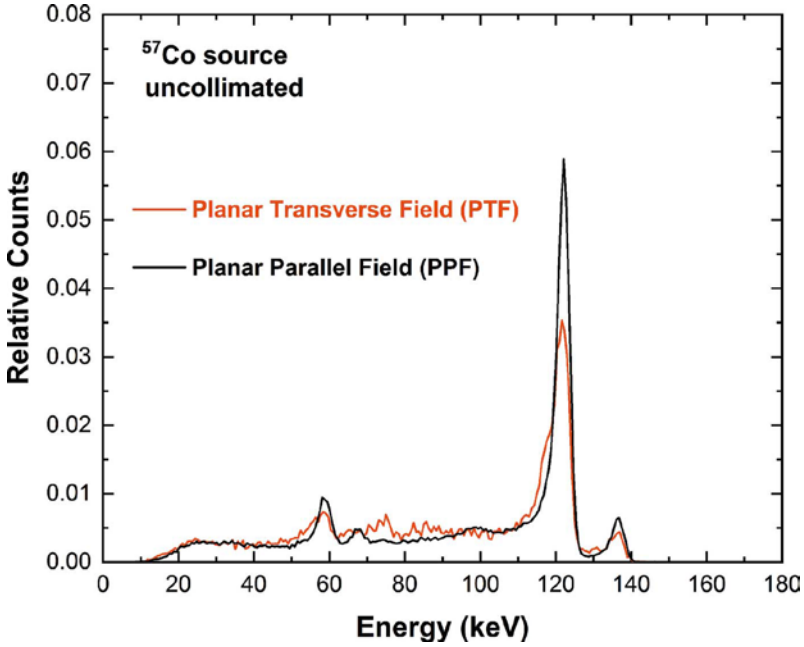

Figure 3.15 *Measured ^{57}Co spectra of a collecting anode strip in PTF and PPF geometries. Energy resolution of 4.9% and 3.3% FWHM at 122.1 keV were obtained in PTF and PPF geometries, respectively.*

Table 3.1 *Energy resolution (FWHM) at different energies of a collecting anode strip of the 3D CZT drift strip detector in PTF and PPF geometries (values refer to raw energy spectra with no spectral correction.).*

The Fano noise was calculated using a Fano factor of F = 0.1 (Devanathan et al., 2006; Kuvvetli & Budtz-Jorgensen, 2005; Owens & Peacock, 2004).

Irradiation Geometry	Energy resolution at 59.5 keV (keV) Fano noise: 0.4 keV	Energy resolution at 122.1 keV (keV) Fano noise: 0.6 keV	Energy resolution at 122.1 keV (keV) Fano noise: 0.6 keV
Planar transverse field	**4.2 (7%)**	**6.0 (4.9%)**	**8.6 (1.3%)**
Planar parallel field	**3.3 (5.6%)**	**4.0 (3.3%)**	**7.9 (1.2%)**

3.5.3 *Spectroscopic improvements with cathode signals*

A critical issue observed in 3D CZT drift strip detectors is represented by the presence of non-uniform spectroscopic response over the cathode–anode depth, with increasing degradations for photon interactions near the anode (*Budtz-Jørgensen & Kuvvetli, 2017; Howalt Owe et al., 2019*).

Regarding the detectors under consideration, evidence of the presence of these distortions was given by the differences observed in detector performance between PTF and PPF geometries, as shown in the previous paragraph. These distortions are better highlighted by the measured spectra (Figure 3.16) from collimated ^{57}Co photon beams (Pb collimator; circular hole diameter Ø = 1 mm) irradiated in PTF geometry at three different positions between the cathode and anode. The photopeak centroid is reduced by about 6% from the cathode to the anode and the energy resolution worsens from 3.2% (near the cathode) to 7.5% (near the anode) FWHM at 122.1 keV.

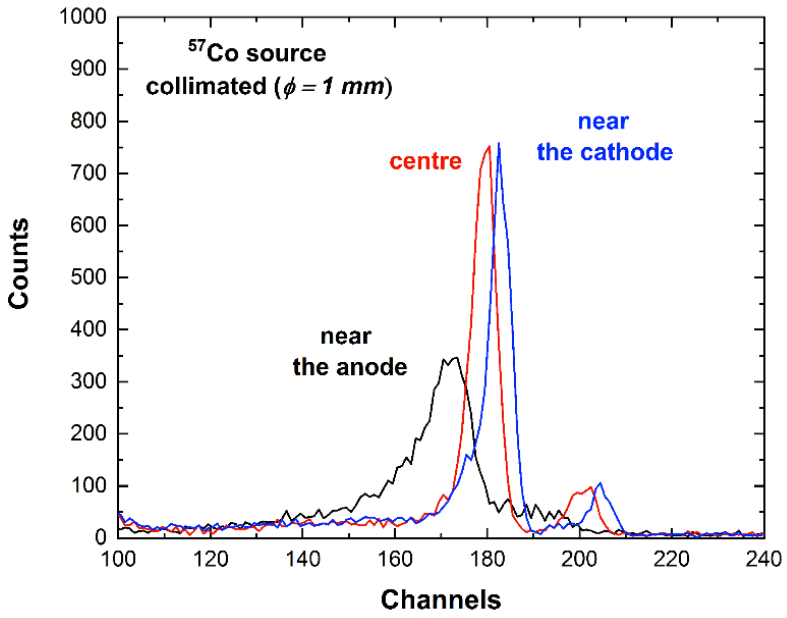

Figure 3.16 *Collimated (Ø = 1 mm) ^{57}Co spectra of a collecting anode strip in PTF geometry at different irradiation positions. The energy spectra show photopeak centroid shifts of about 6% from the cathode to the anode side; the energy resolution is 3.2% and 7.5% FWHM at 122.1 keV near the cathode and anode, respectively.*

This is due to the fact that the weighting potential behaviour of the collecting anode near the anode increases the sensitivity of the pulses to the holes contribution and hence to their trapping effects. In general, mitigation of these non-uniformities can be obtained through the analysis of some features of the cathode and anode pulses. In this case through the cathode to anode (C/A) ratio, the cathode peaking time and the electron drift time were estimated with the goal to exploit their potential in performance recovery.

C/A ratio

As is well known (*Bolotnikov et al., 2016; Kim et al., 2014; Budtz-Jørgensen & Kuvvetli, 2017; Van Pamelen et al., 1998; Verger et al., 2007; Yi et al., 2013*), the C/A ratio is widely used in CZT detectors to compensate for these distortions. However, some critical issues must be taken into account when the C/A ratio is used in CZT drift strip detectors.

First, owing to the low cathode bias voltages (-350 V), the energy spectra from the cathode strips are very poor [Figure 3.17(a)]. This creates significant fluctuations in C/A ratio values and problems in energy calibration of the cathodes. Here, the cathode calibration was successfully performed through low energy spectra (^{241}Am and ^{57}Co sources) measured in PPF geometry, obtaining quite good linearity. Second, charge sharing is present among the cathode strips (as can be clearly seen in the bottom side of figure 3.12) and, therefore, charge sharing addition (CSA) is necessary to correctly estimate the total charge from the cathode strips.

As widely demonstrated in literaure (*Abbene et al., 2018b; Allwork et al., 2012; Brambilla et al., 2012; Bolotnikov et al., 1999; Buttacavoli et al., 2020; Gaskin et al., 2003; Kalemci & Matteson, 2002; Kim et al., 2011*), CSA simply consists of a sum of the energies of the coincidence events among the collecting electrodes (cathode strips in these detectors).

Figure 3.17(b) shows the ^{57}Co spectra from a cathode strip (cathode 3) and from all cathodes after CSA [red line of Figure 3.17(b)].

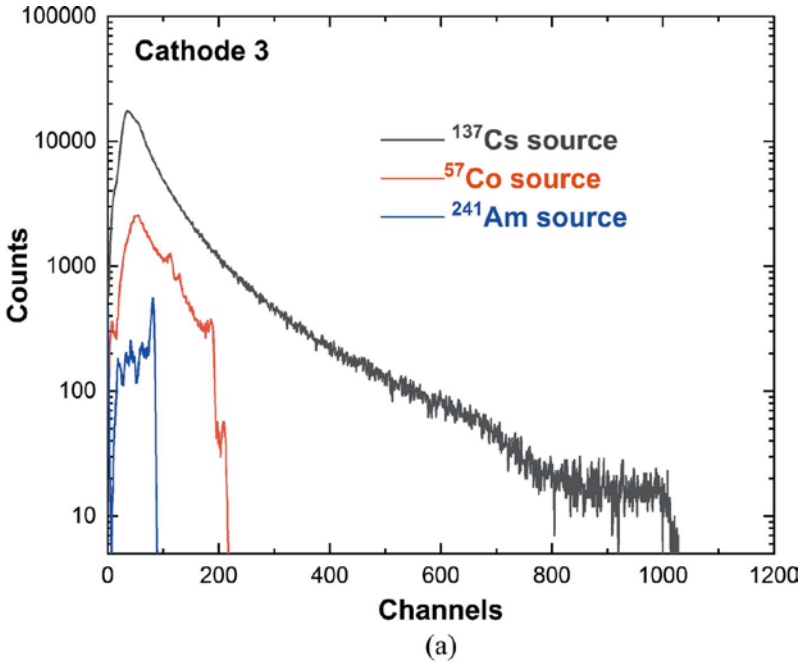

Figure 3.17 *(a) Measured energy spectra from a cathode strip (PTF geometry). (b) ^{57}Co energy spectrum (red line) of all cathode strips after CSA.*

Due to the small inter-strip gap (0.1 mm), if compared with the strip pitch (2 mm), no charge losses are observed after CSA.

Figure 3.18 shows the scatter plots, zoomed in on the 662 keV photopeak region, of the measured C/A ratio, versus the height of the pulses from a collecting anode strip.

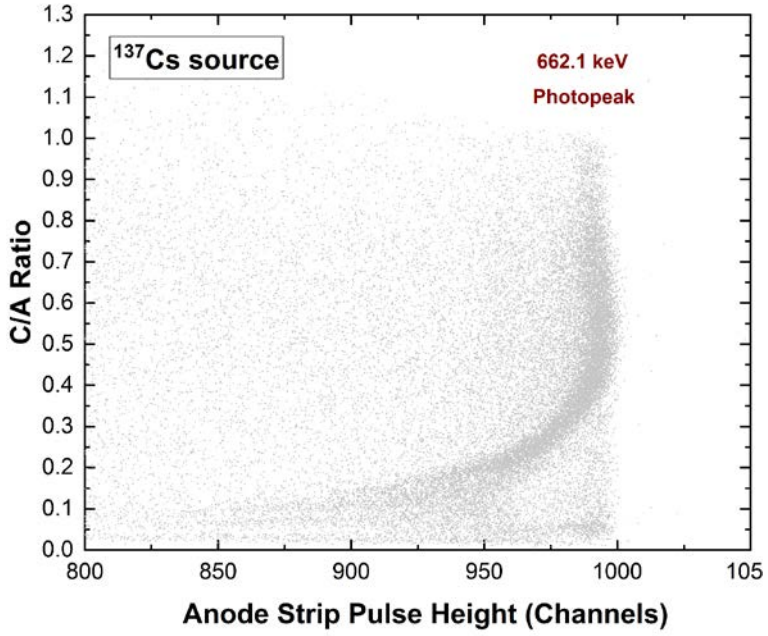

Figure 3.18 *Scatter plots, zoomed in on the 662 keV photopeak region, of the measured C/A ratio, versus the height of the pulses from a collecting anode strip.*

Photopeak shifts, mainly related to interactions near the anode, are visible at low values of these features. The curvature at high C/A values (C/A > 0.7) also confirms the presence of a small contribution from the electron trapping for photon interactions near the cathode.

A performance recovery, by the analisys of scatter plots, was approached.

To obtain a correction for the anode energy E_{corr} was used the following approach:

$$E_{corr} = E_{meas}(F)\frac{E_{best\ photopeak}}{E_{photopeak}(F)} \qquad (3.2)$$

where $\boldsymbol{F}$ is the measured feature, $\boldsymbol{E_{best\ photopeak}}$ is the best photopeak energy (estimated from the energy spectra measured in PPF geometry), $\boldsymbol{E_{meas}(F)}$ is the measured raw energy and $\boldsymbol{E_{photopeak}(F)}$ is the photopeak of the energy spectrum associated with the feature F.

The ^{137}Cs energy spectrum after spectral correction through equation 3.2 is shown in figure 3.19.

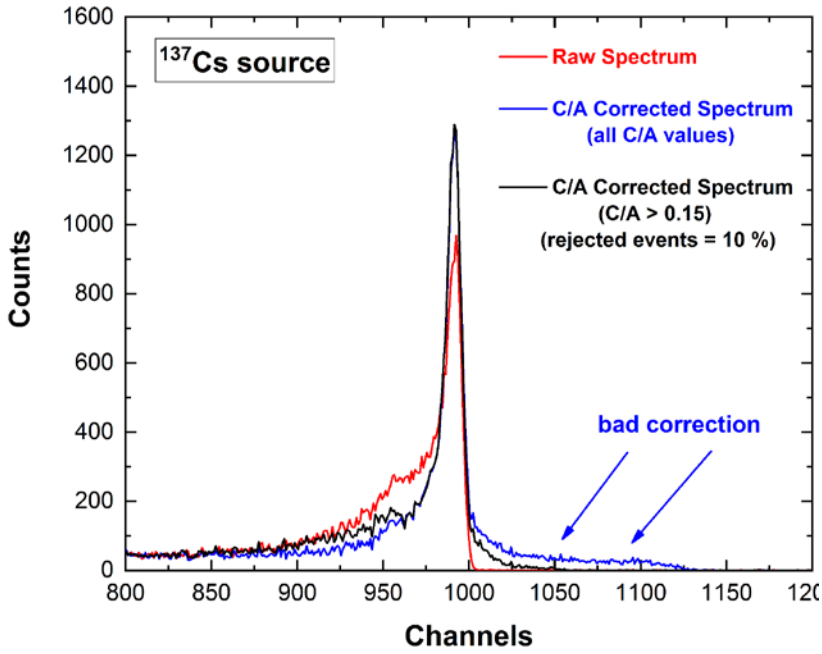

Figure 3.19 *^{137}Cs energy spectra corrected without correction (red line) and after C/A ratio correction (black and blue lines) with equation (3.2). Energy resolutions of 1% FWHM at 661.7 keV was obtained.*

Cathode peaking time

The peaking time of the cathode pulses also follows the depth of interaction between the cathode and anode; due to the similar peaking time values of the shared pulses, it can be helpful to energy addiction when CSA fails, i.e. to better discriminate the collected/shared pulses from induced pulses in cathode strips.
Figure 3.20 shown the distribution of the cathode peaking time versus the height of the pulses from a collecting anode strip.

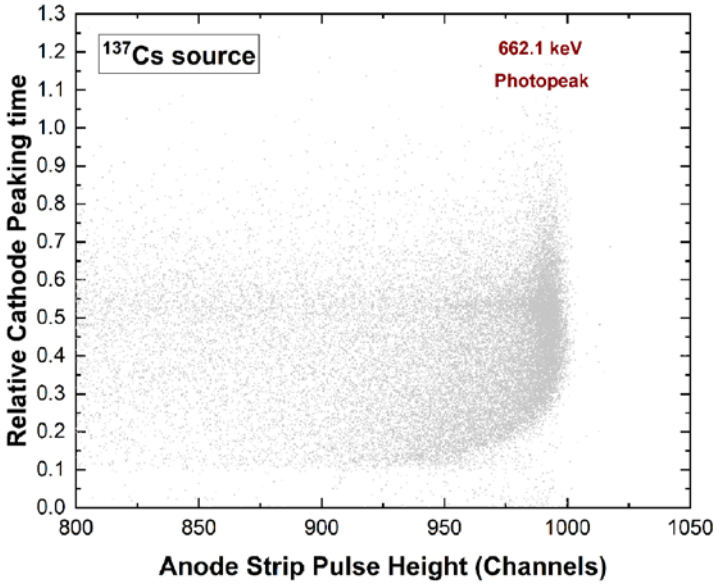

Figure 3.20 *Scatter plots of the relative cathode peaking time versus the height of the pulses from a collecting anode strip.*

Electron drift time

The electron drift time is the time that elapses between the generation of the electron charge cloud and its collection on the anode strip. This is very useful for positioning the double-events of Compton interactions (Compton camera). The measurement of the drift time is influenced by the correct estimation of the arrival times of the pulses which is more critical for anode ones, due to their slow leading edge for interactions that occur near the cathode.

A new method, taking this effect into account, was involved to obtain a good estimate of the electron drift time $\boldsymbol{T_{drift}}$ using following approach:

$$T_{drift} = \begin{cases} T_{anode} - T_{cathode} + T_{anode\ peaking\ time} & (T_{anode} > T_{cathode}) \\ T_{anode\ peaking\ time} & (T_{anode} \leq T_{cathode}) \end{cases} \quad \textbf{(3.3)}$$

where $\boldsymbol{T_{anode}}$ and $\boldsymbol{T_{cathode}}$ are the arrival times of the anode and cathode strip pulses, respectively, and $\boldsymbol{T_{anode\ peaking\ time}}$ is the peaking time of the anode pulses.

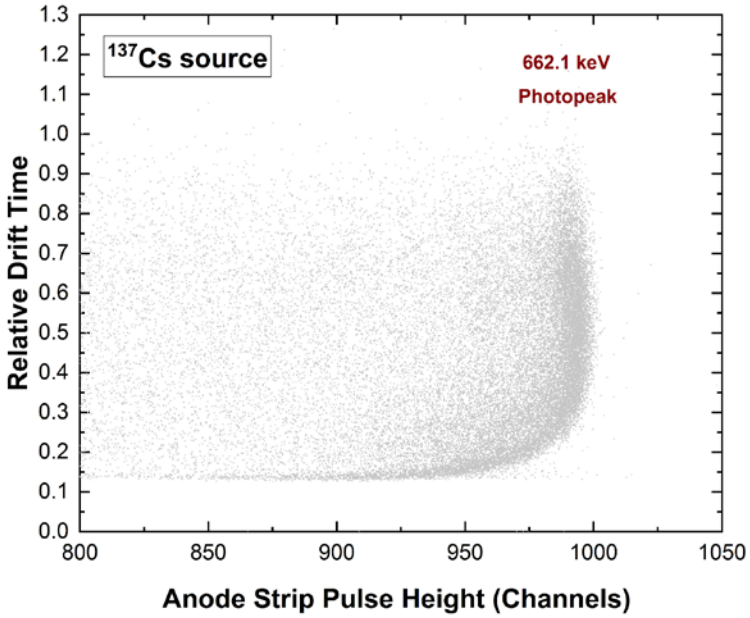

Figure 3.21 *Scatter plots of the relative drift time versus the height of the pulses from a collecting anode strip.*

With the same approach used for C/A ratio (eq. 3.2), was obtained the spectrum in figure 3.22

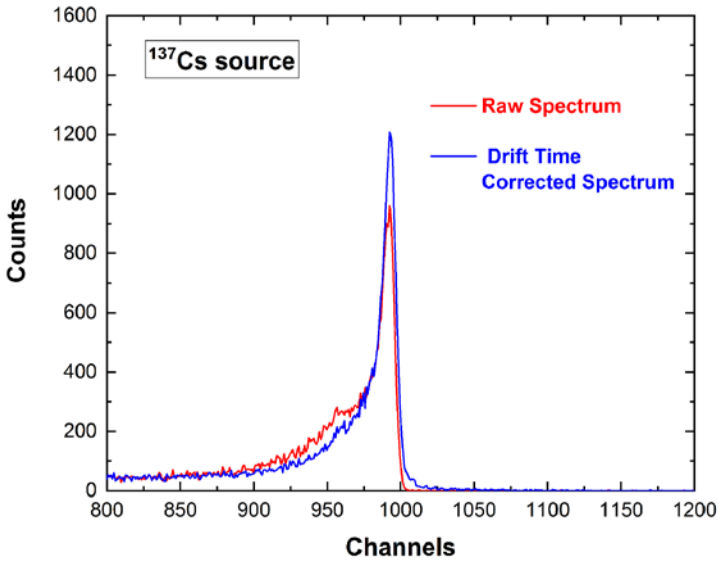

Figure 3.22 *^{137}Cs energy spectra corrected without correction (red line) and after Drift time correction (blue line) with equation (3.1). Energy resolutions of 1.16% FWHM at 661.7 keV was obtained.*

C/A correction gives a slightly better energy resolution (1% FWHM at 661.7 keV) than that of the drift time (1.16% FWHM at 661.7 keV). However, C/A correction requires the rejection of some C/A ratio values which give poor results (blue line of Fig. 3.22), while drift time correction allows the analysis of all events.

3.5.4 Spectroscopic improvements with drift strip signals

Through the pulse analysis (Par. 3.5.1) one sees how some impulses induced on drift strips are characterized by negative saturation levels (Figure 3.23).

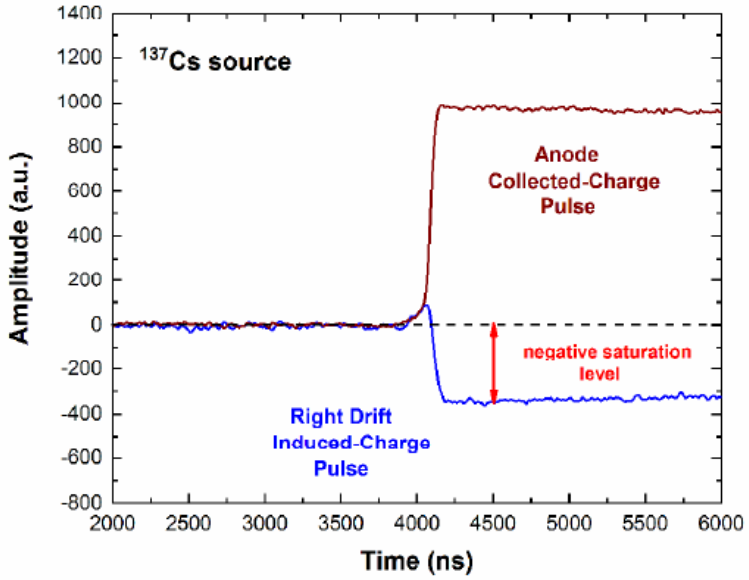

Figure 3.23 *Anode collected charge pulse in temporal coincidence with a drift induced pulse with negative saturation level.*

Through simulations, it was demonstrated that this level of saturation is due to the charge induced by the trapped holes. Hence it was possible to use this feature to reduce the effects of incomplete charge collection. Figure 3.24 (a) shows the scatter plot, zoomed in over the 662 keV photopeak region, of the negative saturation level versus the pulse height from a collecting anode strip. Photopeak lowering is accentuated for higher negative saturation levels.

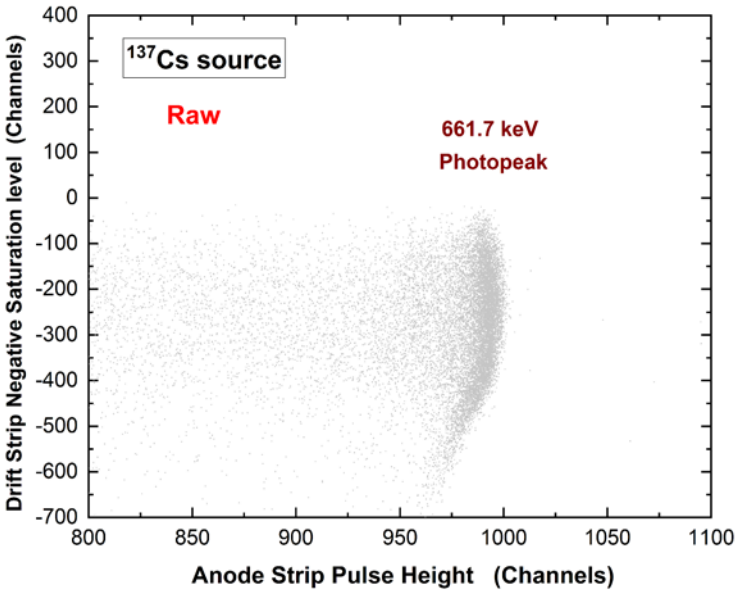

(a)

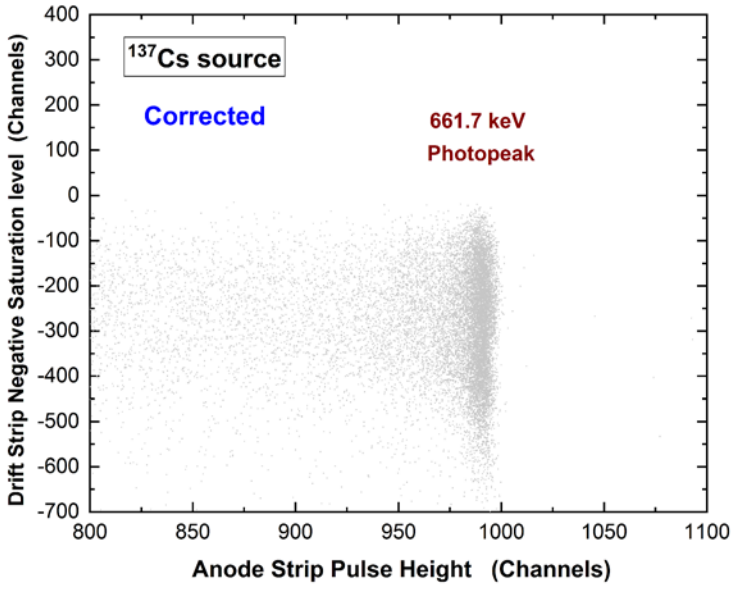

(b)

Figure 3.24 *(a) Raw and (b) corrected [equation 3.1)] scatter plots of the negative saturation level versus the height of pulses from a collecting anode strip.*

Using equation 3.2 with this new feature ***F*** (i.e. the negative saturation level), was obtained a complete recovery of the photopeak (Figure 3.24 (b)) and significant improvements in the energy spectra (0.8%FWHM at 661.7 keV), as shown in Figure 3.25. The energy spectrum ^{137}Cs with the events of the anodic collection strip coinciding in time with all the events from the drift and cathode strip is shown in Figure 3.26. The correction was only applied to the anode strip pulses in temporal coincidence with the induced-charge pulses with negative saturation levels.

An excellent energy resolution of 0.9% FWHM at 661.7 keV characterizes the measured spectrum. To the best of my knowledge, this result represents the best energy resolution value obtained with 3D CZT drift detectors (*Budtz-Jørgensen & Kuvvetli, 2017; Caroli et al., 2010; Howalt Owe et al., 2019; Kuvvetli et al., 2010*).

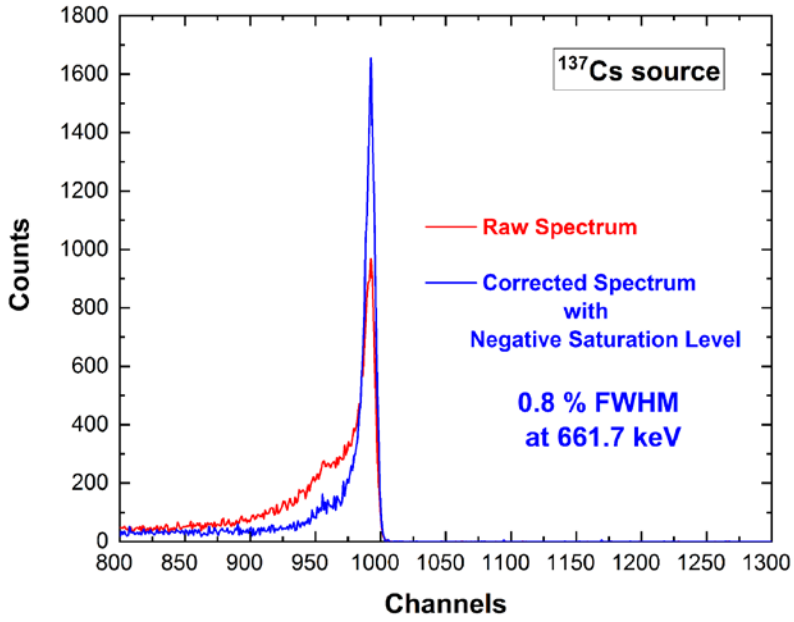

Figure 3.25 *^{137}Cs photopeak reconstruction obtained after correction considering only the induced-charge pulses with negative saturation level. Energy resolutions of 0.8% FWHM at 661.7 keV was obtained.*

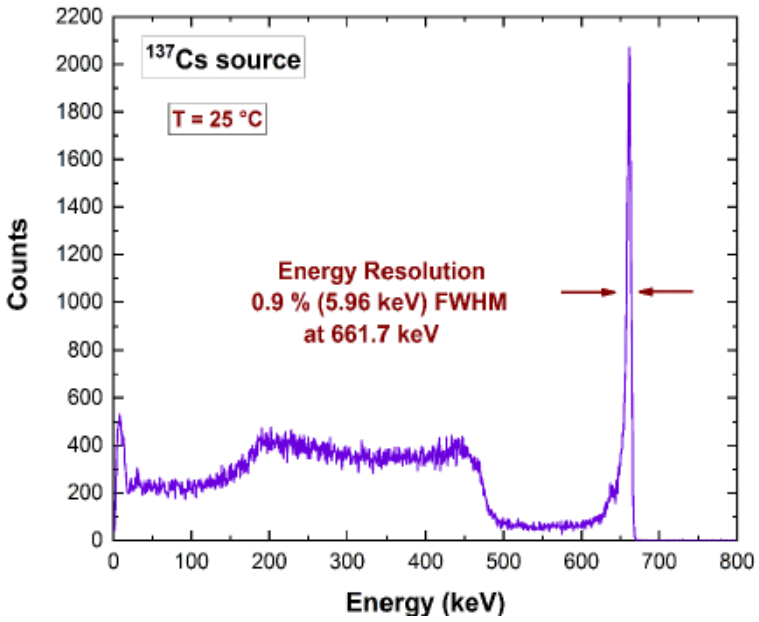

Figure 3.26 *Measured uncollimated ^{137}Cs energy spectrum from a collecting anode strip after spectral correction. The energy spectrum is obtained with the collecting anode strip events in temporal coincidence with all pulses from drift and cathode strips. The correction was only applied to the anode strip pulses in temporal coincidence with the induced-charge pulses with negative saturation levels.*

3.5.5 *Gamma ray and neutron measurements in BNCT environment*

At TRIGA reactor of University of Pavia, measurements with thermal neutrons interacting on a boron sample in water solution were performed.

Figure 3.27 shows the spectra obtained (after application of correction techniques) Moreover, Figure 3.27a shows the difference between the spectrum of a sample of pure water (background) (gray spectrum), and with the boron in water solution (black spectrum). Figure b shows the spectrum of boron solution with more counts.

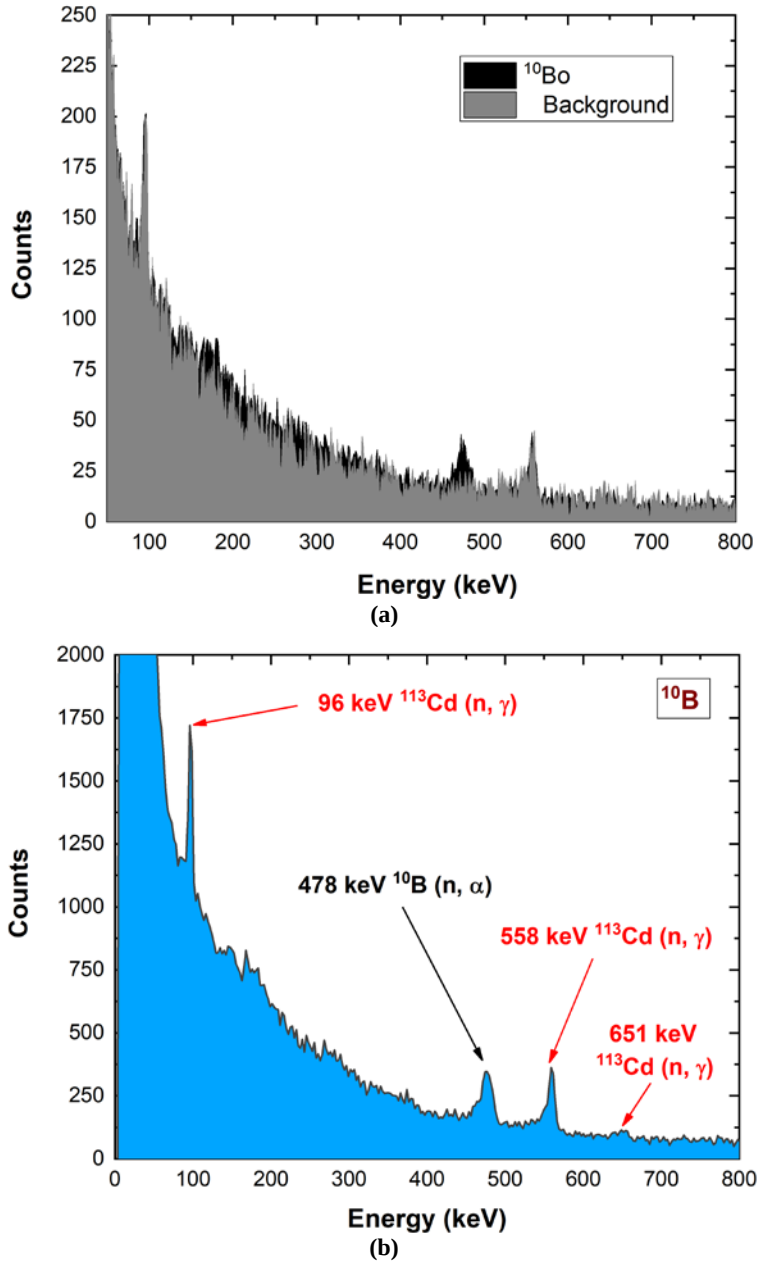

Figure 3.27 (a) *Difference between the background spectrum (gray), and with the boron in water solution (black).* ***(b)*** *Measured spectrum of boron. (Measurements were performed with different acquisition time)*

From spectra in figure 3.27(b) is visible the emission gamma ray at 478 keV due to boron neutron capture (eq 3.1), the broadening of the boron peak is due to the Doppler effect (*Wittig et al., 2008*). In figure 3.27(b) are also marked in red the emission lines due to cadmium neutron capture (*Smither, 1961*).

3.6. Conclusions

The spectroscopic performance of new high-resolution 3D CZT drift strip detectors (19.4 x 19.4 x 6 mm^3) were presented. The detectors are designed to ensure room-temperature measurement of photon energy, timing and 3D positioning up to the megaelectronvolt region, with a moderate number of readout channels (24) for each detector. Due to the focusing effects of the drift strips, charge sharing and mixed induced-collected-charge pulses are not present in collecting anode strips. As reported in the literature, mixed induced-collected-charge pulses have a strong presence in pixelated CZT detectors, representing a critical issue in the correct estimation of the pulse heights. Very good room-temperature energy resolution (1.3% FWHM at 661.7 keV) of the raw energy spectra (with no correction) demonstrates the important advances in device fabrication technology obtained at IMEM/CNR (Parma, Italy) and by due2lab (Reggio Emilia, Italy). Dedicated digital pulse processing, developed at the University of Palermo (Italy), allowed us to exploit the features of the wide range of collected and induced charge pulses from the strips, with excellent results in detector performance enhancements.

In particular, the non-uniformities over the cathode–anode depth, typically present in CZT drift strip detectors, were recovered through the relation of the anode pulses with the C/A ratio, cathode peaking time and drift time (1.0–1.16% FWHM at 661.7 keV).

Excellent spectroscopic improvements (0.8–0.9% FWHMat 661.7 keV) were obtained with a new approach, based on the relation of the anode strip pulses with negative saturation levels of the induced-charge pulses from the drift strips.

Ongoing activities involve the full characterization of the spatial capabilities of the detectors in 3D event reconstruction.

Future work will focus on the capabilities of 3D CZT drift strip detectors as Compton cameras.

CONCLUSIONS

New 2D and 3D CZT detectors were developed and characterized within this PhD research activities. This research was carried out in the framework of a collaboration among the Department of Physics and Chemistry (DiFC) Emilo Segrè of University of Palermo (Italy), the Rutherford Appleton Laboratory (RAL, UK) and an Italian company (due2lab, Parma, Italy), specialized in innovative X-ray inspection systems.

2D CZT detectors based on sub-millimetre arrays (pixel pitches of 500 and 250 μm) were developed as prototypes of advanced X-ray spectroscopic imagers (5-150 keV) for food inspections (Avatar X project). Appealing results were obtained at the cutting edge of the current state-of–art of CZT-based detection systems, summarized as follows:

- excellent room temperature energy resolution of about 1 keV at 60 keV with high bias voltage operation > 6000 V/cm; this is due both to the good electric characteristics of these detectors and the low noise performance of the front-end PIXIE ASIC; the detectors, despite the quasi-ohmic contacts of the electrodes, allow low leakage currents (< $3nA \cdot cm^{-2}$ at 1000V/cm) at room temperature;

- absence of high-flux radiation-induced polarization effects was observed up to fluence rates of 25 x 10^6 photons $mm^{-2} \cdot s^{-1}$; this is due both to the high-bias voltage operation and the physical properties of CZT crystals;

- charge sharing effects were investigated with uncollimated and collimated synchrotron X rays; original techniques able to recover the energy of shared events were developed; different approaches were used for adjacent and diagonal pixels, taking into account the number of involved pixels (i.e. the multiplicity m); one approach, exploiting the relation between the summed energy after CSA and the charge-sharing ratio R of double coincidence events (m =2), allowed the recovery of charge losses between

adjacent pixels; a second technique, based on the linear behaviour of charge losses after CSA with the true photon energy, was also implemented to reconstruct multiple coincidence events with m>2; the energy of double coincidence events between diagonal pixels, mainly due to fluorescence cross talk events, was successfully recovered after the standard CSA; the results showed improved counting efficiency compared to using only isolated events (i.e. after charge sharing discrimination CSD) and improved energy resolution compared to the standard CSA techniques.

The performances of new 3D CZT drift strip detectors were presented; the detectors are designed to ensure room-temperature measurement of photon energy, timing and 3D positioning up to the MeV region, with a moderate number of readout channels (24) for each detector; these detectors were developed, in the framework of the 3-CaTS project, as prototypes of a more complex 3-D imaging system for real-time dosimetric measurements during BNCT (Boron Neutron Capture Therapy) radiotherapy. The following key results are obtained:

- very good room-temperature energy resolution (1.3% FWHM at 661.7 keV) of the raw energy spectra (with no correction) demonstrates the important advances in device fabrication technology obtained within the collaboration;

- due to the use of a custom digital electronics, a dedicated pulse processing analysis was developed and used; this allowed us to exploit the features of the wide range of collected and induced charge pulses from the strips (*zoo of pulses*), with excellent results in detector performance enhancements; in fact, excellent spectroscopic improvements (0.8–0.9% FWHM at 661.7 keV) were obtained with a new approach, based on the relation of the anode strip pulses with the negative saturation levels of the induced-charge pulses from the drift strips;

- the potentialities of the detectors for prompt gamma ray and neutron measurements in BNCT environment were demonstrated at the LENA reactor of University of Pavia with thermal neutrons.

Ongoing activities involve the full characterization of the spatial capabilities of the detectors for 3D event reconstruction.
Future work will focus on the capabilities of 3D CZT drift strip detectors as Compton cameras.

LIST OF PUBLICATIONS

- *Buttacavoli, A.*, Principato, F., Gerardi, G., Mirabello, M., Cascio, D., Raso, G., Bettelli, M., Zappettini, A., Seller, P., Veale, M.C., Abbene, L., "***Energy recovery of multiple charge sharing events in room temperature semiconductor pixel detectors***", *Sensors 21 (11), art. no. 3669,* 2021.
- *Buttacavoli A.*, Principato F., Gerardi G., BettelliM., Amade N.S., Zappettini A., Seller P., Veale M.C., Fox O., Sawhney W., Abbene L., "***Room temperature performance of 3 mm thick cadmium-zinc-telluride pixel detectors with sub-millimetre pixelization***", *J. Synchrotron Rad.*, vol 27, pp. 1180-1189, 2020.
- Abbene L., Principato F., Gerardi G., *Buttacavoli A.*, Altieri S., Gong C., Protti N., Tomarchio E. A., Bettelli M., Sarzi Amadè N., Zanettini S., Zappettini A., Auricchio N., Del Sordo S., Caroli E., "***New results on high-resolution 3-D CZT drift strip detectors***", *2020 IEEE*, (NSS/MIC), pp. 1-3, 2020 proceeding.
- Abbene L., Principato F., Gerardi G., *Buttacavoli A.*, Cascio D., Bettelli M., Amade N.S., Seller P., Veale M.C., Fox O., Sawhney K., Zanettini S., Tomarchio E., Zappettini A., "***Room-Temperature X-ray response of cadmium-zinc-Telluride pixel detectors grown by the vertical Bridgman technique***", ***J. Synchrotron Rad.***, 2020, 27, pp. 319–328.
- Abbene L., Gerardi G., Principato F., *Buttacavoli A.*, Altieri S., Protti N., Tomarchio E., Sordo S.D., Auricchio N., Bettelli M., Amade N.S., Zanettini S., Zappettini A., Caroli E., "***Recent advances in the development of high-resolution 3D cadmium zinc telluride drift strip detectors***", ***J. Synchrotron Rad.***, 2020, 27, pp. 1564–1576.
- Caroli E., Zanettini S., Abbene L., Benassi G., *Buttacavoli A.*, Sarzi Amadè N., Del Sordo S. D., Principato F., Protti N., Sottile G., Stephen J.B., Zambelli N., and Zappettini A., "***Development of a 3D CZT Spectrometer System with Digital Readout for Hard X/Gamma-Ray Astronomy***", 2019 IEEE Nuclear Science Symposium and Medical Imaging Conference, NSS/MIC 2019, 2019, 9059948.
- Fatemi S., Abbene L., Principato F., *Buttacavoli A.*, Auricchio N., Caroli E., Basili A., Zambelli N., Benassi G., Bettelli M., Zanettini S., Zappettini A., Bortolussi S., Magni C., Postuma I., Altieri S., Protti N., "***High performance 3D CZT spectro-imager for BNCT-SPECT: Preliminary characterization***" 2018 IEEE, (NSS/MIC) 2018 proceedings.

BIBLIOGRAPHY

*Abbene L., Del Sordo S., Fauci F., Gerardi G., La Manna A., Raso G., Cola A., Perillo E., Raulo A., Gostilo V. and Stumbo S., "*Spectroscopic response of a CdZnTe multiple electrode detector*", Nucl. Instrum. Methods Phys. Res. A, vol. 583, pp 324–331,* (2007).

*Abbene L. and Gerardi G., "*Performance enhancements of compound semiconductor radiation detectors using digital pulse processing techniques*", Nucl. Instrum. Methods Phys. Res. A, vol. 654, pp. 340–348,* (2011).

*Abbene L., Gerardi G., Turturici A.A., Del Sordo S., Principato F. "*Experimental results from Al/p-CdTe/Pt X-ray detectors*", Nucl. Instrum. Methods Phys. Res. A, vol. 730, pp 135-140,* (2013).

*Abbene L. and Gerardi G., "*High-rate dead-time corrections in a general purpose digital pulse processing system*", J. Synchrotron Rad. vol 22, pp. 1190–1201,* (2015).

*Abbene L., Gerardi G. and Principato F., "*Digital performance improvements of a CdTe pixel detector for high flux energy-resolved X-ray imaging*", Nucl. Instrum. Methods Phys. Res. A, vol. 777, pp. 54–62,* (2015).

*Abbene L., Gerardi G., Turturici A.A., Raso G., Benassi G., Bettelli M., Zambelli N., Zappettini A.and Principato F. "*X-ray response of CdZnTe detectors grown by the vertical Bridgman technique: Energy, temperature and high flux effects*", Nucl. Instrum. Methods Phys. Res. A, vol. 835, pp 1-12* (2016).

*Abbene L., Gerardi G., Raso G., Principato F., Zambelli N., Benassi G., Bettelli M., and Zappettini A., "*Development of new CdZnTe detectors for roomtemperaturehigh-flux radiation measurements*", J. Synchrotron Rad. vol 24, pp. 429–438,* (2017).

*Abbene L., Principato F., Gerardi G., Bettelli M., Seller P., Veale M. C., Zambelli N., Benassi G. and Zappettini A., "*Digital fast pulse shape and height analysis on cadmium–zinc–telluride arrays for high-flux energy-resolved X-ray imaging*", J. Synchrotron Rad. vol. 25, 257-271,* (2018a).

*Abbene L., Gerardi G., Principato F., Bettelli M., Seller P., Veale M. C., Fox O., Sawhney K., Zambelli N., Benassi G. and Zappettini A., "*Dual-polarity pulse processing and analysis for charge-loss correction in cadmium–zinc–telluride pixel detectors.*", J. Synchrotron Rad., vol 25, pp 1078–1092,* (2018b).

*Agostinelli S., et al., "*Geant4-a simulation toolkit*", Nucl. Instrum. Methods Phys. Res. A, vol 506, pp. 250–303* (2003).

*Allwork C., Kitou D., Chaudhuri S., Sellin P. J., Seller P., Veale M. C., Tartoni N. and Veeramani P., "*X-Ray Beam Studies of Charge Sharing in Small Pixel, Spectroscopic, CdZnTe Detectors*", IEEE Trans. Nucl. Sci., vol.* 59*, pp 1563-1568,* (2012).

*Altieri S., Fatemi S., Bortolussi S., Magni C., Postuma I. and Protti N., "*Preliminary Monte Carlo study of CZT response to BNCT (n+γ) background*", Il nuovo cimento, 41 C 208 (2018).*

Alruhaili A., Sellin P. J., Lohstroh A., Veeramani P., Kazemi S., Veale M. C., Sawhney K. J. S. and Kachkanov V., "Performance characteristics of CdTe drift ring detector*", J. Instrum. 9, C03029,* (2014).

Auricchio N., Marchini L., Caroli E., Zappettini A., Abbene L. and Honkimaki V., "Charge transport properties in CdZnTe detectors grown by the vertical Bridgman technique*", J. Appl. Phys. 110, 124502,* (2011).

Awadalla S.A., Al-Grafi M. and Iniewski K., "High voltage optimization in CdZnTe detectors*", Nucl. Instrum. Methods Phys Res. A, vol. 764, pp 193-197,* (2014).

Bale Derek S. and Szeles C. "Nature of polarization in wide-bandgap semiconductor detectors under high-flux irradiation: Application to semi-insulating $Cd_{1-x}Zn_xTe$*" Phys. Rev. B 77, 035205,* (2008).

Barret H. H., Eskin J. D. and Barber H. B., "Charge transport in arrays of semiconductor gamma-ray detectors*", Phys. Rev. Lett. vol. 75, pp. 156–159,* (1995).

Belas E., Uxa S., Grill R., Hlídek P., Šedivý L. and Bugár M., "High temperature optical absorption edge of CdTe single crystal*", J. Appl. Phys. 116, 103521,* (2014).

Benassi G., Nasi L., Bettelli M., Zambelli N., Calestani D. and Zappettini A., "Strong mechanical adhesion of gold electroless contacts on CdZnTe deposited by alcoholic solutions*", J. Instrum. 12, P02018,* (2017).

Bettelli M., Sarzi Amadè N., Calestani D., Garavelli B., Pozzi P., Macera D., Zanotti L., Gonano C. A., Veale M. C., and Zappettini A., "A first principle method to simulate the spectral response of cdznte-based x- and gamma-ray detectors*", Nucl. Instrum. Methods Phys. Res. A, vol. 960, p. 163663,* (2020).

Brambilla A., Ouvrier-Buffet P., Rinkel J., Gonon G., Boudou C. and Verger L., "CdTe Linear Pixel X-Ray Detector With Enhanced Spectrometric Performance for High Flux X-Ray Imaging*", IEEE Trans. Nucl. Sci., vol 59, pp 1552–1558,* (2012).

Bolotnikov A. E., Cook W. R., Harrison F. A., Wong A. S., Schindler S. M. and Eichelberger A. C., "Charge loss between contacts of CdZnTe pixel detectors*", Nucl. Instrum. Methods Phys. Res. A, vol. 432, pp 326–331,* (1999).

Bolotnikov A. E., Camarda G. S., Carini G. A., Cui Y., Li L. and James R. B., "Cumulative effects of Te precipitates in CdZnTe radiation detectors*", Nucl. Instrum. Methods Phys. Res. A, vol. 571, pp 687–698,* (2007).

Bolotnikov A. E., Bale D., Butcher J., Camarda G. S., Cui Y., De Geronimo G., Fried J., Hossain A., Kim K. H., Marshall M., Soldner, S., Petryk, M., Prokesch, M., Vernon, E., Yang, G. and James, R. B. "Comparison of Analog and Digital Readout Electronics on the Processing of Charge-Sharing Events in Pixelated CdZnTe Detectors*", IEEE Trans. Nucl. Sci. 61, 787–792,* (2014).

Bolotnikov A. E., Camarda G. S., Cui Y., De Geronimo G., Eger J., Emerick A., Fried J., Hossain A., Roy U., Salwen C., Soldner S., Vernon E., Yang G. and James R. B., "Use of high-granularity CdZnTe pixelated detectors to correct response non-uniformities caused by defects in crystals*", Nucl. Instrum. Methods Phys. Res. A, vol. 805, pp 41–54,* (2016).

Budtz-Jørgensen C. and Kuvvetli I., "New Position Algorithms for the 3-D CZT Drift Detector", *IEEE Trans. Nucl. Sci. vol. 64, pp. 1611–1618,* (2017).

Buttacavoli A., Principato F., Gerardi G., Bettelli M., Sarzi Amadè N., Zappettini A., Seller P., Veale M. C., Fox O., Sawhney K. and Abbene L., "Room-temperature performance of 3 mm-thick cadmium–zinc–telluride pixel detectors with sub-millimetre pixelization", *J. Synchrotron Rad., vol 27, pp 1180–1189,* (2020).

Butler J. F., Lingren C. L. and Doty F. P, "$Cd_{1-x}Zn_xTe$ gamma ray detectors", *IEEE Trans. Nucl. Sci, vol.39, pp. 605-609,* (1992).

Caroli E., Auricchio N., Del Sordo S., Abbene L., Budtz-Jørgensen C., Casini F., da Silva R. M. C., Kuvvetlli I., Milano L., Natalucci L., Quadrini E. M., Stephen J. B., Ubertini P., Zanichelli M. and Zappettini A., "Development of a 3D CZT detector prototype for Laue Lens telescope", *Proc. SPIE, 7742, 77420V,* (2010).

Chen H., Awadalla S. A., Mackenzie J., Redden R., Bindley G., Bolotnikov A. E., Camarda G. S., Carini G. and James, R. B., "Characterization of Traveling Heater Method (THM) Grown Cd0.9Zn0.1Te Crystals", *IEEE Trans. Nucl. Sci, vol.54, pp. 811-816,* (2007).

Chen H., Awadalla S. A., Iniewski K., Lu P. H., Harris F., Mackenzie J., Hasanen T., Chen W., Redden R., Bindley G., Kuvvetli I., Budtz-Jørgensen C., Luke P., Amman M., Lee J. S., Bolotnikov A. E., Camarda G. S., Cui Y., Hossain A and James, R. B., "Characterization of large cadmium zinc telluride crystals grown by traveling heater method", *J. Appl. Phys. 103, 014903,* (2008).

Cola A. and Farella I. "The polarization mechanism in CdTe Schottky detectors" *Appl. Phys. Lett. 94, 102113,* (2009).

Debertin and R.T. Helmer "Gamma and X-Ray Spectrometry with Semiconductor Detectors", *North Holland Publishers* (1988).

Del Sordo S, Abbene L., Caroli E., Mancini A. M., Zappettini A. and Ubertini P., "Progress in the Development of CdTe and CdZnTe Semiconductor Radiation Detectors for Astrophysical and Medical Applications", *Sensors 9, pp. 3491–3526,* (2009).

Devanathan R., Corrales L.R., Gao F., Weber W.J., "Signal variance in gamma-ray detectors-A review" *Nucl. Instrum. Methods Phys. Res., A, vol 565, pp. 637-649,* (2006).

Du Y., LeBlanc J., Possin G. E., Yanoff B. D. and Bogdanovich S., "Temporal response of CZT detectors under intense irradiation", *IEEE Trans. Nucl. Sci, vol.1, pp. 480-484,* (2002).

Farella I., Montagna G., Mancini A. M. and Cola A., "Study on instability phenomena in CdTe diode-like detectors", *IEEE Trans. on Nucl. Sci., vol. 56, no. 4, pp. 154-161,* (2009).

Fatemi S., Abbene L., Principato F., Buttacavoli A, Auricchio N., Caroli E., Basili A., Zambelli N., Benassi G., Bettelli M., Zanettini S., Zappettini A., Bortolussi S., Magni C., Postuma I., Altieri S., Protti N., "High performance 3D CZT spectro-imager for BNCT-SPECT: Preliminary characterization", *EEE Nucl. Sci. Symp. Conf. Rec. 8824381,* (2018).

Franc J., Dědič V., Rejhon M., Zazvorka J., Praus P., Tous J. and Sellin P.J., "Control of electric field in CdZnTe radiation detectors by above-bandgap light", *J. Appl. Phys. 117, 165702,* (2015).

Gaskin J. A., Sharma D. P. and Ramsey B. D., "Charge sharing and charge loss in a cadmium–zinc–telluride fine-pixel detector array", *Nucl. Instrum. Methods Phys. Res. A, vol 505, pp 122–125,* (2003).

Gatti E. and Rehak P., "Semiconductor drift chamber - An application of a novel charge transport scheme", *Nucl. Instrum. Methods Phys. Res., vol. 225, pp. 608–614,* (1984a).

Gatti E., Rehak P. and Walton, J. T., "Silicon drift chambers - first results and optimum processing of signals", *Nucl. Instrum. Methods Phys. Res. A, vol 226, pp. 129–141,* (1984b).

Gerardi G. and Abbene L., "A digital approach for real time high-rate high-resolution radiation measurements", *Nucl. Instrum. Methods Phys. Res. A, vol 768, pp. 46–54,* (2014).

Grill R., Belas E., Franc J., Bugár M., Uxa S., Moravec P., and Höschl P. "Polarization Study of Defect Structure of CdTe Radiation Detectors", *IEEE Trans. on Nucl. Sci vol. 56, no. 4, pp. 3172-3181,* (2011).

He Z., "Review of the Shockley–Ramo theorem and its application in semiconductor gamma-ray detectors", *Nucl. Instrum. Methods Phys. Res. A, vol. 463, pp 250–267,* (2001).

He Z. and Zhu Y., "Advancement of 4×4×1.5 cm3 CdZnTe Detectors", *Presented At the 2019 Nuclear Science Symposium (NSS) and Medical Imaging Conference (MIC), and the International Symposium on Room Temperature Semiconductor Detectors (RTSD), Held at Manchester, UK, 2019, Oct. 26th – Nov. 2.*

Hecht K., "Zum Mechanismus des lichtelektrischen Primärstromes in isolierenden Kristallen," *Zeitschrift für Phys., vol. 77, no. 3, pp. 235–245,* (1932).

Howalt Owe S., Kuvvetli I., Budtz-Jørgensen C. and Zoglauer A., "Evaluation of a Compton camera concept using the 3D CdZnTe drift strip detectors", *J. Instrum. 14, C01020,* (2019).

Hubert Chen C. M., Boggs S. E., Bolotnikov A. E., Cook W. R., Harrison F. A. and Schindler S. M. "Numerical Modeling of Charge Sharing in CdZnTe Pixel Detectors", *Nucl. Instrum. Methods Phys. Res. A, vol. 482, 395–407,* (2002).

Imahori Y., Ueda Y., Ohmori Y., Kusuki T., Ono K., Fujii R. and Ido T., "Fluorine-18-Labeled FluoroboronophenylalaninePET in Patients with Glioma", *J. Nucl. Med. Vol. 39(2), pp. 325-333* (1998)

Iniewski K., Chen H., Bindley G., Kuvvetli I., and Budtz-Jørgensen C., "Modeling Charge-Sharing Effects in Pixellated CZT Detectors", *IEEE Nuclear Science Symposium Conference Record, pp. 4608-4611,* (2007).

Iniewski K., "CZT detector technology for medical imaging", *J. Instrum. 9, C11001,* (2014).

Jones L.T. and Woollam P.B., "Resolution improvement in CdTe gamma detectors using pulse-shape discrimination*", Nucl. Instrum. Methods Phys. Res., A, vol 124, pp. 591-595,* (1975).

Kalemci, E. & Matteson, J. L. "Investigation of charge sharing among electrode strips for a CdZnTe detector*". Nucl. Instrum. Methods Phys. Res., A, vol 478, pp. 527–537,* (2002).

Kim J. C., Anderson S. E., Kaye W., Zhang F., Zhu Y., Kaye S. J. and He Z., "Charge sharing in common-grid pixelated CdZnTe detectors*" Nucl. Instrum. Methods Phys. Res., A, vol 654, pp. 233-243,* (2011).

Kim J. C, Kaye W. and He Z., "Signal modeling of charge sharing effect in simple pixelated CdZnTe detector*", J. Korean Phys. Soc., vol. 64, pp 1336–1345,* (2014).

Kobayashi T., Sakurai Y. and Ishikawa M., "A noninvasive dose estimation system for clinical BNCT based on PG-SPECT—Conceptual study and fundamental experiments using HPGe and CdTe semiconductor detectors*", Med. Phys., 27(9):2124-32,* (2000).

Koch-Mehrin K.A.L., Bugby S.L., Lees J.E., Veale M.C. and Wilson, M.D., "Charge sharing and charge loss in high-flux capable pixelated CdZnTe detectors*", Sensors Vol. 21, Issue 9, art. no. 3260* (2021).

Knoll, G. F. "Radiation Detection and Measurement*", New York: John Wiley and Sons* (2000).

Kuvvetli I., and Budtz-Jorgensen C., "Pixelated CdZnTe drift detectors*", IEEE Trans. Nucl. Sci., vol.52, pp.1975–1981, (2005).*

Kuvvetli I., and Budtz-Jørgensen C., "Measurements of Charge Sharing Effects in Pixilated CZT/CdTe Detectors*", IEEE Nuclear Science Symposium Conference Record, pp. 2252-2257,* (2007).

Kuvvetli I., Budtz-Jørgensen C., Caroli E. and Auricchio N., "CZT drift strip detectors for high energy astrophysics*", Nucl. Instrum. Methods Phys. Res. A, 624, 486–491,* (2010).

Lingren C. L., Apotovsky B., Butler J. F., Conwell R., Doty F. P., Friesenhahn S. J., Oganesyan A., Pi B. and Zhao S., "Cadmium-zinc-telluride, multiple-electrode detectors achieve good energy resolution with high sensitivity at room-temperature*", IEEE Trans. Nucl. Sci., vol.45, pp. 433–437,* (1998).

Marchini L., Zappettini A., Gombia E., Mosca R., Lanata M. and Pavesi M., "Study of Surface Treatment Effects on the Metal-CdZnTe Interface*", IEEE Trans. Nucl. Sci., vol 56, pp 1823–1826,* (2009).

McCoy J.J, Kakkireni S, Gilvey Z.H., Swain S.K., Bolotnikov A.E. and Lynn K.G., "Overcoming Mobility Lifetime Product Limitations in Vertical Bridgman Production of Cadmium Zinc Telluride Detectors*", Journal of Electronic Materials, vol. 48, Issue 7, pp. 4226-4234,* (2019).

Moss R.L., "Critical review, with an optimistic outlook, on Boron Neutron Capture Therapy (BNCT)*", Appl. Rad. and Isot, vol. 88, pp. 2-11,* (2014).

Ottaviani G., "Charge carriers transport properties in CdTe measured with timeof flight technique*", Revue de Physique Appliquee, vol. 12, no. 2, pp. 249–254,* (1977).

Owens A., den Hartog R., Quarati F., Gostilo V., Kondratjev V., Loupilov A., Kozorezov A. G., Wigmore J. K., Webb A. and Welter E., "Hard x-ray response of a CdZnTe ring-drift detector*", J. Appl. Phys. 102, 054505,* (2007).

Owens A, "Semiconductor Radiation Detectors*" CRC Press, Taylor & Francis Group,* (2019).

Principato F., Turturici A.A., Gallo M., Abbene L., "Polarization phenomena in Al/p-CdTe/Pt X-ray detectors*", Nucl. Instrum. Methods Phys. Res., A, vol 730, pp 141-145,* (2013).

Principato F., Gerardi G., Turturici A.A., Raso G., Quartararo M., Pintacuda F. and Abbene L., "The "livio scarsi" x-ray facility at university of palermo for device testing*", Paper presented at the Proceedings of the European Conference on Radiation and its Effects on Components and Systems, RADECS,* (2015).

Ramo S., "Currents induced by electron motion*", Proceedings of the IRE, vol. 27, pp. 584-585,* (1939).

Rejhon M., Franc J., Dědič V., Kunc J. and Grill R., "Analysis of trapping and de-trapping in CdZnTe detectors by Pockels effect*", J. Phys. D: Appl. Phys. 49, 375101,* (2016).

Schlesinger T.E., James R. B(Eds.), "Semiconductors for Room Temperature Nuclear Detector Applications*", Semiconductors and Semimetals, Vol. 43, Accademic Press, New York,* (1995).

Schlesinger T.E., James R. B(Eds.), "Cadmium zinc telluride and its use as a nuclear radiation detector material*", Materials Science and Engineering: R: Reports, vol. 32, pp. 103-189,* (2001).

Schneider A., Veale M.C., Duarte D.D., Bell S.J., Wilson M.D., Lippa J.D.and Seller P., "Interconnect and bonding techniques for pixelated X-ray and gamma-ray detectors*", J. Instrum 10, C02010, (2015).*

Sellin P. J., Davies A. W., Lohstroh A., Ozsan M. E. and Parkin, J., "Drift mobility and mobility-lifetime products in CdTe: Cl grown by the travelling heater method*", IEEE Trans. Nucl. Sci. 52, 3074–3078,* (2005).

Sellin P. J., Prekas G., Franc J., and Grill R., "Electric field distributions in CdZnTe due to reduced temperature and x-ray irradiation*", Appl. Phys. Lett. 96 133509,* (2010).

Shockley W., "Currents to conductors induced by a moving point charge*", Journal of applied physics, vol. 9, pp. 635-636,* (1938).

Sjőland K. A. and Kristiansson P., "Pile-up and defective pulse rejection by pulse shape discrimination in surface barrier detectors*", Nucl. Instrum. Methods Phys. Res. B, vol 94, pp. 333-337,* (1994).

Smither R.K., "Capture-Gamma-Ray Spectrum of $Cd^{113}(n, \gamma)$ Cd^{114} and the associated Energy Levels in Cd^{114}*", Phys. Review, vol 124, n 1, pp 183-192* (1961).

Squillante M. R., Christian J. F., and Entine G., "Solid State Radiation Detectors", *American Cancer Society, pp. 1–18,* (2016).

Thomas B., Veale M. C., Wilson M. D., Seller P., Schneider A. and Iniewski, K., "Characterisation of Redlen high-flux CdZnTe", *J. Instrum. 12, C12045,* (2017).

Toyama H., Higa A., Yamazato M., Maehama T., Ohno R. and Toguchi M., "Quantitative analysis of polarization phenomena in CdTe radiation detectors", *Japanese journal of applied physics, vol. 45, p. 8842,* (2006).

Uxa Š., Belas, E. Grill R., Praus P.and James R.B., "Determination of electric-field profile in CdTe and CdZnTe detectors using transient-current technique", *IEEE Trans. Nucl. Sci. 59, 2402–2408, (2012).*

Van Pamelen M. A. J. and Budtz-Jørgensen C., "Novel electrode geometry to improve performance of CdZnTe detectors", *Nucl. Instrum. Methods Phys. Res. A, vol 403, pp. 390–398,* (1998).

Vartsky D., Goldberg M., Eisen Y., Shamai Y., Dukhan R., Siffert P., Koebel J. M., Regal R. and Gerber J., "Radiation induced polarization in CdTe detectors", *Nucl. Instrum. Methods Phys. Res. A, vol 263, pp. 457-462,* (1988).

Veale M. C., Bell S. J., Duarte D. D., Schneider A., Seller P., Wilson M. D., and Iniewski K., "Measurements of charge sharing in small pixel CdTe detectors", *Nucl. Instrum. Methods Phys. Res. A, vol 767, 218–226,* (2014).

Veale MC, Booker P, Cross S, Hart MD, Jowitt L, Lipp J, Schneider A, Seller P, Wheater RM, Wilson MD, Hansson CCT, Iniewski K, Marthandam P and Prekas G. "Characterization of the Uniformity of High-Flux CdZnTe Material". *Sensors (Basel).;20(10):2747,* (2020).

Verger L., Gros d'Aillon E., Monnet O., Montémont G. and Pelliciari B., "New trends in γ-ray imaging with CdZnTe/CdTe at CEA-Leti", *Nucl. Instrum. Methods Phys. Res. A, vol. 571, pp 33–43,* (2007).

Williams D. J., "Densities and lattice parameters of CdTe, CdZnTe and CdTeSe", *Properties of Narrow Gap Cadmium-based Compounds, edited by Peter Capper,* (1994).

Wittig A., Michel J., Moss R.L., Stecher-Rasmussen F., Arlinghaus H.F., Bendel P., Mauri P.L., Altieri S., Hilger R., Salvadori P.A., Menichetti L., Zamenhof R. and Sauerwein W.A.G., "Boron analysis and boron imaging in biological materials for Boron Neutron Capture Therapy (BNCT)", *Critical Reviews in Oncology/Hematology Vol 68, Issue 1, pp 66-90* (2008).

Yin Y., Chen X., Wu H., Komarov S., Garson A., Li Q., Guo Q., Krawczynski H., Meng L. J. and Tai Y. C., "3-D Spatial Resolution of 350 /spl mu/m Pitch Pixelated CdZnTe Detectors for Imaging Applications", *IEEE Trans. Nucl. Sci., vol. 60, pp 9–15.*

Zanettini S., Pattini F., Sarzi Amadè N., Sidoli M., Zambelli N., Benassi G., Bettelli M., Rampino S., Gilioli E., Protti N., Fatemi S., and Andrea Zappettini "Al_2O_3 Coating as Passivation Layer for CZT-basedDetectors", *2018 IEEE Nuclear Science Symposium and Medical Imaging Conference Proceedings (NSS/MIC), 2018, pp. 1-5,* (2018).

Zanichelli M., Pavesi M., Marchini L. and Andrea Zappettini, "Studies on charge collection and transport properties on semi-insulating materials in the presence of a non-uniform electric field*", Solid State Communications, vol. 152, Issue 14, Pages 1212-1215,* (2012).

Zappettini A., Zha M., Pavesi M. and Zanotti L., "Boron oxide fully encapsulated CdZnTe crystals grown by the vertical Bridgman technique*", J. Cryst. Growth, 307, 283–288,* (2007).

Zappettini A., Zha M., Marchini L., Calestani D., Mosca R., Gombia E., Zanotti L., Zanichelli M., Pavesi M., Auricchio N. and Caroli E., "Boron Oxide Encapsulated Vertical Bridgman Grown CdZnTe Crystals as X-Ray Detector Material*", IEEE Trans. Nucl. Sci. 56, 1743–1746,* (2009).

Zhang F., Herman C., He Z., De Geronimo G., Vernon E. and Fried J., "Characterization of the H3D ASIC Readout System and 6.0 cm^3 3-D Position Sensitive CdZnTe Detectors*". IEEE Trans. Nucl. Sci., vol.59, pp. 236–242,* (2012).

Zhu Y., Anderson S. E. and He Z., "Sub-Pixel Position Sensing for Pixelated, 3-D Position Sensitive, Wide Band-Gap, Semiconductor, Gamma-Ray Detectors*", IEEE Trans. Nucl. Sci. vol. 58, pp 1400–1409,* (2011).